Master's thesis

NTNU
Norwegian University of Science and Technology
Faculty of Engineering
Department of Marine Technology

Mildrid Sofie Breivik Haga

Hydrodynamic Challenges of Floating Wind Turbines in Shallower Water Depth

Master's thesis in Marine Technology
Supervisor: Marilena Greco
June 2019

NTNU
Norwegian University of
Science and Technology

Mildrid Sofie Breivik Haga

Hydrodynamic Challenges of Floating Wind Turbines in Shallower Water Depth

Master's thesis in Marine Technology
Supervisor: Marilena Greco
June 2019

Norwegian University of Science and Technology
Faculty of Engineering
Department of Marine Technology

NTNU
Norwegian University of
Science and Technology

NTNU Trondheim
Norwegian University of Science and Technology
Faculty of Engineering Science and Technology
Department of MarineTechnology

MASTER THESIS IN MARINE TECHNOLOGY

Spring 2019

FOR

Mildrid Sofie Breivik Haga

Hydrodynamic challenges of floating wind turbines in shallower depths

(Hydrodynamiske utfordringer av flytende vindturbiner i grunnere dybder)

Offshore wind energy is an attractive renewable resource due to high and consistent wind speeds. At present, the majority of installed turbines are on bottom-fixed support structures. There is some evidence that floating platforms may be economically feasible at water depths (~50-70 m), because of less infrastructure demand than bottom-fixed concepts, keeping the larger flexibility in placing the platform, and proximity to land-based demand centers. However, there are still technical challenges. For example, the dynamic mooring line loads as a combination of wind, wave, and current excitation may present more significant design challenges as the water depth decreases.
A preliminary project work has been performed to document the state of the art. The Buchan Deep, where Equinor's Hywind wind park is located, was selected as site with intermediate/shallow water depth for the numerical investigations of the (publicly available) Olav Olsen semi-submersible supporting the DTU 10MW turbine. The SIMA simulation platform was chosen as research tool, and applied to the floating wind turbine (FWT) for preliminary verification studies.

Objective

The present master thesis aims to investigate possible use of a floating wind turbine (FWT) concept at shallower water depths. This emphasis is on the critical mooring-line loads in combined wave-current-wind conditions, with the attempt to provide insights on the physical mechanisms relevant for the platform behaviour, as well as on the applicability of simplified load models.

The work should be carried out in steps as follows:

1. Summarize major findings/outcomes from the project thesis and, if necessary, complement the literature survey in order to identify state-of-the-art of the problem.
2. Describe the assumptions and features of the simulation platform selected as research tool. Complement with the modelling of second-order slow-drift load effects, neglected in the project-thesis studies, and with alternative more realistic mooring-line load modelling to be compared in the analysis against a simplified linear spring model.
3. Investigate the possible reasons for differences between the project-thesis results and the used reference solutions and finalize the verification study.
4. Perform a systematic parameter study of the mooring-line loads and FWT behaviour in relevant (operational and extreme) environmental conditions. In the analysis, the hydrodynamic loads on the FWT should be modelled alternatively as (a) linear 3D potential-flow loads, (b) linear excitation and added-mass loads from Morison's equation, (c) linear plus second-order (slow-drift) 3D potential-flow loads. The slow-drift loads should be calculated both using the Newman's approximation and with

complete second-order transfer function. The effect of viscous damping should be examined using the drag term in Morison's equation.

5. Draw the conclusions from the studies and discuss possible further research steps.

The work may show to be more extensive than anticipated. Some topics may therefore be left out after discussion with the supervisor without any negative influence on the grading.

The candidate should in her report give a personal contribution to the solution of the problem formulated in this text. All assumptions and conclusions must be supported by mathematical models and/or references to physical effects in a logical manner.

The candidate should apply all available sources to find relevant literature and information on the actual problem.

The thesis should be organised in a rational manner to give a clear presentation of the work in terms of exposition of results, assessments, and conclusions. It is important that the text is well written and that tables and figures are used to support the verbal presentation. The thesis should be complete, but still as short as possible. In particular, the text should be brief and to the point, with a clear language. Telegraphic language should be avoided.

The thesis must contain the following elements: the text defining the scope (i.e. this text), preface (outlining project-work steps and acknowledgements), abstract (providing the summary), table of contents, main body of thesis, conclusions with recommendations for further work, list of symbols and acronyms, references and (optional) appendices. All figures, tables and equations shall be numerated.

The supervisor may require that the candidate, in an early stage of the work, present a written plan for the completion of the work. The plan should include budget for the use of computer and laboratory resources that will be charged to the department. Overruns shall be reported to the supervisor.

From the thesis it should be possible to identify the work carried out by the candidate and what has been found in the available literature. It is important to give references to the original source for theories and experimental results.

Supervisor : Marilena Greco
Co-supervisor : Erin Bachynski
Co-supervisor : Claudio Lugni

Submitted : January 15th 2019
Deadline : June 11th 2019

Marilena Greco
Supervisor

Preface

This report is a result of the Master thesis written the spring of 2019 as a part of the Master of Science (MSc) degree of Marine Technology at Norwegian University of Science and Technology (NTNU) under the department of hydrodynamics.

The topic of the Master thesis was chosen due to the author's interest in renewable energy and hydrodynamics. Also, the opportunity to become familiar with different simulation tools used in the marine industry was a motivation behind the selection.

Preliminary work was carried out in the fall of 2018 and resulted in a project thesis. The project thesis considered a broad aspect of floating wind turbines and included general information about the state-of-the-art of floating wind turbine concepts, the current market situation and different research activities. This thesis, on the other hand, is narrowed in and do only consider literature and theory related to the objective. Some sections were taken directly from the project thesis, but this is emphasised at the relevant places.

Trondheim, June 7th, 2019

Mildird Haga

Acknowledgements

I would like to thank my supervisor, Marilena Greco, for the weekly follow-up meetings that have helped me work continuously throughout the year. I would also like to thank her for the good advises she has provided and for helping me understand complicated hydrodynamic theory.

Secondly, I would like to thank my co-supervisor Erin Bachynski for helping me with all the issues I had regarding the software used in the project and for always answering quickly. Also, her expertise within floating wind turbines and the understanding she has provided me regarding this topic has been of great value.

Thirdly, I would like to thank Carlos Eduardo Silva de Souza for the help he has provided and the hours he has spent trying to fix my SIMA model. His help has been priceless in the modeling and analysis process.

Finally, I would like to thank my fellow students at office C1.058 for the support and help throughout the semester.

Abstract

Today, all floating wind turbines are installed at deep water (>100 m). However, due to proximity to land-based demand centers and available areas, installations at water depths from 50-70 m become profitable. At these water depths, several technical challenges arise concerning critical mooring line loads and the applicability of hydrodynamic load models. The objective of this thesis is to study the OO Star 10 MW Wind Floater, a floating wind turbine with a semi-submersible platform, at 50 m water depth. The behavior of the structure in operational and extreme conditions has been analyzed, as well as the applicability of different hydrodynamic load models.

A numerical model of the floating wind turbine was developed. A panel model was created with the software GeniE and HydroD, and first and second order frequency domain analyses were carried out to obtain the hydrodynamic properties of the body. To account for second-order effects, a panel model of the free surface was included in this model. The hydrodynamic properties were imported into the software SIMA, where a coupled model was created.

Performing a frequency domain analysis is computationally expensive. Therefore, a simplified method applying strip theory to calculate the added mass was considered and compared to the model from the frequency domain analysis. This was done by calculating the two-dimensional added mass for a cross-section based on potential theory and adding the terms to slender elements defined in the coupled model in SIMA.

The Buchan Deep was chosen as the site for installing the floating wind turbine. Environmental conditions from this site were obtained and used to create load cases for time-domain simulations. Six load cases, representing operational and extreme conditions, were established.

The numerical models were verified by carrying out decay tests and regular wave tests. A constant wind test was conducted to ensure that the performance of the wind turbine was correct. Then, each numerical model was subjected to time-domain simulations performed with SIMA. A statistical analysis of the responses, loads, and mooring line tensions was carried out, and power spectral density(PSD)-diagrams were created. The results obtained from the time-domain analyses were compared and discussed.

The results showed the importance of considering second-order effects to capture large resonant low-frequency motions. Newman's approximations showed good agreement with analyses carried out with a full quadratic transfer function(QTF) in surge, and was concluded to be applicable to this motion. The model applying strip theory underestimated responses at high frequencies and overestimated responses at low frequencies. This model was therefore not considered to provide satisfactory results for the calculation of the responses.

Sammendrag

Idag er alle flytende vindturbiner installert på dypt vann(> 100 m). Nærhet til kyst og tilgjengelige områder, gjør derimot også installasjon på vanndybder fra 50-70 m lønsomt. Men, ved denne vanndybden oppstår det tekniske problemer knyttet til design av forankringslinene og andvendbarheten til hydrodynamiske lastberegningsmodeller. Målet med denne masteroppgaven var å studere vindturbin modellen OO Star 10 MW Wind Floater med halvt-nedsenkbar platform på 50 meters vanndybde. Bevegelsene til den flytende vindturbinen ble studert for operasjonelle og ekstreme værtilstander, samt anvendbarheten til ulike last modeller.

En numerisk modell av den flytende vindturbinen ble utviklet. En panel modell ble laget med programvarene GeniE og HydroD, og en første og andre ordens frekvensdomene-analyse ble utført for å anskaffe de hydrodynamiske egenskapene til strukturen. For at andre ordenseffekter skulle bli tatt med i beregningene, ble også en panel modell av den frie overflaten modellert. De hydrodynamiske egenskapene ble så importert til programvaren SIMA hvor en koplet model ble utviklet.

Å utføre en frekevensdomene-analyse krever høy datakapasitet. Derfor ble en forenklet metode bestående av å bruke stripeteori til å beregne tilleggsmasse benyttet og sammenlignet med de numeriske modellene utviklet med frekvensdomene-analyse. Dette ble gjort ved å regne ut to-dimensjonal tilleggsmasse basert på potensialteori og å legge disse verdiene til slanke legemer definert i den koplede modellen i SIMA.

Buchan dypet ble valgt til lokasjon for den flytende vindturbinen. Værdata fra dette området ble anskaffet og brukt til å lage last-tilfeller for tids-domene simuleringer. Seks ulike last-tilefeller som representerer operasjonelt og ekstremt vær ble laget.

Egenskapene til de numeriske modellene ble bekreftet ved å utføre fri-osilleringstester og regulær bølge tester. En konstant vind test ble utført for å forsikre at vindturbinen var riktig modellert. Deretter ble hver numerisk modell utsatt for en tidsdomene-analyse utført i SIMA. En statistisk analyse av responsen, lastene og spenning i forankringslinene ble gjort og PSDer ble fremstilt. Resultatene for tidsdomene-analysene ble sammenlignet og diskutert.

Resultatene viste at det er veldig viktig å ta hensyn til andreordens effekter for å få med store, resonante lav-frekvente bevegelser i beregningene. Newmans tilnærming viste enighet med analysene utført med fulle kvadratiske transferfunksjoner i jag og det ble konkludert med at denne tilnærmingen er anvendbar når jag-bevegelsen vurderes. Modellen som anvendte stripeteori underestimerte bevegelsene ved høye frekvenser og overestimerte bevegelsene ved lave frekvenser. Denne modellen ble derfor ikke vudert til å gi tilstrekkelige resultat ved beregning av responser.

Contents

List of Figures

List of Tables

Nomenclature

Acronyms

BEM Blade Element/Momentum

DOF Degree of Freedom

ETM Extreme Turbulence Model

JONSWAP Joint North Sea Wave Project

LFDA Linear Frequency Domain Analysis

NTM Normal Turbulence Model

PSD Power Spectral Density

QTF Quadratic Transfer Function

RAO Response Amplitude Operator

WM Wind Model

Greek Letters

α	Shape Parameter
β	Scale Parameter
ϵ	Phase Angle
η	Body Response
γ	Peakness Parameter
λ	Wave Length
ω	Wave Frequency
ω_0	Natural Frequency

ω_p Peak Frequency

ϕ Velocity Potential

ρ Density

σ^2 Variance

ζ Wave Elevation

ζ_a Wave Amplitude

Latin Letters

a Horizontal Wave Particle Acceleration

A_{kj} Added Mass

B_{kj} Damping Coefficient

C_a Added Mass Coefficient

C_D Drag Coefficient

C_M Mass Coefficient

C_{jk} Restoring Coefficient

D Diameter

F Excitation Load

g Gravitational Acceleration

h Water Depth

H_S Significant Wave Height

k Wave Number

L Length

l_s Length of Suspended Mooring Line

m_h Added Mass Matrix of Slender Element

m_k Spectral Moment

M_{kj} Mass

p Pressure

q Excitation Load

R	Radius
$S(\omega)$	Wave Specter
T	Wave Period
T_H	Horizontal Tension
T_P	Peak Period
T_{jk}	Second Order Transfer Function
U	Velocity
u	Horizontal Wave Particle Velocity
U_C	Current Velocity
U_W	Wind Velocity
V_S	Volume of Strip
w	Mooring Line Weight

Chapter 1

Introduction

Offshore wind is considered the most developed offshore renewable technology, and over the last years, the number of installations has increased significantly. Today, almost all installed offshore wind turbines are fixed to the bottom and installed at water depths shallower than 50 m. At water depths deeper than 50 m, bottom fixed structures are no longer considered economically feasible. However, there are several advantages considering installing wind turbines at deeper water such as steadier and higher wind speed, large available areas, and lower visibility and noise impact [9].

For deeper water depths, floating wind turbines have been developed. These are still in an early phase of development, and a cost reduction is required to make production and operation profitable. The floating wind turbines operating today are installed at deep water(>100 m), but the proximity to land-based demand centers and available areas make installations at shallower water depths from 50-70 m beneficial. However, technical challenges arise in these water depths concerning the mooring line loads and the applicability of hydrodynamic load models.

The OO Star 10 MW Wind Floater is a floating wind turbine substructure concept designed by Dr.Tech Olav Olsen [10]. This substructure was designed as a part of the Lifes50+ project initiated by the European Union which goal is to develop a cost-efficient substructure for a 10 MW wind turbine.

The main objective of this thesis is to study the behavior of the OO Star 10 MW Wind Floater at 50 m water depth, and to evaluate the applicability of different hydrodynamic load models for the floating wind turbine model at this water depth.

1.1 Background

1.1.1 Summary of Preliminary Studies

During the fall of 2018, a project thesis was produced as a preliminary work for the current project. In this thesis, the main focus was to develop a numerical model of the OO Star 10 MW Wind Floater and to verify the model by comparing the performance of the model to the performance of the numerical model defined by Lifes50+ [11].

The numerical model was created using different simulation tools. A panel model was created with the DNV GL software Sesam GeniE. This panel model was made of shell elements and had the shape and dimensions of the semi-submersibles. The model was discretized into panel and the size of the panels was decided by performing a convergence test based on the values of the frequency dependent added mass and damping. A frequency domain analysis was performed with the DNV GL software HydroD to obtain the frequency dependent added mass and damping of the structure. These properties were then written out and imported into the simulation tool, SIMA, used to carry out time-domain simulations.

A few simplifications were made to the numerical model. The mooring system was modeled as a linear spring. This was done by applying horizontal stiffness directly into the hydrostatic stiffness matrix in SIMA. This stiffness was calculated based on the natural period in surge of the model taken from the Lifes50+ model [11]. Table 1.1 shows the natural periods obtained from a decay test of the numerical model compared with results from Lifes50+.

Response	T_n Lifes50+ $[s]$	T_n Num. Model$[s]$	Difference
Surge	181.8	200.4	9.3 %
Heave	20.4	19.6	3.9 %
Pitch	31.25	29.33	6 %
Yaw	116.3	116.28	0.0 %

Table 1.1: Comparison between natural periods from the model defined in Lifes50+ with the numerical model [1]

Another simplification made was to neglect the second-order effects. From the literature review, it was found that these effects are essential for moored structures. It was therefore suggested to include these in the Master thesis.

A constant wind test was carried out to verify the performance of the wind turbine. However, the results were not satisfactory at wind speeds above rated wind speed, and it was proposed to fix this in the work of the Master thesis.

Time-domain analyses were carried out for three different wind speeds. One below rated, one at rated and one above rated wind speed. The corresponding wave height and peak period were obtained from the joint distribution of wind speed, significant wave height, and peak period.

The load case considering the rated wind speed gave the largest offset in surge and pitch. Figure 1.1 shows the time-series of the load case in these degrees of freedom. Table 1.2 lists the statistical values of the platform motions for this load case. The offset in surge was considered drastically large. The spring model will therefore be compared to a model including a mooring system installed at 50 m water depth, which is developed in the current project.

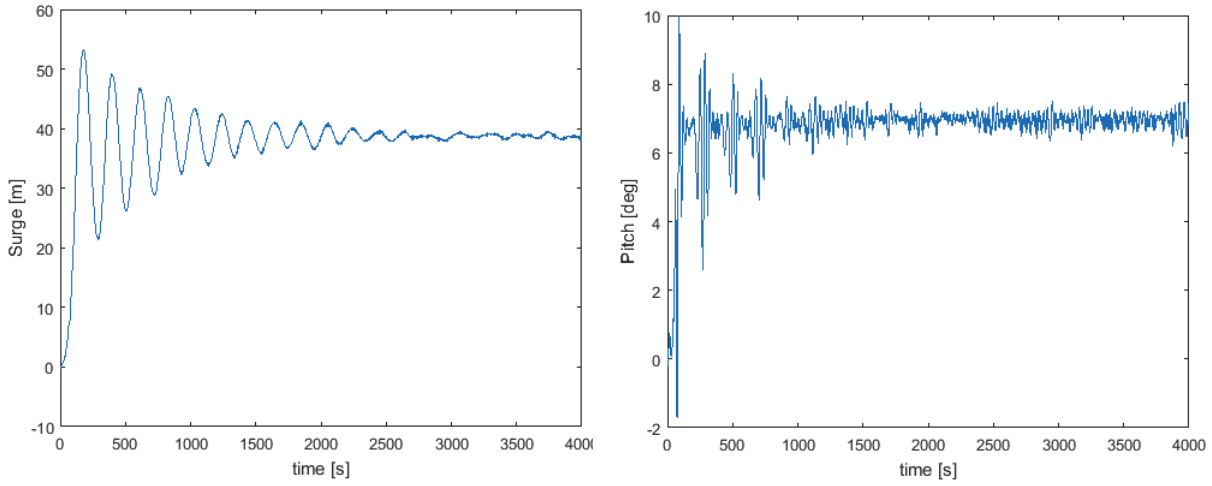

(a) Surge (b) Pitch

Figure 1.1: Time-series in surge and pitch of load case with rated wind speed [1]

	Surge $[m]$	Heave $[m]$	Pitch $[deg]$	Yaw $[deg]$
Mean Offset	38.72	-0.0567	6.95	0.0199
Max Offset	41.25	0.0929	7.52	0.1
Min Offset	35.72	-0.18	6.22	-0.09
RMS	0.8753	0.039	0.188	0.036

Table 1.2: Statistical data for platform motions at rated wind speed from project thesis [1]

The model made in the project thesis was concluded to be sufficient for further analyses. However, improvements that should be made in the Master thesis were to fix the errors

discovered from the constant wind test of the wind turbine, add a realistic mooring system, and account for second-order effects.

1.2 Scope of Thesis

The main objective of this thesis is to investigate the use of the OO Star 10 MW Wind Floater in 50 m water depth. The focus is aimed at the surge motion and the mooring line tension in coupled wind-current-wave conditions. In 50 m water depth, the mooring line tension increases non-linearly for a smaller offset than in deeper water. The surge motion is the main contributor to this increase. The surge motion and the mooring line tension were therefore considered the most relevant parameters to study.

In addition, an investigation of the applicability of different hydrodynamic load models is carried out. The motivation behind this is to find out if simplified models, such as strip theory and Newman's approximation, give satisfactory results. These simplifications reduce computational time significantly.

To achieve these goals, the work presented in the following list was planned to be carried out:

- Perform a literature study to address related work.
- Present the theoretical background of the simulation tools.
- Add realistic mooring system to the numerical model and account for second order effects.
- Carry out a verification study to verify the performance of the floating wind turbine, as well as a comparison of the numerical model with the realistic mooring system, and the model with mooring system designed as a linear spring.
- Perform a parameter study of the surge motion and mooring line tension based on time-domain simulations in SIMA. The behavior will be studied, and a comparison of the following hydrodynamic load models will be presented:
    1. Linear 3D-potential-flow loads
    2. Linear 3D-potential-flow loads + second-order loads from second-order transfer function
    3. Linear 3D-potential-flow loads + second-order loads from Newman's approximation

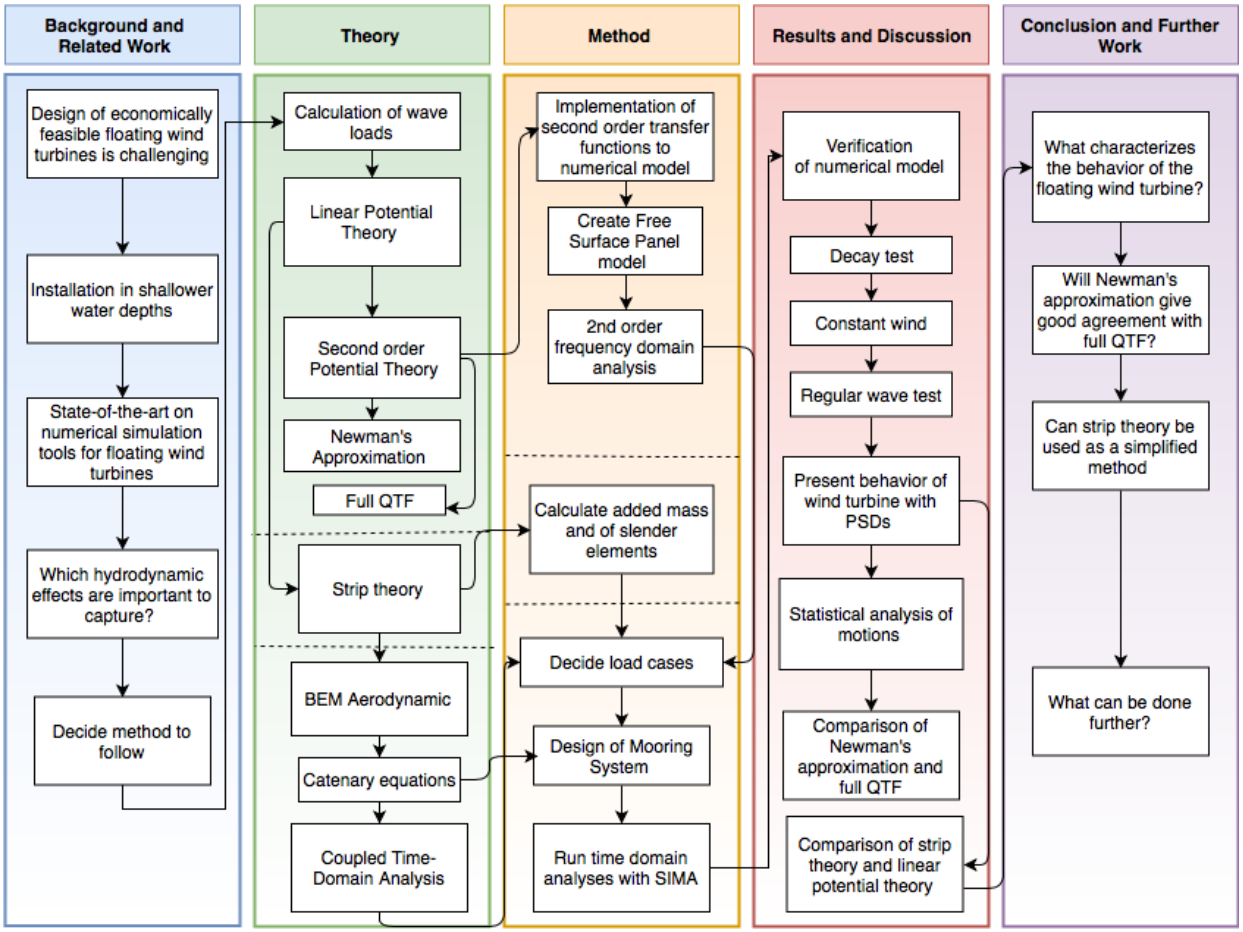

Figure 1.2: Workflow of Master thesis

4. Linear potential-flow with added mass and viscous drag terms calculated by strip theory.

Equal environmental load conditions was be applied for each hydrodynamic load model and the results are compared.

The workflow of the current project is presented in Figure 1.2.

1.3 Structure of Report

The structure of the report is listed below:

- **Chapter 2** considers the literature survey carried out on the state of the art on numerical analysis of floating wind turbines, effects of second-order loads and application of Morison's equation on semi-submersibles.

- **Chapter 3** describes the theory behind the simulations.

- **Chapter 4** provides the location site with corresponding environmental conditions and presents the load cases that were used in time-domain simulations.

- **Chapter 5** shows the method that was followed.

- **Chapter 6** presents a verification study of the numerical model.

- **Chapter 7** shows the results from the time-domain simulations and discusses the behaviour of the floating wind turbine.

- **Chapter 8** compares the different hydrodynamic load models by analyzing results from time-domain simulations.

Chapter 2

Literature

A literature study was conducted to gather information about related work, as well as to address relevant hydrodynamic effects that should be taken into account.

2.1 Numerical Analyses and Simulation Tools

This section provides a literature survey concerning numerical analyses and simulation tools applied to floating wind turbines. Some of the following paragraphs were taken directly from the project thesis [1].

To perform a full numerical analysis on a floating wind turbine, the numerical tool must be able to couple aerodynamics, hydrodynamics, structural and mooring line dynamics and control dynamics [12]. Several different tools are developed to perform this type of analysis. One of these tools is SIMA, which is a workbench combining the codes SIMO and RIFLEX [6].

SIMA is an aero-hydro-servo-elastic numerical tool. Hydrodynamic properties obtained from a first and second-order potential theory frequency domain analysis with Wadam can be imported into SIMA. For the hydrodynamic time-domain analyses, SIMA combines Morison's equation and first and second-order potential theory [13]. Regarding the aerodynamics, the BEM model is implemented.

In the oil and gas sector, frequency domain analyses are frequently used [12]. However, this is not sufficient for floating wind turbines. A frequency domain analysis can be used in the preliminary design states and is relatively good for calculating natural frequencies, which are important to obtain in the early design stages. On the other hand, the frequency domain analysis does not account for non-linear dynamics, nor

can it capture transient events. A floating body fastened with a mooring system will experience both these phenomenons, and a time-domain analysis is therefore required.

Lopez-Pavon [14] studied the wave-induced second-order forces on semi-submersible floating wind turbine mooring system. Second-order forces measured from model tests were compared with numerical results obtained by the second-order module of the WAMIT-code, which is implemented in Wadam in HydroD. The comparison showed that the numerical method captured the main trend in the behavior of second-order forces, but under predicted the loads compared to the model tests even with the full quadratic transfer function (QTF).

Lopez-Pavon and Souto-Iglesias [15] studied hydrodynamic forces on heave plates for semi-submersible floating wind turbines. Results from numerical simulations were compared with model tests. The results showed that the added mass coefficient obtained with from potential theory in Wadam were underestimated compared to the added mass coefficients from the model tests.

Since potential theory does not account for viscosity, viscous damping has to be added to the model in the time-domain simulations. Ishihara and Zhang [16] proposed to include this by adding drag coefficients from Morison's equation to slender elements of the body. An augmented Morison's equation correcting for frequency dependency of the drag force and the added mass was developed. However, this dependency is not corrected for in SIMO.

One of the main challenges design codes are facing today is the computational capacity [12]. Several programs are put together under the same workbench to perform the coupled analysis. Poor communication between different programs causes long simulations that are unfavorable since it is required to do several simulations in different environmental and operating conditions to capture the wind turbines behavior in all environmental conditions.

According to the literature survey conducted on the numerical analyses and simulation tools, the potential flow solver Wadam was decided to be used to carry out a frequency domain analysis on the floating sub-structure. A time-domain simulation would then be required to combine aerodynamics with hydrodynamics. This was decided to be carried out with SIMA. It was expected that the potential theory solution would underestimate the second-order difference-frequency loads and the added mass in heave due to the heave plates.

Due to the challenge regarding computational capacity, a simplified method of calculating wave loads using strip theory was considered. It was therefore decided to carry out a literature study concerning Morison's equation and strip theory applied to semi-submersibles.

2.2 Effect of Second-Order Wave Loads

Second-order effects were neglected in the project thesis. A literature survey was conducted to highlight the importance of these effects and on hydrodynamic load models used to obtain the second-order forces. The effect of these load models at shallower water depths is also considered.

Xu, Gao, and Moan [17] studied the effect of hydrodynamic load modeling on responses of floating wind turbines in shallow water. Three different water depths were used in the analyses. The reference mooring system was designed for 200 m water depth, and this mooring system was modified to be applicable for water depths of 100 m and 50 m. The study showed that the contribution from difference-frequency becomes more critical as the water depth decreases. This means that when obtaining the responses of the floating wind turbine, Newman's approximation is not sufficient and underestimates the low-frequency motions compared to results obtained with a full quadratic transfer function (QTF). A proper estimation of low-frequency motions is essential to capture the mooring line tension particularly at small water depths, since the tension increment of the turbines installed at 50 m becomes nonlinear earlier than for deeper water. Also, the results showed that the mooring line tension is more sensitive to wave loads compared to wind loads.

The effects of second-order hydrodynamic forces on floating offshore wind turbines were investigated by Duarte, Sarmento, and Jonkman [18]. The analyses showed that when there are no wind loads, second-order loads are visible for low frequencies which are below the wave range. From a power spectral density graph, it could be seen that the pitch motion larger for the load model accounting for second-order effects. This large motion was caused by difference-frequency loads. The model using Newman's approximation did not catch this increased movement. No significant contribution from sum-frequencies was made to the second-order effects. The effects of second-order loads were found to be reduced when the turbine is operating since the wind loads dominate. For extreme load cases, it was found that the difference-frequency loads had a minor effect

Hauteclocque, Rezende, Waals, and Chen [19] carried out a study on approximations used to evaluate the part of the QTF depending on the second-order velocity potential. The goal of the study was to find out which approximation was most efficient and at the same time, most accurate. The findings showed that the what defines most accurate method, depends on the water depth and the resonance period of the mooring system. In shallow water where the mooring system is most likely to be stiff, it is essential to calculate the full QTF since second-order waves have an important impact on the QTF also at very low difference-frequencies. This impact is not accounted for with Newman's approximation. In the case of an LNG carrier, results showed that for

difference-frequencies up to 0.15 rad/s, the indirect method of calculating the QTF, neglecting the free surface integral could be applied.

Simos, Ruggeri, Watai, Souto-Iglesias, and Lopez Pavon [20] investigated the effects of different frequency domain methods of estimating the slow-drift of a floating wind turbine. Results showed that Newman's approximation underestimated the slow-drift motions, and results obtained when using the full QTF showed good agreements with results obtained from a model test. When the second-order potential was disregarded when calculating the QTF, the results were still close to the results obtained with the full QTF.

According to the literature review on second-order effects, it was expected that Newman's approximation would underestimate the low-frequency motions and that a full QTF was necessary to capture the effects correctly, especially at shallower water depths. However, simulations applying Newman's approximation was decided to be carried out to evaluate the applicability of this approximation for the OO Star 10 MW Wind Floater at 50 m water depth.

2.3 Morison's Equation Applied on Semi-Submersibles

As mentioned, it is computationally costly to perform frequency domain analyses. An alternative, is to apply Morison's equation instead. This section provides a literature review on studies that have applied Morison's equation to a semi-submersible platform.

Kvittem, Bachynski, and Moan [21] studied the effects of hydrodynamic load models of a semi-submersible wind turbine. This was done by comparing platform motions calculated from linear potential theory and Morison's equation. Quadratic drag elements were included in both models to account for some viscous effects. A potential theory solution in the frequency domain was carried out with Wadam by a panel method to obtain the force and motion transfer functions, and retardation functions. These results were imported into SIMA, where time-domain analyses were performed. The application of Morison's equation was carried out directly with SIMA. Added mass terms were added to each element of the semi-submersible platform. These were calculated from Equation 2.1 for the horizontal forces on columns and Equation 2.2 for vertical forces on the heave plates. The added mass coefficients, C_a, were calculated based on the added mass obtained from the potential theory solution. The coefficients are frequency dependent. Thus, for regular wave tests, different C_a were used for each wave period. For irregular waves, the C_a corresponding to the peak period was used. For the Morison model, four different methods were used. One with forces integrated up to the mean water level, one with forces integrated up to wave elevation, pure Mori-

son with the effect of calculating the forces at an instantaneous position and one with a correction for the dynamic pressure under the columns.

$$m_a^{hor} = \rho_w C_a^{hor} \pi R_{col}^2 L_{col} \tag{2.1}$$

$$m_a^{ver} = \rho_w C_a^{ver} \frac{2\pi}{3} R_{plate}^3 \tag{2.2}$$

Regular wave tests and analyses with coupled wind-wave simulations were carried out. The results showed that the pure Morison model overestimated pitch and heave motions compared to potential theory, but when forces above the mean water level were included, the results showed a better agreement. The conclusion states that the Morison model is sufficient compared to the potential theory solution for wave periods between 7-21 seconds. For smaller periods, diffraction forces were important which are not accounted for by Morison's equation for small wavelengths and larger periods, the coupling between surge and pitch was not well captured with the Morison model.

The study of Ishihara and Zhang [16] developed a fully coupled simulation tool based on an augmented Morison's equation with proposed correction factors for hydrodynamic coefficients accounting for the effects of frequency and KC-dependency. The results obtained with the new model with the corrected hydrodynamic coefficients showed good agreement with results from free decay tests carried out in a water tank with a model of the floating wind turbine. A comparison was made between the augmented Morison's equation, the conventional Morison's equation where the hydrodynamic coefficients were not corrected and a model test. This comparison showed that the conventional Morison's equation underestimated the heave and pitch motions in the high-frequency region and overestimated them in the low-frequency region compared to the model tests, while the augmented Morison model showed good agreement with the model test.

Xu, Shao, Gao, and Moan [22] studied fully nonlinear wave load effects on a floating wind turbine in intermediate water depth. HAWC2 was used as the simulation tool which uses Morison's equation to calculate the wave loads and floater motions from time-domain analyses. Linear and fully nonlinear waves, with linear and fully nonlinear free surface boundary conditions, were generated in a 2D HPC numerical wave tank with the same random seed number. The floater motion and mooring line tension were compared for the linear waves and the fully nonlinear waves, representing extreme environmental conditions. The results showed that the surge motion and mooring line tension were underpredicted when the linear wave model was used compared to the fully nonlinear wave model.

From the literature review, it was decided that a strip theory approach should be applied as an alternative to frequency domain analysis. SIMA allows for user-defined added mass terms of slender elements[23], and these were decided to be calculated based on potential theory. With this method, only one simulation tool is required instead of three. It was expected that this model was sufficient for wave periods between 7-21 seconds, but that it would underestimate heave and pitch motions at high wave frequencies and underestimate them at low frequencies. Some errors were also expected due to the frequency and KC-dependence of the added mass coefficients, which was not taken into account in SIMA.

Chapter 3

Theory

This chapter provides the theory and mathematical background behind the analyses carried out in the current project. Most of the theory was taken from *Sea Loads on Ships and Offshore Structures*, written by O.M Faltinsen [2].

3.1 Wave Loads

Irregular wave theory is important when defining the environmental conditions which a floating structure will be subjected to. Thus, this theory is explained in the following section. Most of the theory in the following section was taken from the project thesis [1].

3.1.1 Irregular Wave Theory

Linear waves are used to simulate irregular sea. This is done by obtaining statistical estimates of a sea state composed of several linear waves [2]. The wave elevation of long-crested irregular sea is obtained by superposing individual linear waves:

$$\zeta = \sum_{j=1}^{N} \zeta_j \sin(\omega_j t - k_j x + \epsilon_j) \tag{3.1}$$

Where ζ_j is the wave amplitude and ϵ the phase angle of a wave j. The sea state is often expressed by a wave spectrum which describes the wave energy in the frequency domain. The amplitude can also be expressed from the frequency domain by a spectrum, as

shown in equation 3.2 where $S(\omega)$ represents the spectrum and ω the wave frequency.

$$\frac{1}{2}\zeta_j^2 = S(\omega_j)\Delta\omega \tag{3.2}$$

Figure 3.1 shows how the wave spectrum described in the frequency domain is connected to the wave amplitude described in the time-domain. As mentioned previously, the sea

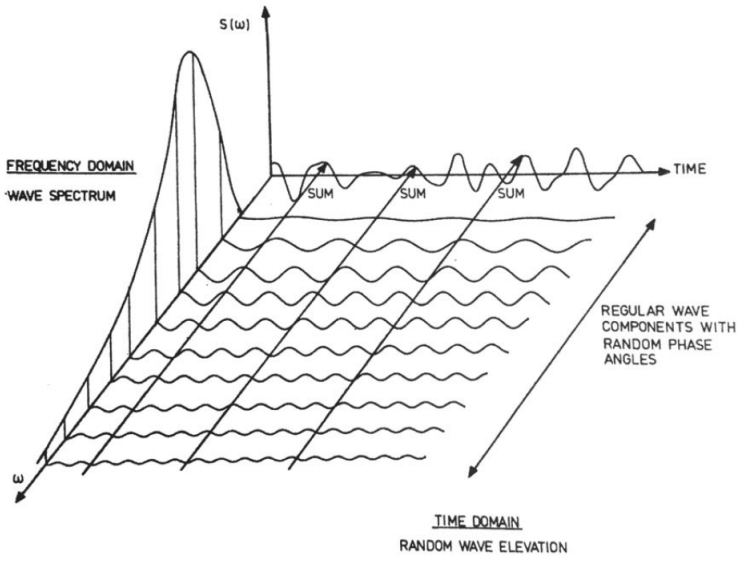

Figure 3.1: Connection between frequency and time-domain [2]

state is often described by statistical estimates. These are often expressed with the spectral moments. These are defined as:

$$m_k = \int_0^\infty \omega^k S(\omega) d\omega \tag{3.3}$$

Some of the most important statistical parameters which are obtained from the spectral moments are expressed below:

- **Significant wave height, $\mathbf{H_s}$:** The significant wave height gives the wave height, which is exceeded by 1/3 of the waves. Its expression is given as:

$$H_{\frac{1}{3}} = 4\sqrt{m_0} \tag{3.4}$$

- **Variance, $\boldsymbol{\sigma^2}$:** Gives the variance of the wave elevation and is given as the zero moment and has the expression:

$$\sigma^2 = m_0 = \int_0^\infty S(\omega) d\omega \tag{3.5}$$

- **Peak period, T_P:** The top frequency is the given frequency where the spectrum has its maximum value.

3.1.2 Wave Spectrum

A wave spectrum is used to graphically present sea states composed of irregular waves [3]. Different locations require different spectra since the sea states vary from site to site. Standardized spectra are created to resemble sea states, and spectral parameters are fitted to a certain location. An example of a standardized spectrum is the Pierson-Moskowitz (PM)-spectra which is expressed as

$$S(\omega) = \frac{A}{\omega^5} exp(-\frac{B}{\omega^4}) \tag{3.6}$$

The spectra based on the standardized PM-spectra have one peak, are valid for fully developed sea states and have a steep front at low frequencies. An example of a spectrum based on the PM-spectrum is the JONSWAP("Join North Sea Wave Project") spectrum. This was developed after a measuring project in the southeastern part of the North Sea. This spectrum uses the peak frequency instead of the wind speed as a parameter, and the A and B in the PM-spectrum are expressed as

$$A = \alpha g^2 \quad \text{and} \quad B = \frac{5}{4}\omega_p^4 \tag{3.7}$$

Where ω_p is the frequency corresponding to the peak period. To obtain the JONSWAP-spectrum, Equation 3.6 is multiplied by the factor

$$\gamma \left[-\frac{1}{2} \left(\frac{\omega - \omega_p}{\sigma \omega_p} \right)^2 \right] \tag{3.8}$$

The total expression for the JONSWAP spectrum becomes

$$S(\omega) = \alpha \frac{g^2}{\omega^5} exp \left[-\frac{5}{4} \left(\frac{\omega_p}{\omega} \right)^4 \right] \tag{3.9}$$

where γ is the peak parameter, α defines spectrum shape in the high frequency range and σ is defined in Figure 3.2.

The total energy in a JONSWAP spectrum and PM spectrum will be the same for the same sea state, but the energy is more concentrated around the peak for the JONSWAP than for the PM spectrum. The JONSWAP spectrum is considered to be a good model for wind-generated sea. However, when swell is present in the sea state, a one-peaked JONSWAP spectrum is not sufficient to describe the current sea state. The Metaocean

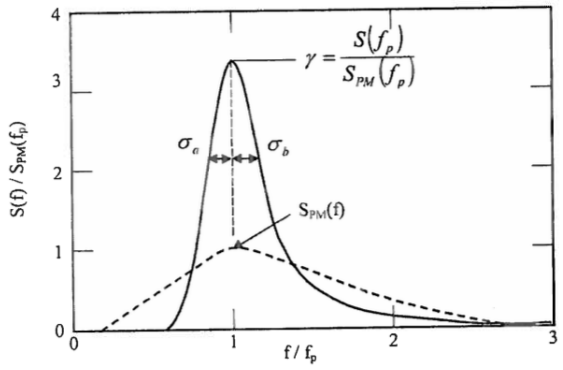

Figure 3.2: JONSWAP and PM Spectrum describing the same sea state [3]

design basis suggests that the Torsethaugen spectrum shall be applied when swell is present. This spectrum combines a JONSWAP spectrum for wind sea and swell sea. At the coast of the UK and Norway, the limit defining if wind or swell sea is dominant in the T_P, H_S-domain is defined in equation 3.10.

$$T_f = 6.6H_S^{1/3} \tag{3.10}$$

If $T_P < T_f$, wind sea is dominating. However, if the peak period of a sea state is within ± 2 s, JONSWAP can be applied. According to Li et al. [24], the sea state in the central North Sea located at the east coast of Scotland is mainly wind dominated since this area is not exposed to open sea. Therefore, the JONSWAP spectrum will be used as the spectrum for the given sea state in simulations for this project.

3.2 Hydrodynamic Load Models

The theory concerning hydrodynamic load models was taken from [2]. Different hydrodynamic load models can be applied to calculate the wave loads on a structure. Examples of such load models are potential theory and Morison's equation. Morison's equation is normally used to calculate wave loads on slender elements with a small diameter compared to the wavelength. Potential theory is used when diffraction forces are important, and when the structure does not consist of slender elements. In the current project, all calculations were performed based on potential theory, but the viscous drag term of Morison's equation was added to the substructure of the wind turbine to account for some viscous damping.

To decide which hydrodynamic load model to apply on a floating body, the dominating forces on the structure should be addressed. Figure 3.3 shows the importance of the

mass, viscous drag, and diffraction forces for different wave height-to-diameter and wavelength-to-diameter ratios of a fixed cylinder.

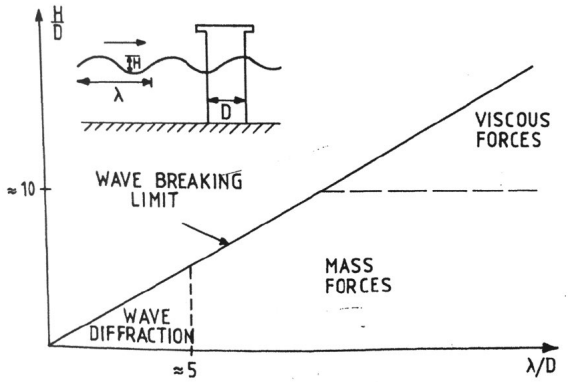

Figure 3.3: Importance of viscous drag, mass and diffraction forces on a marine structure [2]

Even though the current project did not consider a fixed cylinder, this graph can be used as an indication of which effects are important and thus be used as a tool when choosing the hydrodynamic model used for analyses. For a floating semi-submersible as considered in this thesis, the wave length-to-diameter ratio is large, and the wave-height to diameter ratio is small. This indicates that mass forces will dominate. The following sections provide detailed explanations of the first and second-order wave potential theory and Morison's equation, and how these theories were applied to calculate the wave forces and motions.

3.2.1 First-Order Potential Theory

First-order potential theory is applied to large volume structures where diffraction forces are important. Diffraction forces are found when the floating body is restrained from oscillating, and incident waves are acting [2]. The unsteady fluid pressure field from these incident waves will change due to the presence of the structure and the force causing this is called diffraction force.

Potential theory is applied in Wadam by a panel method. By frequency domain calculations, hydrodynamic properties of the body are obtained. To find the radiation and diffraction effects on the body, a linear boundary value problem for incompressible, inviscid flow, expressed with the complex velocity potential of the flow has to be solved [25]. The solution is solved at the mean position of the free surface and is linear with the wave amplitude. The velocity potential for an incident wave is defined as

$$\phi = \frac{ig\zeta_a}{\omega}\frac{\cosh k(z+h)}{cosh(kh)}\exp\left(-ik(xcos\beta + ysin\beta)\right) \tag{3.11}$$

where ζ_a is the wave amplitude, ω is the wave frequency, k is the wave number, h is the water depth, and β is the angle between the propagation direction and the x-axis.

According to linear potential theory, finding the wave loads acting on a floating structure can be divided into two problems. The first problem deals with wave excitation loads acting on the body when it is restrained from oscillating, and there are incident waves. These forces and moments are divided into Froude-Krylov and diffraction forces. The second problem is called the radiation problem and includes the forces acting on the floating body when it is forced to oscillate with the wave frequency, and there are no incident waves. These forces and moments are called added mass, damping, and restoring.

In Wadam, these two problems are found by decomposing the velocity potential into a radiation component and a diffraction component[25]:

$$\phi = \phi_D + \phi_R \tag{3.12}$$

where

$$\phi_R = i\omega \sum_{j=1,6} \eta_j \phi_j \qquad \phi_D = \phi_0 + \phi_7 \tag{3.13}$$

η_j is the complex amplitudes of the oscillating motions in each degree of freedom and ϕ_j is the unit-amplitude radiation potentials. ϕ_D is the disturbance by the body of the incident wave, and ϕ_0 is the incident wave potential.

The forces and moments are found by integrating the fluid pressure, which is a function of the velocity potential, over the body. By applying Newton's second law and setting the two sub-problems equal to each other, the 1-degree of freedom(DOF) frequency dependent equation of motion using linear potential theory becomes:

$$\Sigma_{k=1}^{6}[(M_{jk} + A_{jk})\ddot{\eta}_k + B_{jk}\dot{\eta}_k + C_{jk}\eta_k] = F_j e^{-i\omega_e t} \quad (j = 1, .., 6) \tag{3.14}$$

M_{jk} is the mass of the body, A_{jk} is the added mass, B_{jk} is the radiation damping, C_{jk} is the restoring term and F_j is the complex amplitude of the excitation forces. The index k indicates in which direction the body moves due to the load in the direction j.

The equation of motion is solved with Wadam by applying a three-dimensional panel method. This method is described in detail in the WAMIT-manual [25].

3.2.2 Second-Order Potential Theory

For a moored semi-submersible structure, second-order effects become important due to the high natural periods in surge, sway and yaw caused by the mooring system [2]. Second-order potential theory accounts for the instantaneous position of the floating body. The problem is not solved exactly, but all involving terms are linear or proportional to the square of the wave amplitude.

If the body is moving in the vertical direction, the part of the body closest to the water surface will move in and out of the water. If the pressure field in a point at this part of the body is examined with Bernoulli's equation, a non-zero mean term appears in addition to one term dependent on the difference and one term dependent on the sum of two frequencies, found in the wave spectrum. For a moored semi-submersible, the term dependent on the difference-frequency is important because it might get close to the natural periods of the structure in surge, sway and yaw and excite large motions.

Mean Drift Loads

The mean term of the resulting pressure on the body is called mean wave drift load. This load exists due to the floating body's ability to create waves [2]. Normally, mean drift forces are small for structures where mass forces dominate, such as for a semi-submersible.

The pressure obtained from the second-order velocity potential has zero mean, and the second-order velocity potential does therefore not contribute to the mean drift forces. Consequently, only the first-order velocity potential is necessary to calculate the mean drift loads. One method to calculate the mean drift force is by applying conservation of momentum in the fluid. The equations for the mean drift load obtained from conservation of momentum can be written as:

$$\overline{F_i} = -\overline{\iint_{s_\infty} [pn_i + \rho V_i V_n] ds} \qquad i = 1, 2 \tag{3.15}$$

$\overline{F_i}$ is the resulting mean force on the body, S_∞ is the time-dependent wetted surface, p is the pressure which can be calculated with Bernoulli's equation, V_i is the fluid velocity and V_n is the normal component of the velocity at the surface S. The expression of the mean drift force is used to calculate the mean drift in surge and sway, but with some adjustments it is also possible to calculate the mean drift moment in yaw.

Direct pressure integration can also be used to calculate the mean drift forces. The complete Bernoulli's equation is used and integrated over the exact wetted surface.

The hydrodynamic problem has to be solved to higher-order in wave amplitude. The sum of the integrated terms in Bernoulli's equation becomes $(\rho g/2)\zeta_a^2$, which is the correct asymptotic value. The generalized asymptotic formula which can be used for long-waves can then be written:

$$\overline{F_i} = \frac{\rho g \zeta_a^2}{2} \int_{L_1} \sin^2(\theta + \beta) n_i dl \tag{3.16}$$

$\overline{F_i}$ is the drift force, ζ_a is the wave amplitude, θ is the angle of the hull, β is the wave propagation direction and L_1 is the non-shadow part of the water plane curve.

The mean drift forces are calculated with both methods in Wadam. Section 6.4 provides a comparison of the results obtained with the two models.

Slow-Drift Motions

Slow-drift motions occur in irregular sea due to non-linear interaction effects between the waves and motions of the platform. For a floating wind turbine that is freely floating and connected to the sea bottom with a mooring system, slow-drift motions occur in surge, sway and yaw. As mentioned earlier, if the pressure from the waves on the floating body is investigated with Bernoulli's equation, it can be seen that one of the terms in the total pressure is dependent on the difference-frequency of two incoming waves with different frequencies. The second-order velocity potential is necessary to calculate the slow-drift loads. The total excitation loads on the body from slow-drift motions, F_i^{SV} can be written:

$$F_i^{SV} = \sum_{j=2}^{N} \sum_{k=2}^{N} \zeta_j \zeta_k [T_{jk}^{ic} cos\{(\omega_k - \omega_j)t + (\epsilon_k - \epsilon_j)\} + T_{jk}^{is} sin\{(\omega_k - \omega_j)t + (\epsilon_k - \epsilon_j)\}] \tag{3.17}$$

ζ_i are the wave amplitudes, ω_i is the wave frequency, ϵ_i are the random phase angles and, T_{jk}^{is} and T_{jk}^{ic} are the quadratic transfer functions(QTF) for the difference-frequency loads. F_i^{SV} can be calculated in all 6 degrees of freedom. The diagonal terms of the second-order transfer functions correspond to the mean drift force.

To calculate the QTFs, a free surface mesh is needed since a panel method is used in WADAM. Direct pressure integration is used to obtain the transfer functions from a second-order analysis in the frequency domain.

Newman's Approximation

Calculating the full quadratic transfer functions for a broad frequency domain is computationally costly. Newman's approximation is a simplified method that can be used to calculate the second-order slow-drift motions. According to [2], the approximation is based on the assumption that T^{ic}_{jk} and T^{is}_{jk} can be approximated by T^{ic}_{jj}, T^{ic}_{kk}, T^{is}_{jj} and T^{is}_{kk}. This works because T^{ic}_{jk} and T^{is}_{jk} normally do not change a lot with frequency. Since the difference-frequencies that are close to the resonance oscillation frequencies usually are very small, the second-order transfer functions can be approximated to their values on the line $\omega_j = \omega_k$. This means that only the mean drift forces are used to obtain the QTFs. The second-order transfer functions T^{ic}_{jk} and T^{is}_{jk} becomes:

$$T^{ic}_{jk} = T^{ic}_{kj} = 0.5(T^{ic}_{jj} + T^{ic}_{kk}) \tag{3.18}$$

and

$$T^{is}_{jk} = T^{is}_{kj} = 0 \tag{3.19}$$

Which then can be directly inserted into equation 3.17. However, to simplify this equation one more time, the double summation can be replaced by the square of a single series. The final slow-drift force using Newman's approximation can then be written as:

$$F^{SV}_i = 2\Big(\sum_{j=1}^{N} \zeta_j (T^{ic}_{jj})^{\frac{1}{2}} \cos(\omega_j t + \epsilon_j)\Big)^2 \tag{3.20}$$

If the frequencies considered in the diagonal are close to the natural frequencies of motions with little damping, the approximation becomes less accurate. Newman's approximation is also less accurate for motions with lower natural periods such as heave, pitch and roll.

3.3 Morison's Equation

Morison's equation is semi-empirical and used to calculate wave loads on slender structures with a high wavelength-to-diameter ratio [26]. For these types of structures, viscous effects are important and hence Morison's equation is composed of two force terms, one inertia term and one viscous drag term. For potential theory, the hydrodynamic loads are found by looking at the velocity potential, while for Morison's equation, the loads are expressed with the undisturbed fluid particle velocity and acceleration.

Equation 3.21 shows the horizontal force of a unit length of a vertical cylinder expressed with Morison's equation. The first term of the equation is the drag force, and as can be seen, this force accounts for some non-linearity of the flow. The second term is the mass term accounting for Froude-Krylov forces and inertia forces. The advantage of using Morison's equation is that it can be solved in the time-domain, which is not the case when using potential theory. To obtain the total wave force, strip theory is applied, and the force dF at one strip is integrated over the length of the body.

$$dF = \frac{1}{2}\rho C_D D dz u|u| + \rho C_M \frac{\pi D^2}{4} dz a_1 \tag{3.21}$$

ρ is the water density, D is the cylinder diameter, u and a_1 are the fluid particle velocity and acceleration and C_D and C_M are the drag and mass coefficients. C_M and C_D are dependent on several parameters of the wave kinematics such as the KC-number, Reynolds number and roughness number and should be determined empirically. If viscous effects are negligible, the drag force of the Morison's equation is zero, and only the mass term of the Morison's equation is left:

$$dF = \frac{1}{2}\rho C_M \frac{\pi D^2}{4} dz a_1 \tag{3.22}$$

Where $C_M = C_a + 1$. If viscous effects are assumed negligible and the wavelength is much larger than the diameter($\lambda/D > 5$) of the body, long-wave approximation can be applied in potential theory. For this approximation, waves generated by wave-body interaction are small, and the damping contribution to the force can be neglected. According to potential theory with long-wave approximation the excitation force on a strip can be written as:

$$dF = \rho \frac{\pi D^2}{4} a_1 dz + C_a \rho \frac{\pi D^2}{4} a_1 dz \tag{3.23}$$

If C_a is equal to 1, Morison's equation when viscous effects are negligible is equal to the equation for excitation forces from potential theory on a strip when assuming long-wave approximation.

Strip theory can therefore be used as a simplified method to calculate the wave loads on slender elements when long-wave approximation is assumed. This means that potential theory is still valid, but a full frequency domain analysis is not necessary. In SIMO, the wave force acting on a strip on matrix form is defined as:

$$\boldsymbol{F_{WS}} = \rho V_s \boldsymbol{a_s} + \boldsymbol{m_h a_s} + (\boldsymbol{C_D}(\boldsymbol{U_c} + \boldsymbol{u_s} - \boldsymbol{\eta_s}))|\boldsymbol{C_D}(\boldsymbol{U_c} + \boldsymbol{u_s} - \boldsymbol{\eta_s})| \tag{3.24}$$

$\boldsymbol{F_{WS}}$ is the wave force on the strip, V_S is the volume of the strip, $\boldsymbol{a_s}$ is the water particle acceleration in the local strip coordinate system, $\boldsymbol{m_h}$ is the added mass, and $\boldsymbol{C_D}$ is the drag coefficient. $\boldsymbol{U_c}$ is the current velocity, $\boldsymbol{u_s}$ is the water particle velocity and $\boldsymbol{\eta_s}$ is the strip velocity component, all defined in the local strip coordinate system. When strip theory is applied, the added mass and drag from these equations are added to slender elements defined on the SIMO body.

Potential theory assumes an inviscid, incompressible flow. However, as seen in figure 3.3, viscous effects may become important when the wave period is close to the natural period of the structure. To account for the viscous effect, drag coefficients from Morison's equation are added to the elements of the platform for both the potential theory case and the case using strip theory.

When the floating wind turbine experiences large waves, the radiation damping is small, and viscous damping effects become important to provide damping to the resonant motions. This viscous damping can be expressed by the viscous drag term of Morison's equation.

3.4 Aerodynamics

3.4.1 Blade Element/Momentum Theroy

SIMA utilizes the blade element/momentum(BEM) theory for the aerodynamic calculations to obtain forces acting on the blades [27]. This theory allows for calculating steady loads, thrust and power for different wind speeds, rotational speeds and pitch angles. BEM is based on the 1-D momentum theory which models the rotor as an ideal disc and a stream tube resembles the incoming flow. The stream tube is discretized into N annular elements with height dr. Two assumptions are made for the elements: There is no radial dependency, and the rotor has an infinite number of blades. The rotor thrust and momentum can be found for each element and the expressions are presented in Equation 3.25 and 3.26, respectively.

$$dT = 4\pi r \rho U_W^2 a(1-a)dr \tag{3.25}$$

$$dM = 4\pi r^3 \rho U_W \omega (1-a)a'dr \tag{3.26}$$

U_W is the wind speed, $V_W(1-a)$ is the axial velocity and $\omega r(1+' a)$ is the tangential velocity, which is shown in figure 3.4.

Several corrections are applied to SIMA to make BEM applicable for real rotor blades, and some of these are listed below:

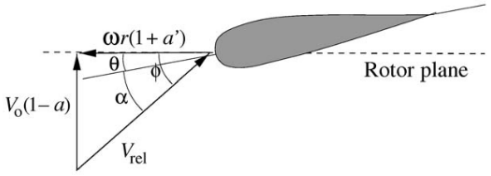

Figure 3.4: Airfoil section in rotor plane [4]

- Prandtl's tip loss factor is applied to correct the assumption that there is an infinite number of blades. The tip of the blade produces less aerodynamic force because the pressure gradient makes some of the air flow from the lower to the upper side of the blade. When adding this correction factor to the results from the blade element/momentum theory, this reduction in the aerodynamic force is taken into account [27].
- Glauert Correction for high values of a. When a >0.5, the BEM theory breaks down since this would make the velocity in the far end negative. In these cases, the Gluert correction factor is applied.
- Real rotor blades will experience a dynamic wake. This effect is due to a time lag in induced velocities that occurs because of shedding and downstream convection of vorticity. To account for this effect, a method of filtering the induced velocity has been made. It is necessary to obtain the real-time behavior of the flow so that the pitch of the blades can be adjusted when the thrust changes.
- Dynamic stall occurs due to dynamic changes in lift and drag coefficient values. These values are modeled as static in BEM, but attachments and re-attachment of the flow cause the coefficients to change. In SIMA, the Stig Øye method is used to correct for this which can be read about in [4].
- The tower shadow effect is included in SIMA. The presence of the tower affects the incoming flow when the blades pass the tower, and the resulting thrust variance can result in fatigue damage.

3.5 Coupled time-domain Analysis

To perform time-domain simulations, the results from the frequency domain calculations carried out with Wadam are imported to SIMA. With SIMA, the frequency dependent equation of motion(Equation 3.14) is solved by the convolution integral [23]. On matrix form the equation of motion can be written:

$$(\boldsymbol{M} + \boldsymbol{A}(\boldsymbol{\omega}))\ddot{\boldsymbol{\eta}} + \boldsymbol{B}(\boldsymbol{\omega})\dot{\boldsymbol{\eta}} + \boldsymbol{C}\boldsymbol{\eta} = \boldsymbol{f}(\boldsymbol{t}) \tag{3.27}$$

The terms that are independent of the frequency can be moved to the right side.

$$\boldsymbol{A}(\boldsymbol{\omega})\ddot{\boldsymbol{\eta}} + \boldsymbol{B}(\boldsymbol{\omega})\dot{\boldsymbol{\eta}} = \boldsymbol{f}(\boldsymbol{t}) - \boldsymbol{M}\ddot{\boldsymbol{\eta}} - \boldsymbol{C}\boldsymbol{\eta} \tag{3.28}$$

The added mass and damping terms are written as:

$$\boldsymbol{A}(\boldsymbol{\omega}) = \boldsymbol{A}_{\infty} + \boldsymbol{a}(\boldsymbol{\omega}) \tag{3.29}$$

$$\boldsymbol{B}(\boldsymbol{\omega}) = \boldsymbol{B}_{\infty} + \boldsymbol{b}(\boldsymbol{\omega}) \tag{3.30}$$

B_{∞} is zero, so the equation of motion in the frequency domain becomes:

$$-\omega^2 \boldsymbol{A}_{\infty}\boldsymbol{\eta}(\boldsymbol{\omega}) + (i\omega\boldsymbol{a}(\boldsymbol{\omega}) + \boldsymbol{b}(\boldsymbol{\omega}))i\omega\boldsymbol{\eta}(\boldsymbol{\omega}) = \boldsymbol{F}(\boldsymbol{\omega}) \tag{3.31}$$

To transform the equation into the time-domain, an inverse Fourier transform is applied. The equation of motion is then

$$\boldsymbol{A}_{\infty}\ddot{\boldsymbol{\eta}} + \int_{\infty}^{t} \boldsymbol{h}(\boldsymbol{t} - \boldsymbol{\tau})\boldsymbol{\eta}(\boldsymbol{\tau})\boldsymbol{d\tau} = \boldsymbol{f}(\boldsymbol{t}) \tag{3.32}$$

This equation is then added to Equation 3.28, and the total equation in the time-domain by becomes:

$$(\boldsymbol{M} + \boldsymbol{A}_{\infty})\ddot{\boldsymbol{\eta}} + \boldsymbol{C}\boldsymbol{\eta} + \int_{\mathbf{0}}^{t} \boldsymbol{h}(\boldsymbol{t} - \boldsymbol{\tau})\dot{\boldsymbol{\eta}}(\boldsymbol{\tau})\boldsymbol{d\tau} = \boldsymbol{q}(\boldsymbol{t}, \boldsymbol{\eta}, \dot{\boldsymbol{\eta}}) \tag{3.33}$$

The retardation function $\boldsymbol{h}(\boldsymbol{\tau})$ is obtained by a transform of the frequency dependent added mass and damping.

The excitation forces $\boldsymbol{q}(\boldsymbol{t}, \boldsymbol{\eta}, \dot{\boldsymbol{\eta}})$ can be separated into a high and low frequency part.

$$\boldsymbol{q}(\boldsymbol{t}, \boldsymbol{\eta}, \dot{\boldsymbol{\eta}}) = \boldsymbol{q}_{\boldsymbol{wave,1st}} + \boldsymbol{q}_{\boldsymbol{wave,2nd}} + \boldsymbol{q}_{\boldsymbol{current}} + \boldsymbol{q}_{\boldsymbol{wind}} + \boldsymbol{q}_{\boldsymbol{drag}} \tag{3.34}$$

$\boldsymbol{q}_{\boldsymbol{wave,1st}}$ and $\boldsymbol{q}_{\boldsymbol{wave,2nd}}$ are calculated by a frequency domain analysis in Wadam, $\boldsymbol{q}_{\boldsymbol{wave,2nd}}$ and $\boldsymbol{q}_{\boldsymbol{current}}$ is calculated with SIMO/RIFLEX based on the current values added to the environmental conditions, and $\boldsymbol{q}_{\boldsymbol{drag}}$ is calculated with the drag term of Morison's equation and strip theory is applied in SIMO.

3.6 Catenary Equations

The floating wind turbine is attached to the sea bottom with a mooring system consisting of three catenary anchor lines. These anchor lines provide stiffness to the platform due to the weight of the chains, and it is important to design a mooring system that is stiff enough to avoid large offsets. For the mooring system to be easy to move, the anchors cannot take on vertical forces and a part of the mooring line closest to the anchors must lie on the sea bottom. The mooring system used for the OO Star 10 MW Wind Floater in this thesis is described in detail in Section 5.4. To find the initial position of the anchors, an inelastic static analysis was performed with MATLAB. To carry out this analysis, the catenary equations described in [2] were applied.

Figure 3.5 shows a mooring line and its variables used for the analysis.

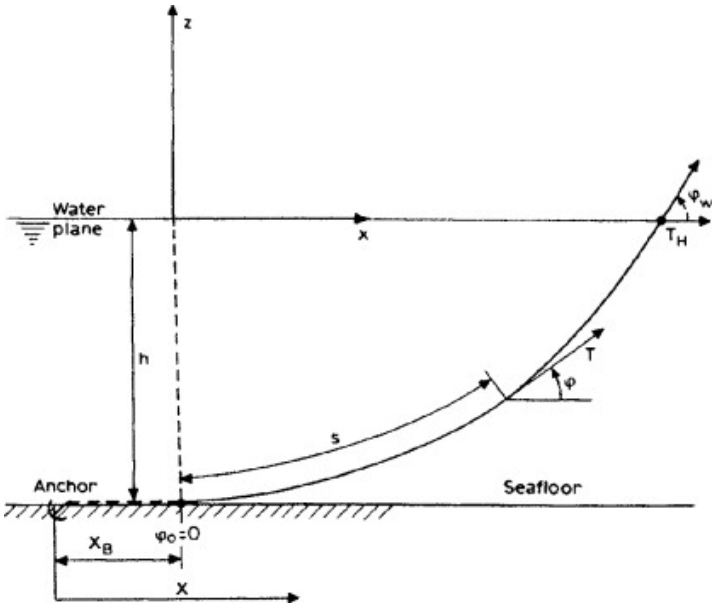

Figure 3.5: Variables of a mooring system [2]

The catenary inelastic equation assumes a horizontal seabed and the effect of elasticity is neglected. The length of the suspended line, l_s,and the vertically span, h, can be written as:

$$l_s = \left(\frac{T_H}{w}\right) sinh\left(\frac{wx}{T_H}\right) \tag{3.35}$$

and

$$h = \frac{T_H}{w}\Big[cosh\Big(\frac{wx}{T_H}\Big) - 1\Big] \tag{3.36}$$

Where T_H is the horizontal tension at the fairlead, w is the mooring line weight in N/m and x is the horizontal length of the suspended line. If these two equations are combined, the suspended line length becomes:

$$l_s^2 = h^2 + 2h\frac{T_H}{w} \tag{3.37}$$

When finding the position of the anchor lines, the variable X, which is the horizontal distance between the fairlead and the anchor needs to be found. This distance is written as:

$$X = l - l_s + x \tag{3.38}$$

However, it is important to find X as a function of T_H so that the mean position of the platform can be found for different load conditions. By putting Equation 3.37 and 3.36 into Equation 3.38, the Equation for X as a function of T_H becomes:

$$X = l - h\sqrt{1 + \frac{2T_H}{w}} + \frac{T_H}{w}\cosh^{-1}\Big(1 + \frac{hw}{T_H}\Big) \tag{3.39}$$

This equation was used to find the anchor positions for a given pre-tension T_H.

Chapter 4

Environmental Conditions

4.1 Site

The Buchan deep located on the east coast of Scotland was chosen as a site for the floating wind turbine due to its shallow water depths and its wind resources. The environmental conditions at this site were studied to find out which loads the floating wind turbine most likely would be subjected. The water depths at this region ranges from 30-140 m, and the average wind speed is at 10 m/s which makes this site suitable for a wind turbine that will be installed at 50 m water depth and with a rated wind speed of 11 m/s. In 2017, Equinor installed the worlds first floating wind turbine park at the Buchan deep. This farm consists of 5 6MW wind turbines which provide electricity to about 22,000 households [28]. A map showing the location is presented in Figure 4.1.

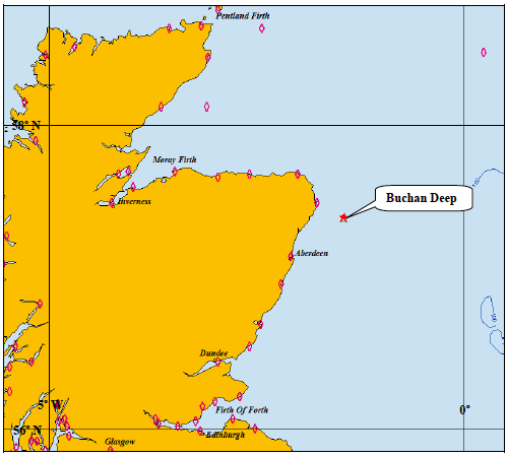

Figure 4.1: Location of Buchan Deep

4.2 Wind Loads

According to Li et al. [24], the power law wind velocity profile can be used at the current site with $\alpha = 0.1$ (Equation 4.1).

$$U_W(z) = U_{10}\left(\frac{z}{10}\right)^{\alpha} \tag{4.1}$$

U_{10} is the mean wind velocity at 10 m above water level and z is the vertical coordinate where z = 0 is at still water level. The power law profile was chosen in SIMA, where the horizontal velocity, direction, reference height, and wind shear exponent, α, were input parameters. The wind velocities for operational conditions chosen for the simulations were taken from the *Metocean design basis from the Buchan Deep* [29]. Two wind velocity for operational conditions were chosen. One corresponded to the annual mean value and one to a wind speed close to the cut-off velocity of 25 m/s. The annual mean value is the wind velocity that the wind turbine is most likely to experience, this velocity was 8.5 m/s, which at hub-height corresponded to 10.88 m/s. This is close to the rated wind velocity of 11.4 m/s, which gives a maximum thrust of the turbine. The wind speed right below cut-off was chosen to be 18.9 m/s, which also was chosen from [29] and corresponds to a random wind velocity that the wind turbine will experience during one year.

	Direction [°]	U_{10} $[m/s]$	U_{119} $[m/s]$
Mean annual	0	8.5	10.88
Close to cut-off	0	18.9	24.21

Table 4.1: Wind velocities used in simulations

In addition to operational conditions, a wind velocity corresponding to extreme conditions was chosen. The extreme values are defined as values that only appear one time within a certain period of time, and this amount of time is called the return period. The 50-year return period of the wind velocity is taken directly from the Metocean Data Design Basis [29] and is presented in Table 4.2.

Return Period $[years]$	Direction [°]	z a.s.l $[m]$	U_W $[m/s]$
50	0	10	28

Table 4.2: Extreme values for wind conditions(a.s.l = above sea level)

4.2.1 Wind Distribution Model

Realistic wind conditions include wind gusts and turbulence. To include this in the wind simulations, the tool TurbSim was used. This tool simulates numerical turbulent wind flows which can be imported into programs such as SIMA [30].

For the wind speeds below cut-off, the Normal Turbulence Model (NTM) defined in IEC 61400-1 [31] was used. An input-file was created to TurbSim where wind speeds at hub height were defined. NTM uses a power law distribution of the vertical wind speed and uses the average wind speed and the reference turbulence intensity, I_{ref}. The standard deviation of NTM is presented in Equation 4.2 [31]. The alpha factor of the power law distribution and the reference turbulence intensity were both chosen to be 0.1 in accordance with [24].

$$\sigma_1 = I_{ref}(0.75U_{hub} + 5.6) \tag{4.2}$$

For extreme conditions, the extreme turbulence model(ETM) was used. This was also created with TurbSim, and the standard deviation of this model is presented in Equation 4.3.

$$\sigma_1 = 2I_{ref}\big(0.072\big(\frac{U_{ave}}{2} + 3\big)\big(\frac{U_{hub}}{2} - 4\big) + 10\big) \tag{4.3}$$

4.3 Waves

According to [24], the sea state at the Central North Sea, which is located east of the UK is mainly composed of wind-generated waves since the location is not exposed to open ocean. Thus, the JONSWAP wave specttrum for wind-generated waves was used in the time-domain simulations in SIMA to simulate operational conditions for the wind turbine. The significant wave height, H_S, and the peak period, T_P, and the direction are input values that are required of SIMA.

Since wind sea is dominating at this site, a joint distribution of wind velocity, U_W, significant wave height, H_S and peak period T_P was used to find the wave height and wave period for the wind speeds given in Table 4.1. This joint distribution was found in [24], and the parameters of the distribution fitted to the Central North Sea were provided. The conditional probability distribution for the significant wave height for a given wind velocity is given as:

$$F_{H_S|U_W}(h|u) = \frac{\alpha_{HC}}{\beta_{HC}}\Big(\frac{h}{\beta_{HC}}\Big)^{\alpha_{HC}-1} exp\Big[-\Big(\frac{h}{\beta_{HC}}\Big)^{\alpha_{HC}}\Big] \tag{4.4}$$

α_{HC} and β_{HC} are the shape and scale parameters and can be obtained by:

$$\alpha_{HC} = a_1 + a_2 u^{a_3} \tag{4.5}$$

$$\beta_{HC} = b_1 + b_2 u^{b_3} \tag{4.6}$$

a_1,a_2, a_3,b_1,b_2 and b_3 are parameters estimated from data at each location. The expected value of H_S for a given U_W is:

$$E[H_S|U_W] = \alpha_{HC}\Gamma\left(1 + \frac{1}{\beta_{HC}}\right) \tag{4.7}$$

The parameters used to calculate the expected value are fitted to the environmental conditions at the Central North Sea and are presented in Table 4.3.

Parameter	a_1	a_2	a_3	b_1	b_2	b_3
Value	1.755	0.184	1	0.534	0.07	1.435

Table 4.3: Parameters used for calculating E[$H_S|U_W$]

The joint conditional distrubution was based on the Weibull-distribution, so a built-in MATLAB function was used to calculate the expected value based on the given parameters. The expected value of the significant wave height for $U_W = 8.5m/s$ and $U_W = 18.9m/s$ resulted to be 1.83 m and 5.23 m, respectively. The mean value of T_P for the given H_S and U_W was calculated based on the lognormal conditional distribution given in Equation 4.8.

$$f_{T_P|H_S,U_W}(t|h,u) = \frac{1}{\sqrt{2\pi}\sigma_{ln(T_P)}t} exp\left[-\frac{1}{2}\left(\frac{ln(t) - \mu_{ln(T_P)}}{\sigma_{ln(T_P)}}\right)^2\right] \tag{4.8}$$

The mean value for this distribution at the given significant wave height found from Equation 4.7 and a given wind velocity is calculated by applying Equation 4.9

$$E[T_P|H_s, U_W] = E[T_P(H_S)]\Big[1 + \theta\Big(\frac{u_w - E[U_W(h)]}{E[U_W(h)]}\Big)^{\gamma}\Big] \tag{4.9}$$

$E[U_W|H_S]$ and $E[T_P|H_S]$ are expected wind velocity and peak period for a given significant wave height and are location dependent. The values were obtained from Equation 4.10 and 4.11.

$$E[T_P|H_S] = e_1 + e_2 h^{e_3} \tag{4.10}$$

$$E[T_P|H_S] = f_1 + f_2 h^{f_3} \tag{4.11}$$

The parameters that were used to calculate the mean value of T_P were taken from [24] and are presented in Table 4.4.

Parameter	e_1	e_2	e_3	f_1	f_2	f_3	θ	γ
Values	5.563	0.798	1	3.5	3.592	0.735	-0.477	1

Table 4.4: Parameters used to calculate $E[T_P|H_S,U_W]$

The mean value of T_P obtained from these parameters corresponding to wind velocities 8.5 m/s and 18.9 m/s were 7.25 s and 10.71 s, respectively.

For the extreme conditions, the 50-year return-period of significant wave height and the corresponding peak period was used. These were obtained from the *Metocean Design Basis of the Buchan Deep* and are presented in Table 4.5

	H_S $[m]$	T_P $[s]$
Values	10.01	14.0

Table 4.5: H_S and T_P for extreme conditions

4.4 Current

The current which the floating wind turbine is exposed to is combosed of wind-generated current and tidal current. The total current profile is taken from DNV GLs *Recommended Practice on Environmental Conditions and Environmental Loads* [32] and can be expressed as the sum of the wind current and the tidal current components as can be seen from Equation 4.12.

$$U_c = U_{c,wind} + U_{c,tidal} \tag{4.12}$$

The wind current and tidal current profiles are presented in equation 4.13 and 4.14, respectively.

$$U_{c,wind} = U_{c,wind}(0)\left(\frac{d_0 + z}{d_0}\right) \tag{4.13}$$

$$U_{c,current} = U_{c,tidal}(0)\left(\frac{d + z}{d}\right)^{1/7} \tag{4.14}$$

$U_{c,wind}(0)$ and $U_{c,tidal}$ are the current velocities at the mean surface line. The parameter d_0 represents the reference depth for wind-generated current and d is the water depth. The Metaocean data from the Buchan Deep [29] gives a directional sample distribution of the total current speed in this region. Since the joint distribution for wind and current not is given in Li et al. [24] nor in the Metocean data, the annual mean current at 0 degrees was selected. The input for the current in SIMA is the current velocity at a certain water depth. Table 4.6 shows which values are used in the simulations.

Direction [°]	Water Depth $[m]$	$U_C[m/s]$
0	25	0.373

Table 4.6: Current speed used in simulations

The extreme values for current are taken as the current velocity with a 50 year return period and are taken from [29]. The value that was used in the simulations is presented in Table 4.7.

Return period $[years]$	Water Depth $[m]$	Direction [°]	U_C $[m/s]$
50	25	0	1.29

Table 4.7: Extreme values for current

4.5 Load Cases

Based on the environmental conditions, six different load cases were established for the time-domain simulations. The purpose of creating these load cases was to study the motion responses and forces on the wind turbine subjected to different environmental conditions. Two of the load cases represent operational conditions, two represent the near cut-off conditions, and two represent extreme conditions. It was considered interesting to study the effect of hydrodynamic loads alone, without the wind loads. Three of the load cases were therefore defined without wind, and three were defined with. This made it possible to investigate which loads were dominant on the floating wind turbine.

Table 4.8 shows the load cases used in the simulations. O.1, C.1 and X.1 do not include wind, while O.2, C.2 and X.2 include wind.

Load Case	H_s $[m]$	T_P $[s]$	$U_{C,25}$ $[m/s]$	U_W $[m/s]$	WM
O.1	1.83	7.25	0.373	-	-
O.2	1.83	7.25	0.373	8.5	NTM
C.1	5.23	10.71	0.373	-	-
C2.	5.23	10.71	0.373	18.9	NTM
X.1	10.1	14.0	1.29	-	-
X.2	10.1	14.0	1.29	28.0	ETM

Table 4.8: Load cases used in time-domain simulations

Chapter 5

Method

5.1 Coordinate System

The definition of the coordinate system and the mooring line numbers used in the analyses are shown in Figure 5.1.

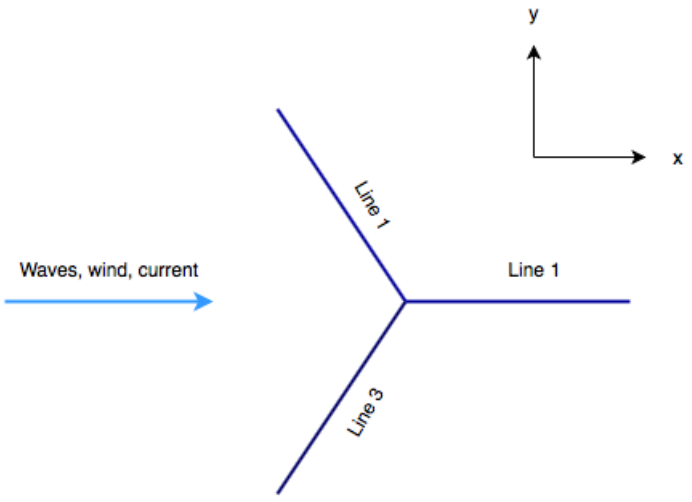

Figure 5.1: Definition of coordinate system

5.2 Simulation Tools

5.2.1 GeniE

The DNV GL software GeniE is a part of the Sesam package and is a structural design analysis tool [33]. The software may be utilized for modeling both bottom-fixed and floating structures by combined beam, plate, and shell modeling. Finite element mesh generation and analysis, and environmental load calculation are some of the analyses that can be carried out with GeniE.

In this thesis, GeniE was used to make a panel model of the substructure of the floating wind turbine. The model was discretized into panels and imported into HydroD, where hydrodynamic loads were calculated by a panel method.

5.2.2 HydroD

HydroD is a software used to compute hydrostatics and stability, wave loads, and motion response for ships and offshore structures [34]. The application provides two features named Wadam and Wasim. Wadam is used to calculate wave loads with Morison's equation and first and second-order 3D potential theory in the frequency domain. Wasim also uses Morison's but can solve 3D diffraction/radiation problem by a Rankine panel method where incident wave potentials are defined by Airy linear or stokes wave theory of fifth order. For Wasim, is it possible to perform analyses in both the frequency- and the time-domain.

In this project, the Wadam code was used to perform a frequency domain analysis of the semi-submersible. This code uses a panel method based on potential theory to calculate the frequency dependent added mass and radiation damping, force and motion transfer functions, restoring, mass, and retardation functions. The theory behind this is presented in Section 3.2.1. The hydrodynamic properties obtained from the frequency domain analyses were written out to a G.SIF-file which was implemented into SIMA.

5.2.3 SIMA

SIMA is a software used for time-domain coupled analyses combining hydrodynamic and aerodynamic theory, applying functions of the control system and calculating structural response [6]. The features of SIMO and RIFLEX are used in the analyses for floating wind turbines. RIFLEX is a tool developed to analyze slender structures such as risers and mooring systems by a non-linear finite element formulation and can carry

out coupled time-domain analysis on rigid bodies. Aerodynamic forces are calculated in RIFLEX with the blade element/momentum (BEM) theory explained in section 3.4.1. SIMO, on the other hand, is used to model the hydrodynamic loads acting on the body. A user-defined wave-environment can be defined, and SIMO applies a dynamic wave generation. The theory behind the coupled analysis and the equation of motion of the coupled model is presented in Section 3.5.

5.3 Wind Turbine Model

The wind turbine concept used in this project consists of the platform OO Star 10 MW Wind Floater designed by Dr. Tech Olav Olsen AS and the DTU 10 MW Reference Wind Turbine. The concept is a part of the Lifes50+ research project which is funded by the European Union [35]. The goal of this project is to develop a cost-effective substructure design which can be used for a 10 MW wind turbine at water depths from 50-200 m. Four different concepts participated in the first phase of the project, which consisted of conceptual design and upscaling from 5 to 10 MW of the design. Two of these were selected to the next phase, which consisted of numerical and experimental investigation and the OO Star 10 MW Wind Floater is one of these concepts. The outcome of the project has been to develop and publish guidance and recommended practices for designing and analyzing substructures for floating wind turbines.

5.3.1 DTU Wind Turbine

The wind turbine used as the reference turbine for the OO Star 10 MW Wind Floater in the Lifes50+ project is the DTU 10 MW Reference Wind Turbine. This turbine is developed from a cooperation between the Danish research center, DTU Wind Energy and Vestas [5]. The most relevant parameters of the wind turbine for this project are presented in Table 5.1.

Parameters	Unit	Value
Cut in wind speed	$m/$	4
Cut out wind speed	m/s	25
Rated wind speed	m/s	11.4
Rated power	MW	10
Number of blades	-	3
Rotor diameter	m	178.3
Hub height	m	119
Minimum rotor speed	rpm	6
Maximum rotor speed	rpm	9
Rotor mass	t	227.96
Nacelle mass	t	446.04
Tower mass	t	628.44

Table 5.1: Parameters of DTU 10 MW Reference Wind Turbine

5.3.2 OO Star Wind Floater Semi

The OO Star 10 MW Wind Floater platform is designed by Dr. Tech Olav Olsen AS and is a semi-submersible platform consisting of four columns, one in the center where the tower and the wind turbine will be placed, and three outer columns connected with pontoons with 120 degrees between [7]. Below the outer columns and pontoons, thin, flat plates called heave plates. These are implemented to increase the natural period in heave and thus decrease the heave motion of the platform. The material used to construct the platform is post-tensioned concrete. The properties of the semi are presented in Table 5.2 and the dimensions can be seen in Figure 5.2.

Property	Unit	Value
Total substructure mass	kg	2.1709e+07
Tower base	m	11
Draft	m	22
Center of buoyancy	m	-14.236
Angle between pontoons	deg	120

Table 5.2: Properties of OO Star 10 MW Wind Floater Semi [7]

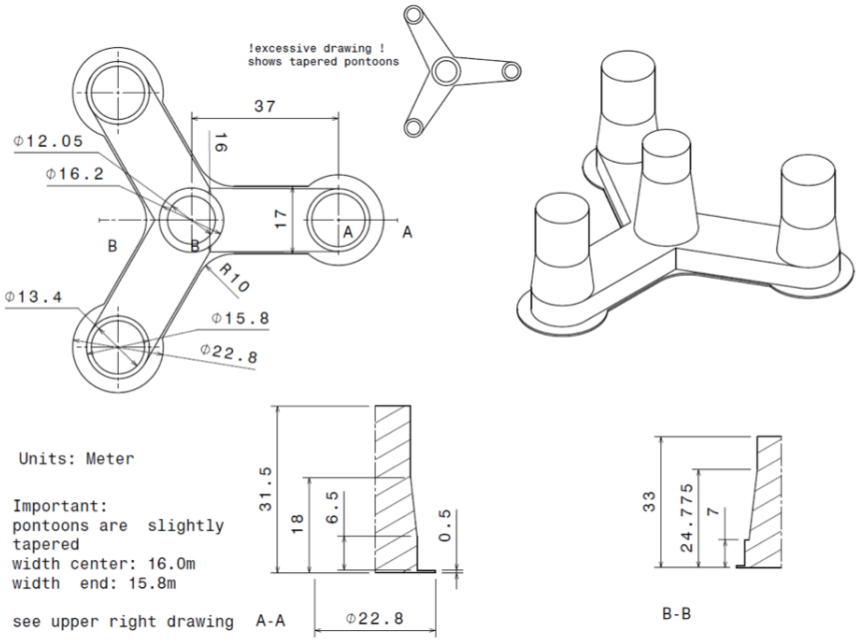

Figure 5.2: Structural drawing of OO Star 10 MW Wind Floater Semi [5]

5.4 Design of Mooring System

There are several challenges related to designing mooring systems at shallower water depths (50-100 m). The part of the mooring line which is suspended is shorter than in deeper waters. For a chain catenary system, the weight of the suspended line is what is causing the restoring of the horizontal motions of the platform [2]. This means that for a shorter line, less horizontal tension is required to create horizontal offsets. Another case at shallower water is that the mooring line tension as a function of the horizontal offset becomes non-linear for a smaller offset than at larger water depths [36]. If the wind turbine is subjected to extreme weather that causes large offsets, the mooring line tension may become very large and exceed the mooring line breaking strength. It is important that the mooring system is designed so that the natural periods in surge, sway and heave are larger than the wave frequencies. At the same time, it is important that the system is stiff enough to avoid large offsets, which can cause damage to the power cable.

Mooring lines designed for shallower water depths are usually designed with heavier material than for a similar mooring system at deeper water and often are clump weights added to increase the weight. This gives a higher pretension, and a larger horizontal force is required to move the platform in the horizontal directions.

The mooring system originally designed to the OO Star 10 MW Wind Floater is developed for 130 m water depth. Thus, this mooring system was not applicable for a 50 m water depth. Instead, the mooring system used in the analysis was taken from the Master thesis with the title *Mooring System Design for a Large Floating Wind Turbine in Shallow Water* written by Tiril Stenlund during the spring of 2018 [8]. This system was initially designed to a water depth of 70 m, but the distance from the fairlead to the sea bottom was only 55 m. This made it possible to apply to the OO Star Wind Floater at 50 m water depth where the vertical distance from the fairlead to the sea bottom was 59.5 m. Table 5.3 gives the properties of the mooring system used in this thesis. Since the focus of this thesis was not on the design of the mooring system, the effect of adding clump weights or using different materials was not looked into.

A static analysis was performed with MATLAB to fit the mooring system to the water depth of 50 m with a horizontal distance from the fairlead of 59.5 m. This is explained in detail in Section 5.4.1. Figure 5.3 shows the side view of the mooring line configuration for the mooring line used in this thesis.

Property	Unit	Value
Distance from Fairlead to seabottom	m	59.5
Material	-	Studless R4
Density	kg/m^3	7850
Number of mooring lines	-	3
Angle between adjacent mooring line	$^\circ$	120
Length of mooring line	m	845
Mass of each line in air	kg/m	462
Mass of each line in water	kg/m	401
Elastic stiffness, EA	kN	3.7789e+06
Maximum breaking strength	kN	20156

Table 5.3: Properties of mooring system [8]

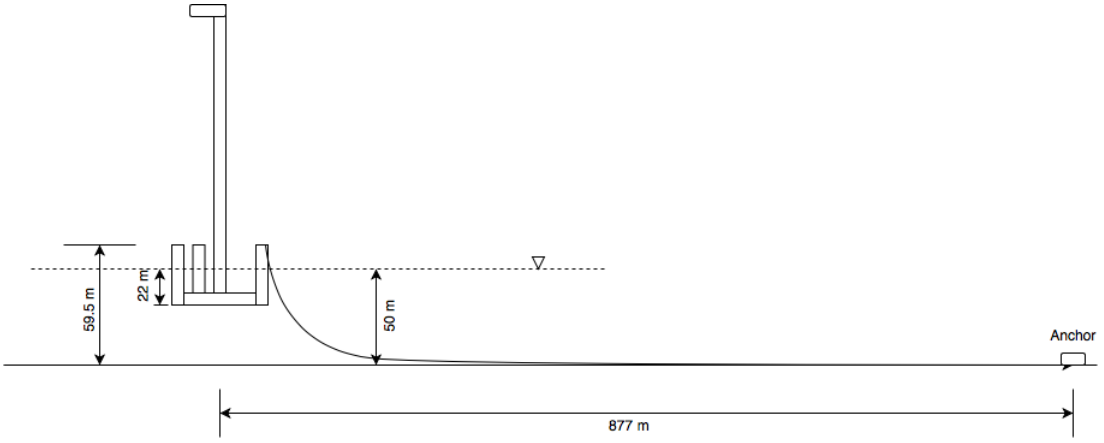

Figure 5.3: Moring line configuration

5.4.1 Static Analysis

A static analysis of the mooring system was performed with MATLAB. This was done by using the catenary equations presented in Chapter 3.6. A pretension of 1457 kN was used in accordance with the pretension from [8]. The weight per meter,w, total length, l, and vertical distance, h, from fairlead to seabed were known parameters in the static analysis and were taken from Table 5.3. The MATLAB-script made to perform the static analysis calculated the following parameters for when the platform is in equilibrium:

- Length of the suspended mooring line length, l_S
- Total weight of suspended mooring lines
- Horizontal distance from fairlead to anchor, X
- Coordinates of anchor positions
- Horizontal offset from equilibrium position for different values of T_H

The resulting values obtained from the analysis are presented in Table 5.4. The total length of the mooring line is 845 m, while the length of the suspended line is only 220 m. This is expected since the restoring effect the mooring lines give to the platform is because of the weight of the suspended line. Since this part of the line is shorter than for mooring lines in deeper water, it provides less restoring and thus needs a larger part of the mooring line to lay on the sea bottom to prevent it from being lifted completely. This has to be prevented since the anchors cannot take on any vertical loads.

Parameter	Unit	Value
Length of suspended line, l_s	m	220.9
Total weight of mooring 3 lines	t	266
Horizontal distance from fairlead, X	m	834

Table 5.4: Properties of mooring system obtained from static analysis

The coordinates of the three anchors obtained from the static analysis are presented in Table 5.5. The values calculated for the anchor coordinates with MATLAB were verified by performing a static analysis with SIMO. This gave almost the same result with a maximum difference of 0.3 m.

The horizontal tension T_H increases for increasing loads acting on the platform. It is important to ensure that this tension does not exceed the breaking strength of the mooring line for large offsets. The value of X was calculated for a range of tensions from the pretension to the breaking strength. To find the horizontal offset from the

	x $[m]$	y $[m]$	z $[m]$
Anchor 1	877.47	0	-50
Anchor 2	-438.93	-760.25	-50
Anchor 3	-438.93	760.25	-50

Table 5.5: Coordinates of anchors

equilibrium position, the initial horizontal distance X_0 was subtracted from all the X obtained with different tensions. Figure 5.4 shows the horizontal tension as a function of the horizontal offset of the platform. The mooring line tension becomes non-linear only after an offset of 4 m and increases rapidly. At an offset of 8 m, the maximum breaking strength is already exceeded.

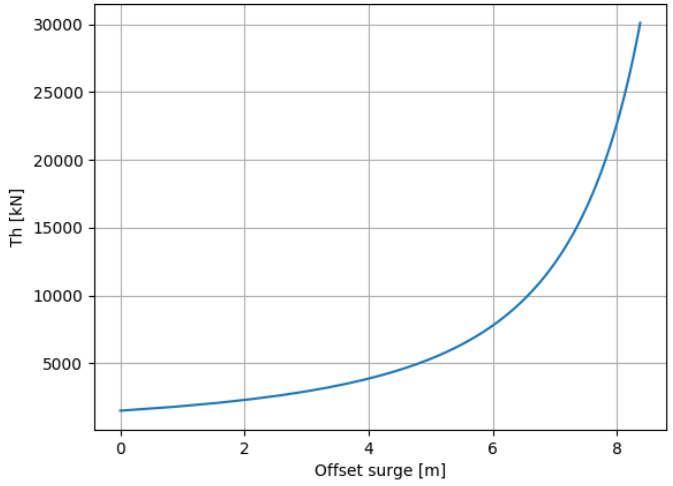

Figure 5.4: Horizontal tension for offset in surge

Even though the mooring lines reach the breaking strength at an offset of 8 m, the mooring system was considered good enough for this project since the focus was not on the design of the mooring system.

5.5 First-Order Frequency Domain Analysis

To study the behavior of the floating wind turbine by considering potential theory, a frequency domain analysis had to be carried out to obtain the hydrodynamic characteristics of the body. This was done with Wadam, which uses a panel method to calculate

the hydrodynamic properties. These properties consisted of:

- Frequency dependent added mass and damping, and the corresponding retardation functions
- Stiffness matrix
- Mass matrix
- Linear damping
- First-order motion and force transfer functions

The panel method requires a panel model of the body. This model was created with GeniE and imported into HydroD. The following sections provide a comprehensive description of how the frequency domain analysis was carried out.

5.5.1 Panel Model

A panel model of the OO Star 10 MW Wind Floater Semi was created as a part of the project thesis in the fall of 2018 [1]. The dimensions of the body were taken from the structural drawings presented in Figure 5.2. The model was made by shell elements, and no structural properties were added. The model was then discretized into small panels. The linear frequency domain analysis only considers the part of the structure which is defined below the free surface. However, the part of the body above the water surface was also included to be able to perform a second-order frequency domain analysis at a later stage. Feature-edges were defined at the free surface so that no panels would cross the free surface. Settings in Wadam made it possible only to create a model of half of the body, and apply symmetry about the xz-axis. The panel model is seen in Figure 5.5. A sensitivity study of the panel size was carried out to find out how large the panel size could be without affecting the results. The results from this sensitivity study are presented in the project thesis [1]. The resulting panel size used was 0.85 $m/element$.

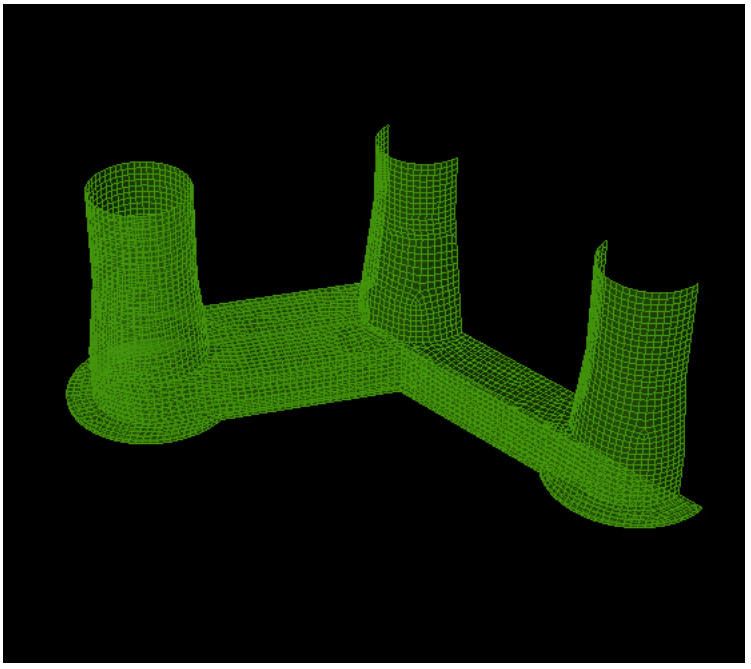

(a) GeniE

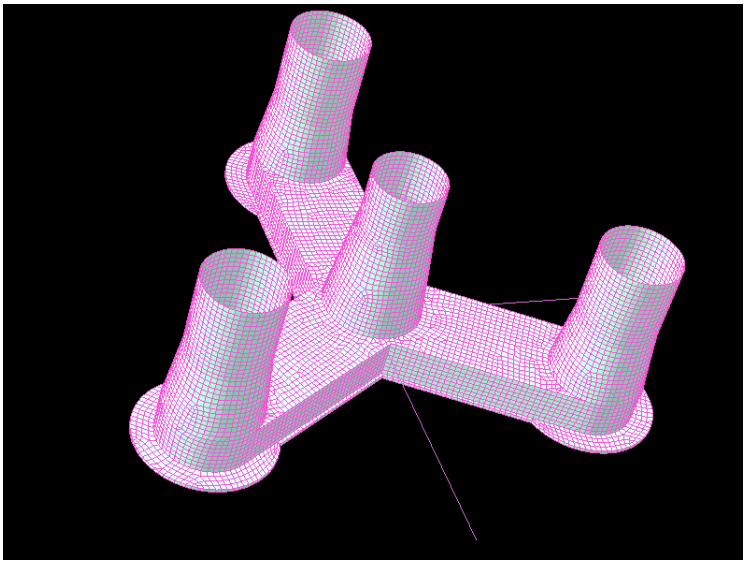

(b) HydroD

Figure 5.5: Panel model

5.5.2 Frequency Domain

The panel model was imported into HydroD, where a panel method was used to perform the frequency domain analysis. A set of 36 wave-frequencies from 0-5 rad/s and 11 directions from 0-360 degrees, were defined. The output of HydroD containing all the information about the hydrodynamic properties of the body was a G.SIF-file which was imported into SIMA. A MATLAB-script provided by co-supervisor Erin Bachynski was used to present the results graphically.

To verify the model and the results obtained, the frequency dependent added mass were compared with the added mass and damping of the OO Star Wind Floater defined in the technical report of Lifes50+ [11]. Figure 5.6 shows the frequency dependent added mass and damping obtained. The blue crosses define the added mass and damping from the Lifes50+ report. The data set of the frequency dependent added mass and damping obtained from Lifes50+ was not publicly available, hence a few points on the added mass and damping graphs from [11] were found and plotted in Figure 5.6. The frequency domain analysis show good agreement with the values from Lifes50+.

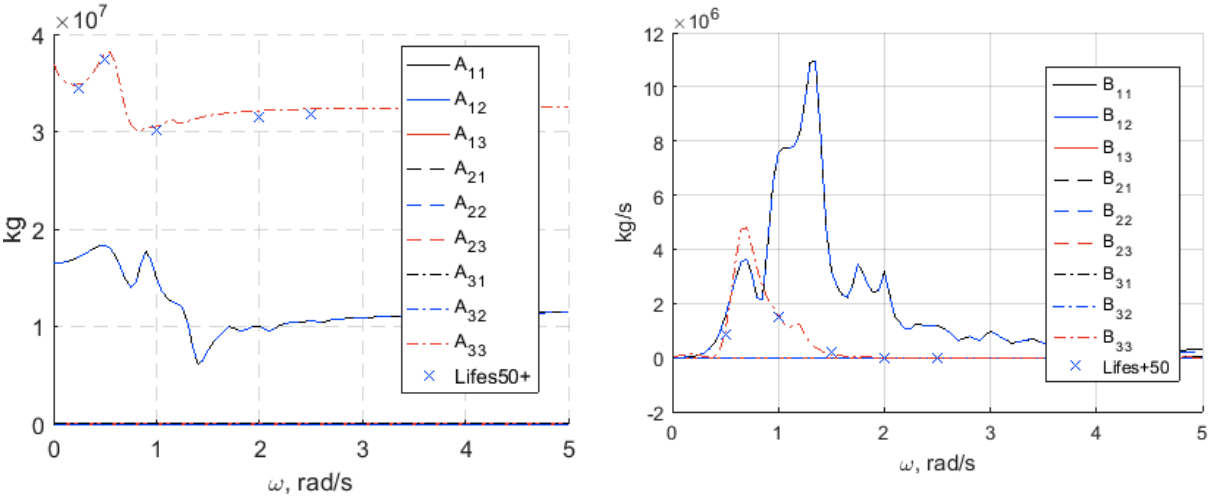

(a) Added mass

(b) Radiation damping

Figure 5.6: Comparison of added mass and damping from Lifes+50 and GeniE [1]

5.6 Second-Order Frequency Domain Analysis

From the literature survey, it was found that second-order effects are important to consider when a structure is moored. To account for second-order slow-drift motions, it was necessary to obtain the QTFs of the floating body. Two methods were used to find the QTFs. Pressure integration of the body, which consider the contributions from all difference-frequencies. For this method, the second-order velocity potential is needed, and a panel model of the free surface is necessary[2]. The other method is Newman's approximation, which obtains the transfer function by only considering the mean drift forces, and the second-order velocity potential is not used. Both methods were applied in the second-order frequency domain analysis, and the outputs of the analysis, which was later implemented into SIMA were:

- Wave-drift force
- Difference-frequency wave force transfer functions (QTF)

5.6.1 Second-Order Free Surface

To be able to carry out a second-order potential theory analysis, it was necessary to create a panel model of the free surface. This was necessary for the sum and difference-frequency calculation in Wadam since the second-order velocity potential is needed to obtain these terms [37]. However, only the effects from the difference-frequencies were taken into account since the sum-frequencies do not have much effect on a moored structure. The free surface was modeled in GeniE such as the model of the platform. A hydro-pressure with normal component in the negative z-direction was added to the model, and it was discretized into small panels.

Several constraints had to be taken into account during the modeling of the free surface to be able to import the model into HydroD. The maximum number of elements on the free surface was 10000, and no triangular elements were allowed. The latter constraint was difficult to avoid due to the mesh-settings in GeniE and trying to eliminate the remaining triangular elements was extremely time-consuming. This made it very difficult to perform a systematic sensitivity study of the mesh configuration and the mesh sizes, since, for every change made, new triangular elements appeared.

According to the Wadam Manual [37], the radius of the free surface should be at least 50% of the water depth. However, since the water depth studied was 50 m, the factor deciding the radius was instead the wavelength of the incoming waves. From the environmental conditions, it was seen that during normal operational conditions, the peak period of the wave condition was $T_p = 7.25\ s$. The corresponding wavelength to a

wave with a 7.25 s period is approximately 100 m. However, to be able to study waves for more extreme conditions, the radius was set to 200 m. Figure 5.7 and Figure 5.8 show the final panel model of the free surface with 4524 panels.

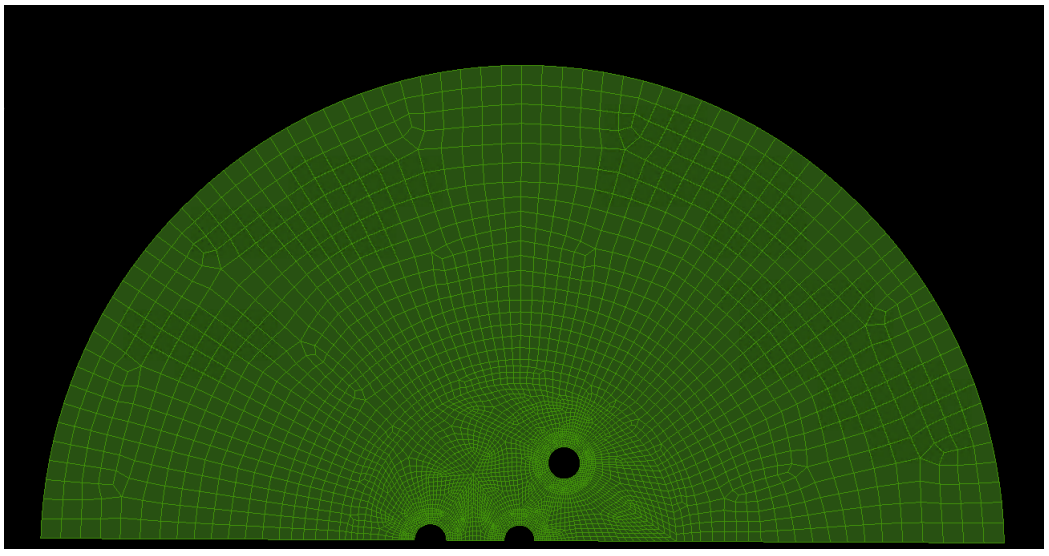

Figure 5.7: Panel model of free surface in GeniE

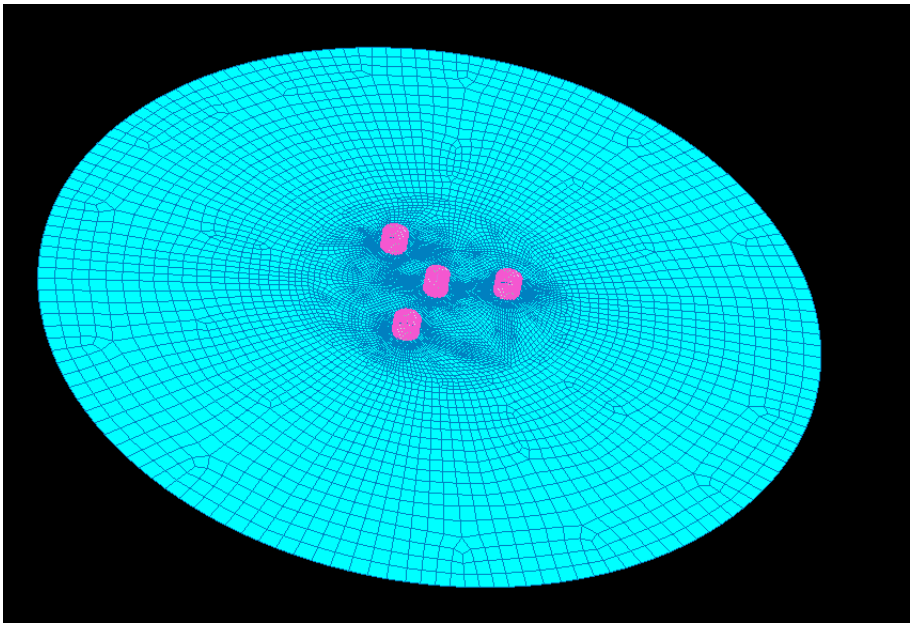

Figure 5.8: Free surface and platform in HydroD

When making the mesh configuration, the focus was made on keeping the panel sizes closest to the platform small, while increasing the panels further out. The panels closest to the platform had the same panel size as the platform of 0.85 $m/element$. The complex geometry of the body caused difficulties regarding creating a satisfying mesh configuration. The challenging geometry and the restraint of not having any triangular elements, made a systematic sensitivity study extremely time-consuming and was not prioritized.

The lack of the sensitivity study of the panel size and the panel configuration is a significant source of error and may have affected the results.

5.6.2 Second-Order Frequency Domain

A new frequency domain was chosen for the second-order frequency domain analysis. A second-order analysis is significantly more time-consuming than a first-order analysis, so the number of frequencies had to be reduced. Also, only one direction(0 degrees) was considered.

The frequencies were chosen based on the wave period range, which is defined from approximately 5-20 s. At the same time, the natural frequencies of the semi were considered, and difference-frequencies corresponding to these was included by selecting a frequency-step between two frequencies corresponding to some of the natural frequencies. However, this was only done for a few frequencies due to the computational capacity. Frequencies from 0.5 rad/s to 1.4 rad/s were chosen. This corresponds to a range of wave periods from 4.5 s to 12.6 s. The frequency-step between each frequency was normally set to 0.05 rad/s, but between some frequencies, it was set to 0.03 rad/s so that some difference-frequencies would coincide with the natural frequency in surge of 0.08 rad/s.

Several ranges of frequencies were tried out. The goal was to include frequencies corresponding to the whole wave range, but due to computational problems, frequencies lower than 0.5 rad/s were not included.

The difference between a coarse and fine frequency domain was investigated. Figure 5.9 shows the QTFs in surge, heave and pitch obtained with a coarse and fine frequency domain. The fine frequency domain included 23 frequencies, while the coarse included 15 frequencies. The graphs show that in surge, the coarse frequency domain gave the same results as the fine. In heave and pitch, the coarse frequency domain underestimated forces between 0.6 rad/s and 0.8 rad/s. From the QTFs, it is observed that at frequencies above 1.2 rad/s, something went wrong in the analyses. However, frequencies above 1.2 rad/s correspond to small waves, and it was therefore decided

to continue with the results from the fine frequency domain analysis. Computational issues were a significant obstacle when carrying out the second-order frequency domain analyses, and a larger frequency domain was not possible to achieve. This is a possible source of error in the results regarding second-order effects.

After finalizing the second-order frequency domain analysis, the QTFs and the mean wave drift obtained from the frequency domain analysis, were imported into SIMA.

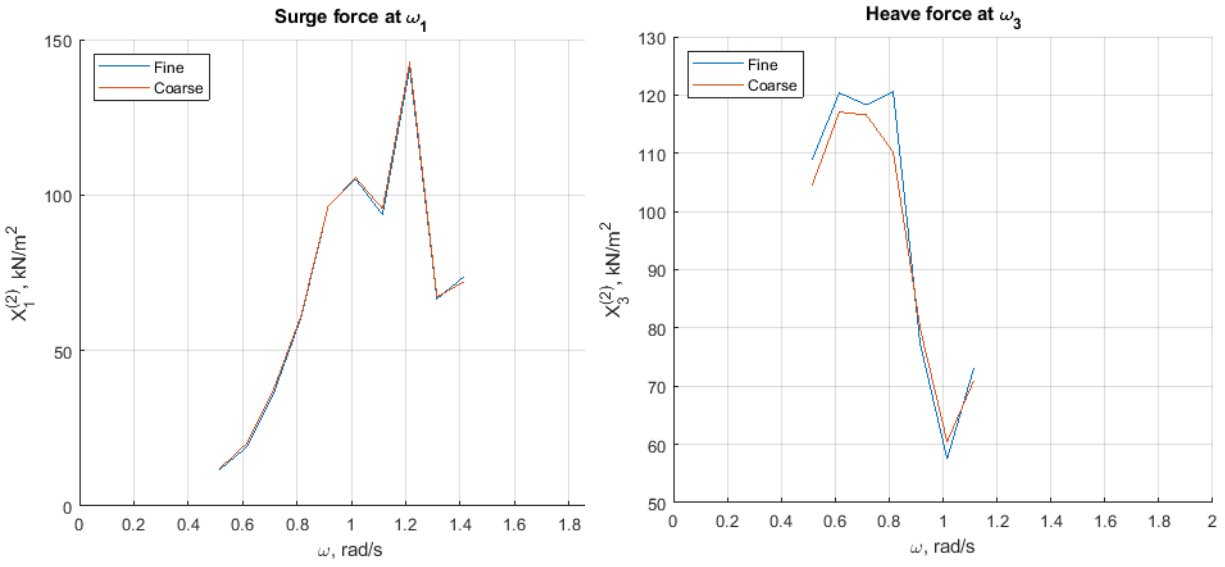

(a) Surge

(b) Heave

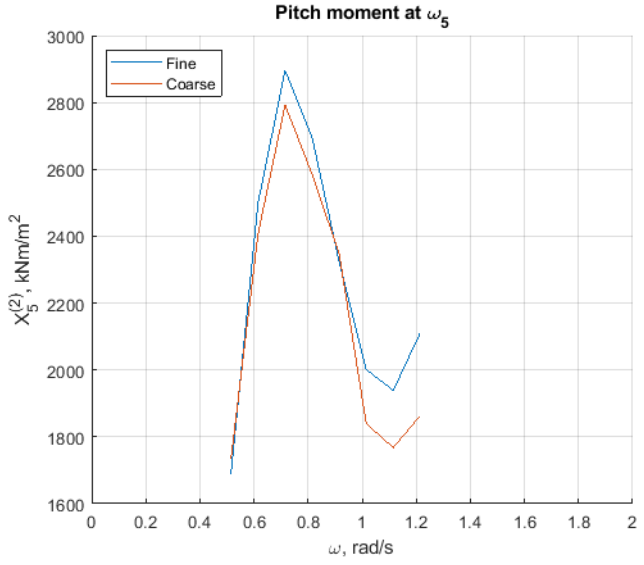

(c) Pitch

Figure 5.9: QTFs for coarse and fine frequency domain in surge, heave and pitch

5.7 Load Calculation with Strip Theory

Another way of calculating wave loads from potential theory on a floating structure is by application of strip theory. For slender cylindrical elements, this is calculated by using the Froude-Krylov and added mass term of Morison's equation. This is also possible to do with a semi-submersible structure which is composed of cylindrical elements [2]. This section provides the methodology followed to use strip theory to calculate the wave loads on a semi-submersible supporting a wind turbine. Several studies regarding the application of strip theory on a semi-submersible have been carried out as written in Section 2.3, but few studies are performed on the use of strip theory on a floating wind turbine in small water depths.

When applying strip theory to find the added mass term, long wave approximation is required to be able to discount the damping, as explained in Chapter 3.3. The force and motion transfer functions and retardation functions of added mass and damping were removed from the coupled model created in SIMA, and the frequency dependent added mass and damping were set to zero. Slender elements were created by defining the x-,y- and z-coordinates of the two endpoints of the cylinder, and the total volume of each cylinder was defined. Only circular cross-sections were allowed, so the cones and pontoons were modeled as cylinders, but with the same volume as the original configuration. Figure 5.10 shows the slender elements that the semi-submersible was divided into in SIMA.

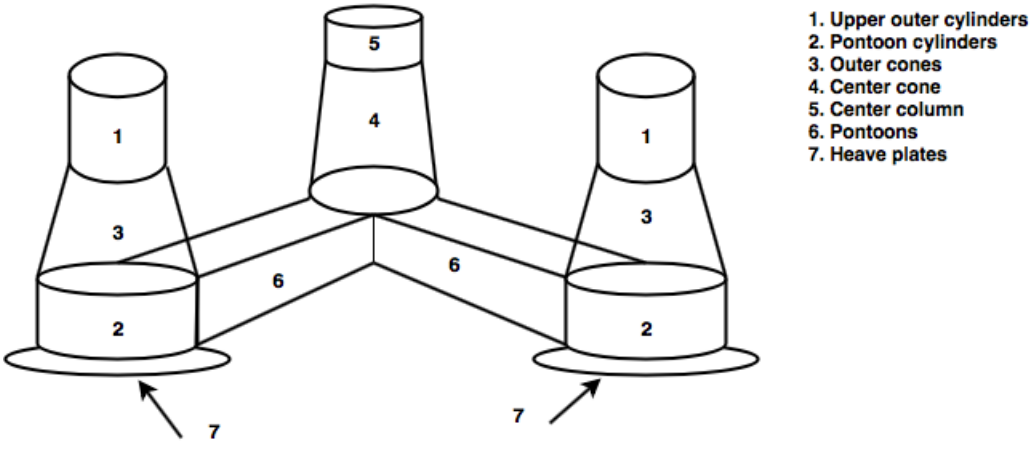

Figure 5.10: Platform divided into slender elements

The slender elements were then divided into a user-defined number of strips. The Froude-Krylov force was calculated automatically with SIMA by the integration of

the volume over the length of the elements multiplied by the acceleration of the fluid particles [23]. However, the added mass term had to be calculated and added manually to the slender elements. Table 5.6 shows the dimensions of each slender element. The diameters of the cones in SIMA were defined as the average of the top and bottom diameter, and the diameter of the pontoons as the height.

	n Elements	Diameter$_1$ $[m]$	Diameter$_2$ $[m]$	Length $[m]$	L/D
Upper outer cylinders	3	13.4	13.4	13.5	1.007
Pontoon cylinders	3	15.8	15.8	6.5	0.411
Outer cones	3	13.4	15.8	11.5	0.727
Center cone	1	12.05	16.2	17.775	0.683
Center column	1	12.05	12.05	8.225	0.683
Pontoons	3	15.8	15.8	37	5.285
Heave plates	3	22.8	22.8	1	0.044

Table 5.6: Dimensions of slender elements defined in SIMA

5.7.1 Added Mass Calculation

Added mass in kg/m had to be added manually to each of the slender elements. Since strip theory was used, the two-dimensional added mass from potential theory was calculated. As presented in Section 3.3, the added mass from potential theory can be calculated from Equation 5.1.

$$A_{jk} = C_a \rho \frac{\pi D^2}{4} \tag{5.1}$$

The two-dimensional added mass coefficients C_a for different cross-sections are defined by DNV GL in [38]. For circular cross-sections, $C_a = 1.0$. For rectangular cross-sections, the coefficient depends on the width/height ratio of the cross-section and for a rectangle with a width/height ratio of 2.3, C_a was approximated to 1.36. The added mass of the slender elements had to be defined in the local element coordinate system. The local element axes were defined as presented in Figure 5.11.

This means that for the columns, added mass in heave is defined in the x-direction and added mass in surge and sway in the y- and z-direction. The added mass for each slender element was calculated with a MATLAB script and applied in SIMA. The added mass values are defined in Table 5.7. Regarding the cones, the added mass was taken as the average of a strip with the top diameter and a strip with the bottom

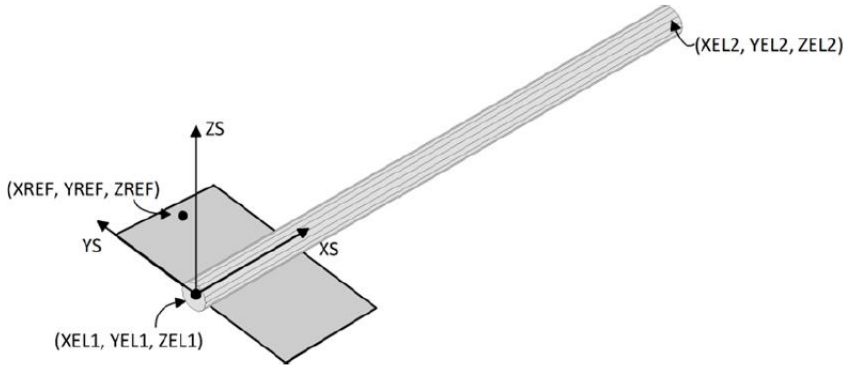

Figure 5.11: Local coordinate system of slender elements [6]

Added mass	A_x $[kg]$	A_y $[kg]$	A_z $[kg]$
Upper outer cylinders		1.4455e+05	1.4455e+05
Pontoon cylinder		1.0048e+05	1.0048e+05
Outer cones		1.716e+05	1.716e+05
Center cone		1.606e+05	1.606e+05
Center column			
Pontoons	2.733e+05		2.733e+05
Heave plates	4.049e+06		

Table 5.7: Added mass in each direction for all of the slender elements

diameter. The calculation of the added mass of the heave plates was more complicated and is discussed in the section below.

The contribution to added mass in surge from the heave plates was assumed to be very small and was not added to the slender elements. It was also assumed that all contribution to added mass in heave came from the heave plates and the plates below the pontoons. The center column is above the mean surface level, and the added mass was therefore not calculated for this element.

5.7.2 Added Mass of Heave Plates

The added mass of the heave plates was calculated based on equations taken from [39]. This article provided equations for added mass for a disk with and without a cylinder, and these equations are presented below.

$$A_{33,disk} = \frac{1}{3}\rho D_d^3 \tag{5.2}$$

$$A_{33,disk\ w/cylinder} = \frac{1}{12}(2D_d^3 + 3\pi D_d^2 z - \pi^3 z^3 - 3\pi D_c^2 z) \tag{5.3}$$

where

$$z = \frac{1}{\pi}\sqrt{D_d^2 - D_c^2} \tag{5.4}$$

The diameter of the disk, D_d, was 22.8 m, while the diameter of the cylinder, D_c was 15.8 m. The values of the added mass in heave obtained when inserting the diameters in Equation 5.2 and 5.3 are presented in Table 5.8.

	A_{33} $[kg]$
Disk	4.050e+06
Disk w/cylinder	3.634e+06

Table 5.8: A_{33} for a disk and a disk with a cylinder

These theoretical values were compared to the actual added mass contribution of the heave plates. This was done by removing the heave plates from the panel model and performing a frequency-domain analysis on the panel model without heave plates. The panel size was kept the same for the model with and without the heave plates. Figure 5.12 shows the frequency dependent added mass in heave calculated from potential theory for the platform with and without heave plates. It can be seen that the heave plates are important to the contribution of the added mass.

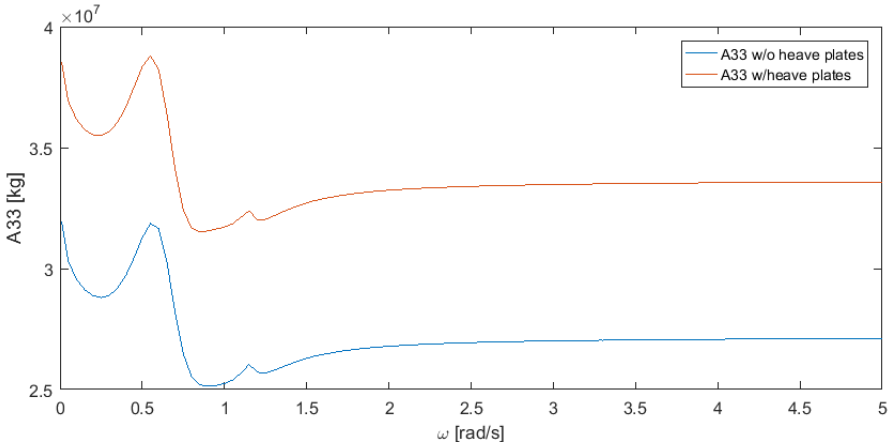

Figure 5.12: Added mass in heave

Since long wave approximation is used when Morison's equation and strip theory is applied in this thesis, the value of the added mass in heave for the two models is compared at the zero frequency. The two first columns of Table 5.9 shows the total added mass at zero frequency calculated with Wadam with and without heave plates,

and the last column shows the contribution of one heave plate to the added mass. The latter value was calculated by subtracting the added mass calculated without heave plates from the added mass calculated with heave plates. Since there were three heave plates, this number was divided by three.

	w/Heave plates $[kg]$	w/o Heave plates $[kg]$	Heave plate $[kg]$
$A_{33,0}$	3.6852e+07	3.1927e+07	1.641e+06

Table 5.9: Difference in added mass for structure with and without heave plates

The contribution of one heave plate calculated from Wadam is significantly less than the added mass calculated theoretically presented in Table 5.8. This implies that the rest of the platform also has a significant contribution to the added mass in heave. However, in SIMA, the added mass in heave was applied so that almost all added mass in heave came from the heave plates and the plates below the pontoons. Thus, the value of the added mass of the disk without cylinder, calculated from Equation 5.2, was used to calculate the added mass of the heave plates which was applied to the slender element modeled as the heave plate.

To calculate the added mass contribution from the plates below the pontoons, Equation 5.1 was used and the width of the plates, 17 m, was applied as the diameter. The total value of the added mass calculated manually in heave and surge is compared with the total values obtained from the frequency domain analysis in the section below.

5.7.3 Comparison of Calculated Added Mass with Added Mass from Frequency Domain Analysis

The total added mass calculated with strip theory and from frequency domain analysis, in the horizontal and vertical direction, are presented and compared in Table 5.10. For strip theory, values were found by multiplying the added mass values presented in Table 5.7 by the length of the element and adding up the contribution from each element in surge and heave separately. For the cones, the added mass was integrated with respect to the height of the cones since the diameter was not constant. The added mass from frequency domain analysis was taken for the zero frequency since long wave approximation was assumed for the added mass calculated by strip theory.

There are several reasons for the differences in the added mass calculated by strip theory and the added mass obtained from the frequency domain analysis. The added mass coefficient was assumed to be 1 for the circular cross-sections and 1.36 for rectangular cross-sections. From [2], it is known that C_a is frequency dependent, and this was not

	$A_{jk,Strip}\ [kg]$	$A_{jk,0,Frequency\ Domain}[kg]$	Difference
Horizontal	1.5612e+07	1.6475e+07	5.2%
Vertical	3.9771e+07	3.6852e+07	7.9%

Table 5.10: Difference in added mass between calculated value and value from frequency domain analysis

taken into considerations. The junctions between the columns and the pontoons were not adjusted.

5.7.4 Discussion of Method

The method described above of how to apply strip theory to a semi-submersible platform is a simplified method to calculate the wave loads compared to performing a full frequency domain analysis. However, it is necessary to discuss if the method is valid or not.

Commonly, Morison's equation can be applied when the wavelength-to-diameter ratio, λ/D, is larger than 5. The wave periods are found between 5-21 s, and a period of 5 s corresponds to a wavelength of 39 m. This does not meet the requirement of $\lambda/D > 5$, and diffraction forces are considered important, and the long-wave approximation is no longer valid.

The added mass coefficients C_a are taken to be 1.0 for all cylindrical elements. These coefficients are dependent on the frequency and the KC number [2]. This is an error source on the added mass terms calculated with strip theory. The effect of the junction between the elements on the added mass is not investigated. This could have been done by performing a frequency domain analysis on each of the elements separately and comparing the added mass values for the sum of the added mass from each element with the added mass obtained for the total platform.

5.8 Coupled Analysis

The behavior of the floating wind turbine was analyzed by studying the results of several coupled time-domain simulations with the different load cases. These simulations were carried out with SIMA. The following sections present different topics regarding the coupled model and analyses.

5.8.1 Coupled Models

Four different coupled models were created to study the effect different hydrodynamic load models had on the results. All models included a RIFLEX model of the DTU 10 MW wind turbine and the mooring system defined in 5.4. The hydrodynamic properties obtained with Wadam were imported into a SIMO-body, modeled as a nodal element. The four different models made were:

Linear Frequency Domain Analysis Model (LDFA):
No adjustments were made to the description above for this model. second-order effects were not accounted for.

LFDA-model including a full QTF:
This model was identical to the LFDA-model, but the difference-frequency wave force transfer function was added to the SIMO-body.

LFDA-model including wave-drift:
This model was identical to the LFDA-model, but the mean wave-drift obtained from the second-order frequency domain analysis was added to the SIMO-body. This model calculated wave loads by Newman's approximation.

Strip Theory Model:
The same model was used, except that the hydrodynamic properties of the SIMO-body were removed. Added mass coefficients were added to the slender elements, as explained in chapter 5.7.

5.8.2 Mooring System

The mooring system was defined by adding a node at the fairlead positions and the anchor positions. A cross-section with the properties given in Table 5.3 was defined, and a line composed of this cross-section was created between a fairlead and an anchor. A static analysis was carried out with SIMA, and the results agreed well with the static

analysis performed with MATLAB described in Section 5.4.1. Figure 5.13 shows the mooring line configuration in SIMA after a static analysis.

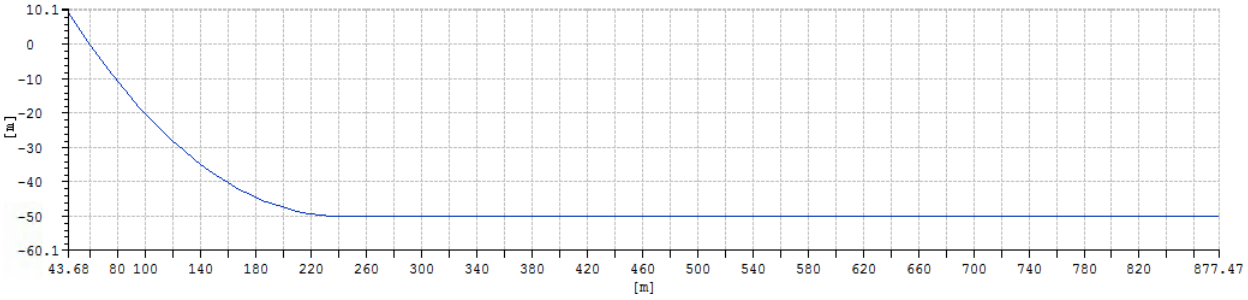

Figure 5.13: Mooring line configuration in the xz-plane after static analysis in SIMA

5.8.3 Viscous Drag Elements

As explained in Section 3.3, viscous damping terms are important to include, to better describe the behavior of the body when it experiences resonant motions. This was done by adding the drag coefficient from Morison's equation to the different parts of the body.

The coupled models were divided into slender elements as described in Section 5.7 and viscous drag coefficients were added to account for viscous damping. The drag coefficients were added in the local element axis. To model the effect of the heave plates at the bottom, the bottom of the vertical outer columns were modeled with a large drag coefficient corresponding to the drag coefficients the plates would have had with the real diameter. The drag coefficient and diameter for each cylindrical element were defined in the Lifes50+ report [11], and the equation for calculating the quadratic drag is presented in Equation 5.5. An error source regarding the drag coefficients is that the counter interaction between the slender member and the dependency on the KC-number were not taken into account.

$$Q_D = \frac{1}{2}\rho C_D D \tag{5.5}$$

Table 5.11 shows the values used to calculate the quadratic drag and the quadratic drag for each element.

Figure 5.14 shows the RAO of the heave motion with and without viscous damping. The amplitude of the heave motion was reduced drastically when viscous damping terms were introduced. At wave periods far from the natural period in heave, the viscous damping does not affect the response.

Part of Semi	D $[m]$	$C_D[m]$	$Q_D[Ns^2/m^3]$
Upper central column	12.05	0.729	4502
Lower central column	14.125	0.7165	5186.8
Upper outer column	13.4	0.72	4944.6
Lower outer column	14.6	0.713	1294.5
Cylindrical part of pontoon	15.8	0.706	5716.8
Rectangular part of pontoon	7	2.05	7354.4
Outer heave plates	15.8	38.34	155229.1
Central heave plate	14.125	14.99	59528.9

Table 5.11: Diameter and drag coefficient of modified slender elements

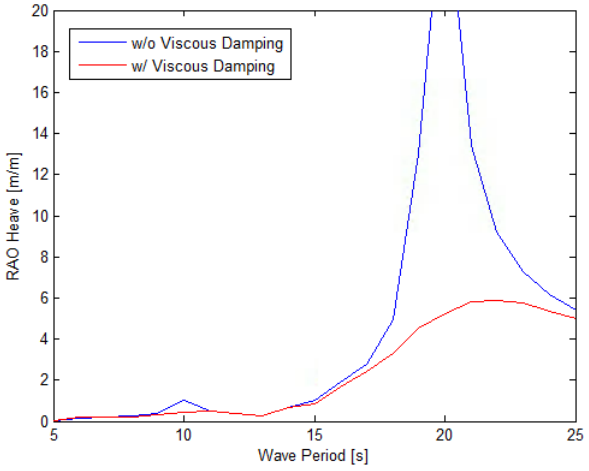

Figure 5.14: RAO of heave motion with and without viscous damping

5.8.4 Corrections of Control System

A wind turbine works most efficient at the rated wind speed. At wind speeds lower than rated, the wind turbine will produce less power, and at higher wind speeds the probability of damaging the generator increases. Thus, the wind turbine is equipped with a control system that reduces power loss and the danger of damage. The control systems of the wind turbines are important, to control power production at wind speeds that are different from rated. It normally consists of two independent systems: a generator-torque controller and a variable speed-collective blade-pitch controller. The generator-torque controller tries to maximize the power output when the wind speed is lower than the rated wind speed, and the blade-pitch controller's main propose is to control the generator speed when the wind speed is higher than the rated wind speed

[40].

The control system of the DTU 10 MW reference turbine consists of these two types of controllers. The properties of these controllers were implemented into RIFLEX through an input file. When the constant wind test on the floating wind turbine was carried out, the pitch motion did not decay as it should. According to [41], this happens because the floating wind turbine experiences negative damping. The controller is made for a land-based wind turbine and is not fitted to a structure with low natural frequency in pitch. The controller reduces the thrust when the floating wind turbine is in motion by pitching the blades. It is therefore recommended by [41] to reduce the natural frequency of the controller so that this natural frequency is lower than the natural frequency in pitch.

The blade pitch controller and the generator torque controller are equipped with a proportional-integral regulator. The blade-pitch controller proportional and integral gain were taken from [42] and are expressed with Equation 5.6 and 5.7, respectively. If the natural frequency of the controller is changed, these values have to be changed correspondingly.

$$K_P = \frac{2I_{drivetrain}\Omega_0\zeta_\phi\omega_{\phi n}}{N_{Gear}\big(-\frac{\partial P}{\partial \theta}\big)} \tag{5.6}$$

$$K_I = \frac{I_{drivetrain}\Omega_0\omega_{\phi n}^2}{N_{Gear}\big(-\frac{\partial P}{\partial \theta}\big)} \tag{5.7}$$

$I_{drivetrain}$ is the drive train cast to the low-speed shaft, Ω_0 is the rotational speed of the low-speed shaft, $\omega_{\phi n}$ is the natural frequency of the controller, ζ_ϕ is the damping ratio, N_{gear} is the high-to-low speed gearbox ratio and $-\frac{\partial P}{\partial \theta}$ is the sensitivity of aerodynamic power.

Since the K_P and K_I values for $\omega = 0.06\ Hz$ are given in the input file and the other values from Equation 5.6 and 5.7 are constant, the K_P and K_I values can be found for any frequency. The natural frequency in pitch is 0.038 Hz, so the natural frequency of the pitch controller was chosen to be 0.03 Hz. The new values of K_P and K_I are given in Table 5.12

Frequency $[Hz]$	K_P	K_I
0.06	0.174828	0.015693
0.03	0.26224	0.035308

Table 5.12: New K_P and K_I values

In addition to changing the natural frequency of the controller, two more adjustments were made to make sure that the wind turbine worked as it should:

- The blade pitch angle above rated wind speed was changed by subtracting two degrees from the given blade pitch angle of each wind speed. This was done because the rotor speed decayed for increasing velocities above the rated wind speed.
- The minimum pitch angle was changed from 100 degrees to 0.001 degrees for extreme conditions.

5.8.5 Coupled Time-Domain Simulations

Six coupled time-domain simulations, corresponding to each load case, were carried out for all the coupled models described in 5.8.1. The simulation length was 4000 s with a time-step of 0.005 s. The results from these simulations are presented in Chapter 7 and 8.

Chapter 6

Verification of Numerical Model

To verify if the numerical models behaved correctly, three different tests were carried out. In addition, a comparison of mean drift force calculated with the conservation of momentum and pressure integration was conducted. Also, the numerical model made from frequency domain analysis was compared to the model based on strip theory. The different tests were:

- Decay test
- Constant wind test
- Regular wave test

6.1 Decay Tests

Decay tests were carried out in surge, heave, pitch, and yaw to find the natural period of the system. This was done in SIMA. For surge and heave, a force in the wanted DOF was applied to the wind turbine. The force was first applied as a ramp force for 50 s followed by a constant force for 100 s. The force was then released, and the wind turbine started to oscillate with its natural frequency in the given degree of freedom. Then, the same procedure was repeated in pitch and yaw by applying moments in the wanted DOF. During the decay tests, the wind turbine was in parked condition to avoid rotating blades. The response of the turbine was written out to a result file, and post-processing was performed with MATLAB. The parameters used in the decay tests are presented in Table 6.1. The decay tests were carried out for the model based on frequency domain analysis and the model based on strip theory. Figure 6.1 shows the responses from the decay tests in surge, heave, pitch, and yaw.

DoF	Const. Force	Ramp Force	Constant Dur.	Ramp Dur.	Simulation Length
Surge	500 kN	10 kN	100 s	50 s	1000 s
Heave	3500 kN	70 kN	100 s	50 s	1000 s
Pitch	36000 kNm	720 kNm	100 s	50 s	1000 s
Yaw	15000 kNm	300 kNm	100 s	50 s	1000 s

Table 6.1: Simulation parameters for the decay tests

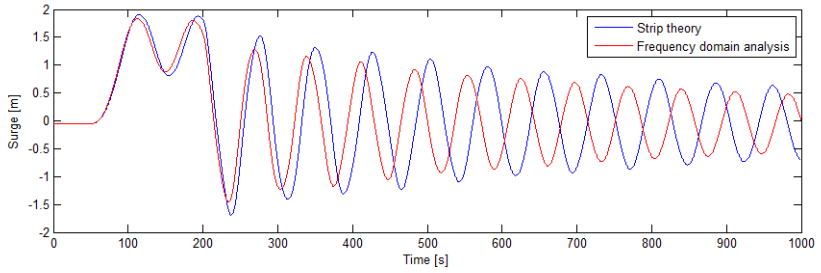

(a) Surge

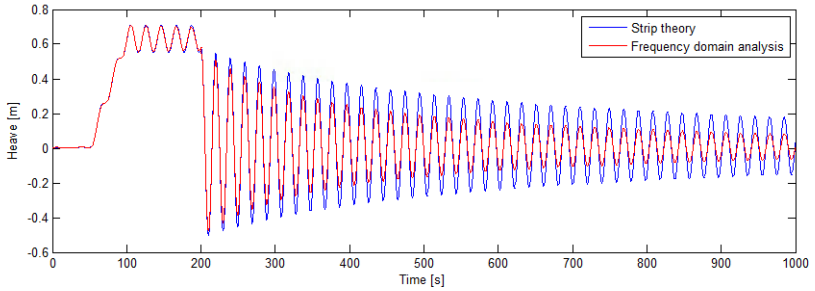

(b) Heave

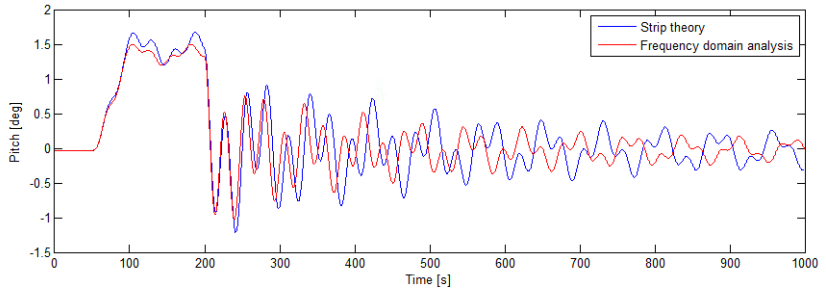

(c) Pitch

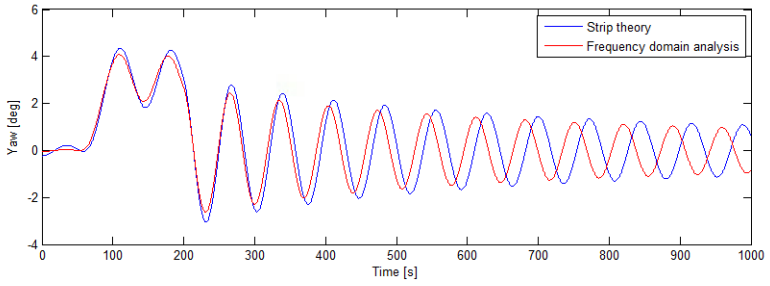

(d) Yaw

Figure 6.1: Free decay tests

The decay test in pitch shows that the motion is coupled. By looking at the effect of this decay test in the other degrees of freedom, it was found that the pitch motion was coupled with surge. This means that a surge motion was induced when pitch was excited.

The natural frequencies in each degree of freedom were obtained by a MATLAB-script given by co-supervisor Erin Bachynski. These are presented in Table 6.2. The natural period in surge is 76 s. According to [2] the natural period in surge is normally found between 1 and 2 minutes for semi-submersibles. However, due to the short length of the suspended mooring line, the natural period is much lower than the one defined for the same model defined in Lifes50+ [11] where the water depth was 130 m.

The difference between the natural period of the two models is small in surge and heave, but larger in pitch and yaw. This difference is due to the difference in added mass.

DoF	$T_{n,frequency\ domain}$ $[s]$	$T_{n,strip\ theory}$ $[s]$	Difference
Surge	76.49	76.18	0.4 %
Heave	19.39	19.42	0.1%
Pitch	26.59	27.79	4.3 %
Yaw	69.43	72.12	3.7 %

Table 6.2: Natural periods found from decay tests

Table 6.3 shows the linear and quadratic damping obtained from the decay tests. The damping in heave is much lower for the strip theory model, and this can also be seen from Figure 6.1b.

DoF	$q_{1,frequency\ domain}$	$q_{1,strip\ theory}$	$q_{2,frequency\ domain}$	$q_{2,strip\ theory}$
Surge	0.00186	0.0015	0.0142	0.0145
Heave	0.00221	0.0008	0.0589	0.0290
Pitch	-	-	-	-
Yaw	0.00044	0.00032	0.02066	0.01833

Table 6.3: Linear and quadratic damping obtained from decay test

6.1.1 Comparison With Spring Model

In the project thesis [1], decay tests were carried out for the numerical model, but with a mooring system modeled as a linear spring. The linear spring was modeled by adding horizontal stiffness directly into the hydrostatic stiffness matrix. The stiffness

was calculated based on the natural period in surge, according to [11]. Table 6.4 shows the natural periods obtained from decay tests for the two models. The natural period in surge and yaw for the model with the realistic mooring lines is much smaller than for the model with linear springs. The realistic mooring system is designed for a water depth of 50 m. A shorter line causes a stiffer system, which according to Equation 6.1 gives a lower natural period [2].

$$T_{ni} = 2\pi\sqrt{\frac{M_{ii} + A_{ii}}{C_{ii}}} \tag{6.1}$$

The hydrostatic stiffness in surge for the spring model was calculated based on the natural period of the OO Star 10 MW Wind Floater located in 130 m water depth. It was therefore expected that this natural period was much larger. Also, the mooring line designs are not identical. The mooring line design was not considered a focus in the current project, so the recommendation of further work could be to study a feasible design of the mooring system to the OO Star 10 MW Wind Floater for 50 m water depth.

DoF	$T_{n,frequency\ domain}$ $[s]$	$T_{n,strip\ theory}$ $[s]$	Difference
Surge	76.49	200.4	61.8 %
Heave	19.39	19.6	1.07%
Pitch	26.59	29.33	9.3 %
Yaw	69.43	116.28	40.3 %

Table 6.4: Comparison of natural periods obtained with current model with model from project thesis

6.2 Constant Wind Test

A constant wind test was carried out to verify the performance of the wind turbine, to find out which wind speeds give maximum offset in surge and pitch, and to find the mooring line tension at different offsets. 1000 s long time-domain simulations were performed with constant wind for 16 different wind speeds. The wind applied was stationary uniform with shear profile, and the value of the horizontal wind velocity was applied at the hub height of the turbine. The significant wave height was set to 0.01 m and the peak period to 20 s to avoid the effect of incoming waves. Only the model based on frequency domain analysis was used for the constant wind test. From Figure 6.2a and 6.2b, it can be seen that the generator power, generator torque, and the rotor speed becomes constant when the wind speed exceeds the rated wind speed. This is in

accordance with the performance curves of a 10 MW wind turbine given in the lecture notes of *Integrated Dynamic Analysis of Wind Turbines* [43]. The rotor thrust decays after the rated wind speed is reached due to the change of the blade pitch. As explained in Section 5.8.4, this is regulated by the blade-pitch controller and prevents the wind turbine from getting damaged.

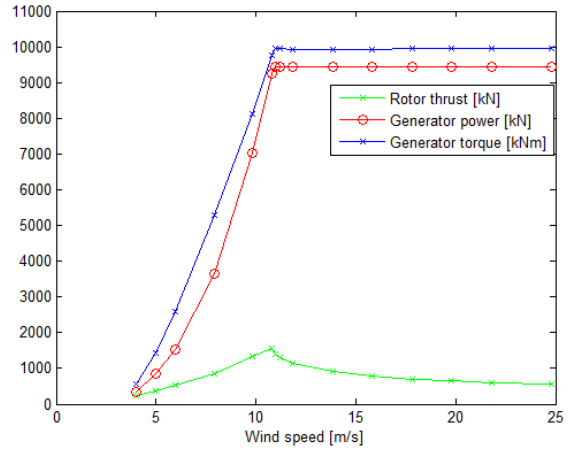

(a) Rotor thrust, generator power and generator torque

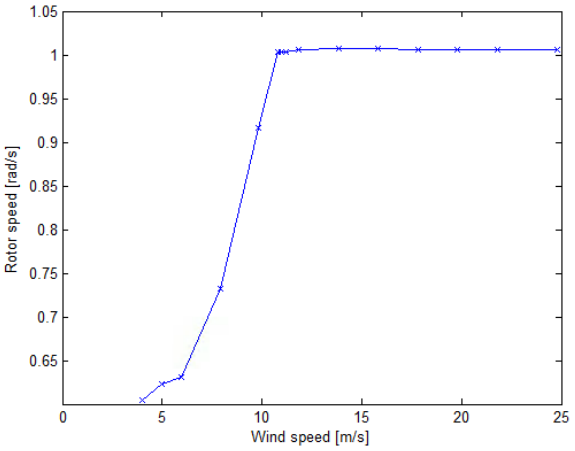

(b) Rotor speed

Figure 6.2: Rotor thrust, generator power and generator torque as a function of wind speed

Figure 6.3a and 6.3b shows that the rated wind speed gives the largest offset in surge and pitch. This was expected since, at higher wind speeds, the thrust is reduced due to the blade-pitch change. Since these two graphs follow the same trend as the graph of the rotor thrust, it was concluded with that the wind turbine was working as it should.

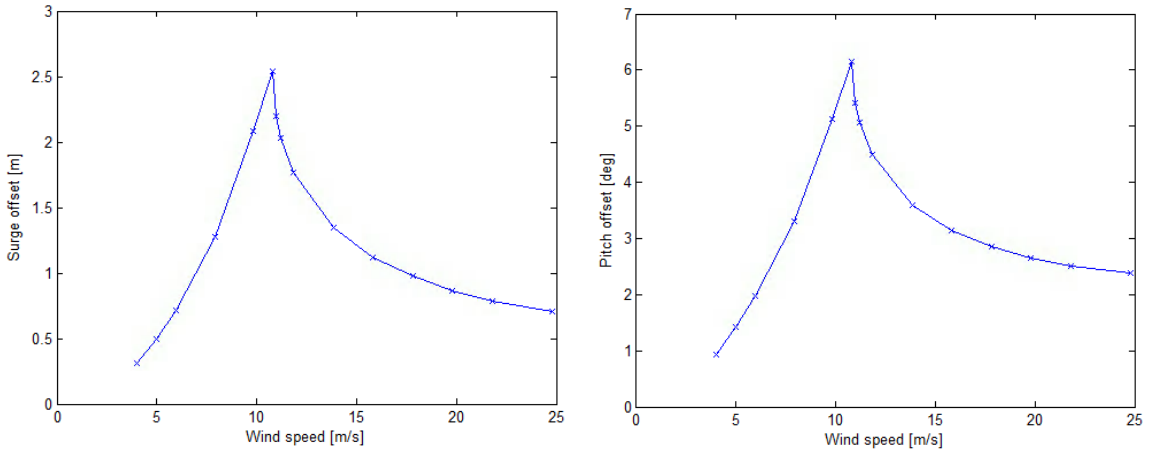

(a) Surge (b) Pitch

Figure 6.3: Surge and pitch offsets as a function of constant wind speed

Time-series of the surge and pitch motions, as well as the mooring line tension in two different lines are presented below in Figure 6.4 and 6.5 for four different wind speeds. For all motions, it can be seen that the mean offset is largest at the rated wind speed. This is also the case for wind speed at 40 m/s, which corresponds to extreme weather. At this wind speed, the wind turbine is parked, and the blades are feathered. The graph representing the surge motion shows that the damping in surge is small. The oscillating period of the mooring line tension is the same as the surge natural period. The graphs show that the floating wind turbine behaves as it should and the performance of the wind turbine is therefore verified.

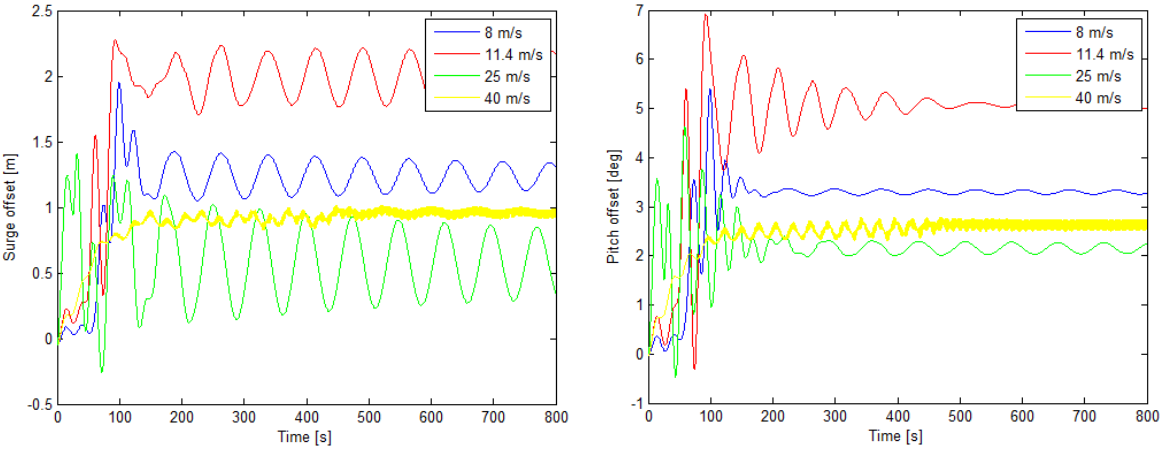

(a) Surge (b) Pitch

Figure 6.4: Time series of constant wind test

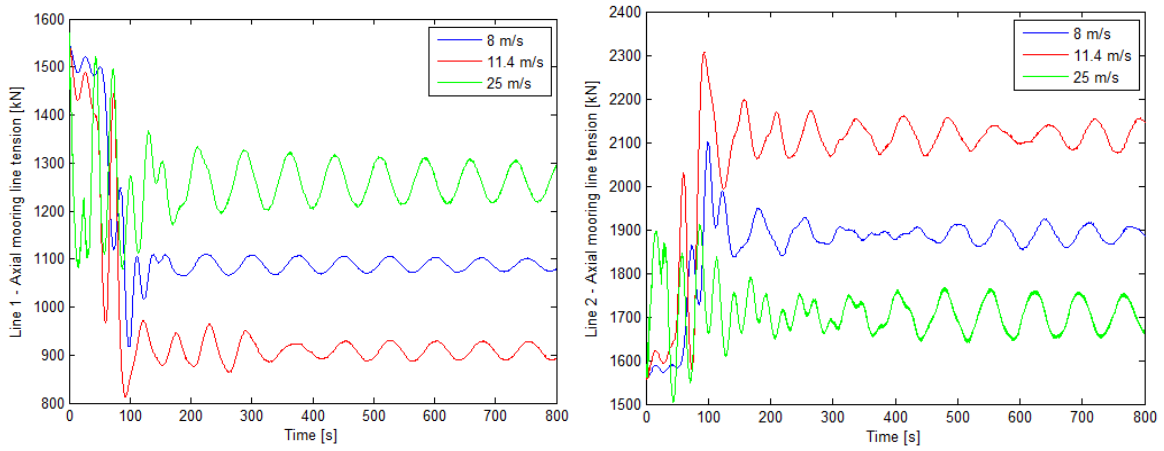

(a) Mooring line 1

(b) Mooring line 2

Figure 6.5: Time series of mooring line tension during constant wind test

The motions of the floating wind turbine obtained from the constant wind test are erroneous compared to a real case. Waves and currents induce damping which will reduce the offsets obtained in this test.

6.3 Regular Wave Response

A regular wave test was carried out for the linear frequency domain analysis model and the strip theory model. A time-series of regular waves was carried out for 1000 s for waves with a period from 5 s to 35 s. Wind and current were set to zero.

The response amplitude operators(RAOs) were obtained by plotting the response amplitude-to-wave elevation ratio. Figure 6.6 shows the RAOs in surge, heave, and pitch. The RAOs of the strip theory model follows the same trend as the frequency domain analysis model, but the responses are underestimated in all motions. This is most likely caused by the difference in the added mass and radiation damping of the two models.

The peaks of the RAOs are shifted two seconds to the right compared to the natural frequencies obtained from the decay test. It was checked to see if this was due to the viscous damping added to the structure, and regular wave tests were performed with and without the drag coefficients. However, this did not change the results. Thus, the reason for this shift was not found.

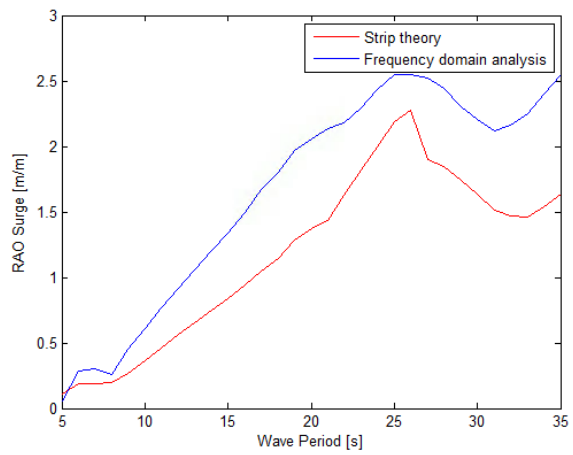

(a) Surge

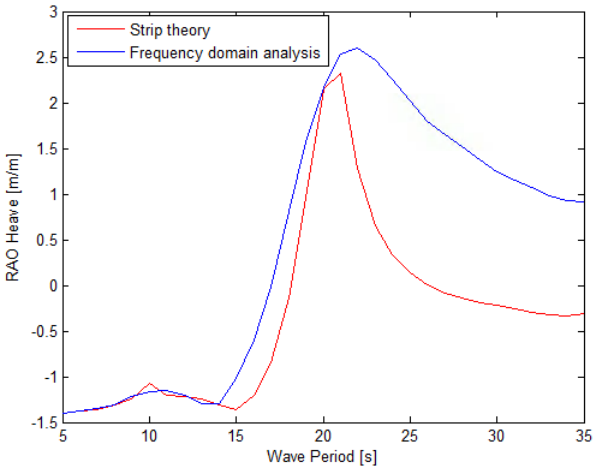

(b) Heave

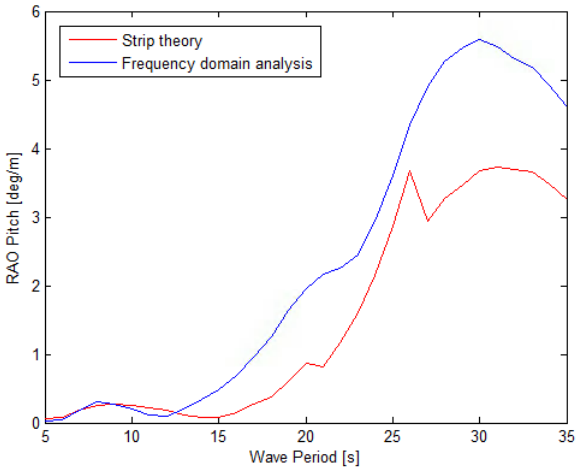

(c) Pitch

Figure 6.6: RAOs in regular waves surge, heave and pitch

6.4 Comparison of Mean Drift Force

In WADAM, the mean drift forces are calculated with two different methods: Direct pressure integration and conservation of momentum. These two methods are described in Section 3.2.2. The difference between the results obtained with these two methods is a good indication of how good the mesh of the panel model is. A small difference indicates that the mesh is good. Figure 6.7 shows the dimensionless mean drift force calculated by the two methods in surge. At small wave periods, the difference between the two methods is larger than at long-wave periods. This is because the panels are relatively large compared to the incoming wave, which causes a larger error of the calculated force. The two methods show good agreement at wave periods of 7 s and larger. Since the wave peak periods used in the simulations are 7.25 s and larger, the mesh was considered good enough to be used in further analyses.

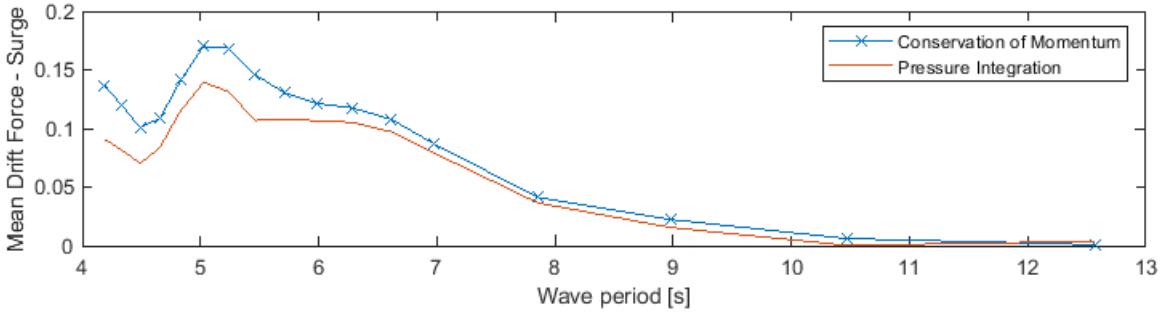

Figure 6.7: Comparison of dimensionless mean drift force calculated by conservation of momentum compared with pressure integration

Chapter 7

Behavior of Wind Turbine at 50 m Water Depth

This chapter provides the results obtained from coupled time-domain simulations and presents the behavior of the floating wind turbine in operational and extreme conditions. The simulations were carried out with the LFDA-model and with the LFDA-model including the full QTF. The results are compared and discussed in the following sections. Load cases with number 1 had no wind included, and load cases with number 2 included wind. The responses, hydrodynamic loads and the mooring line tensions are the parameters that are studied when analyzing the behavior of the floating wind turbine

7.1 Quadratic Transfer Functions

The quadratic transfer functions obtained from second-order frequency domain analysis are presented in Figure 7.1 for surge, heave, and pitch. As expected, Newman's approximation underestimates the difference-frequency loads in heave and pitch. However, it shows good agreement with the full QTF in surge.

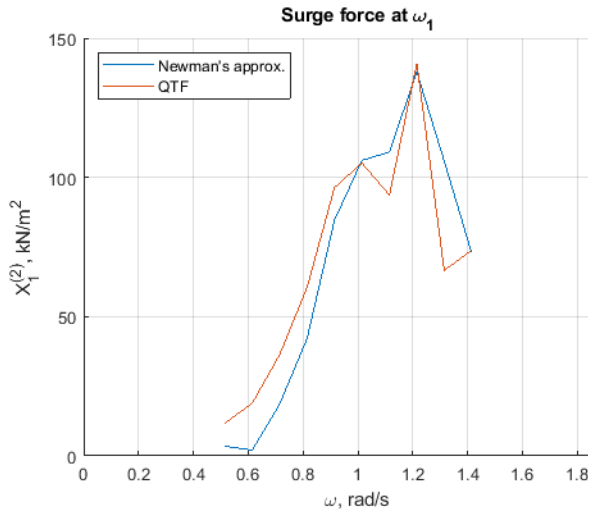

(a) Surge

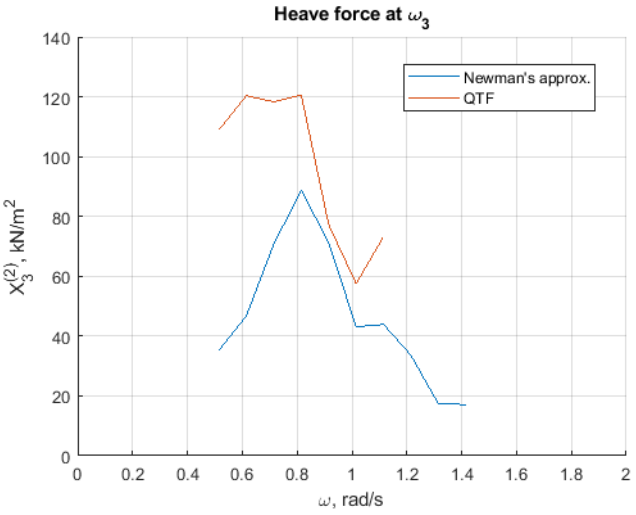

(b) Heave

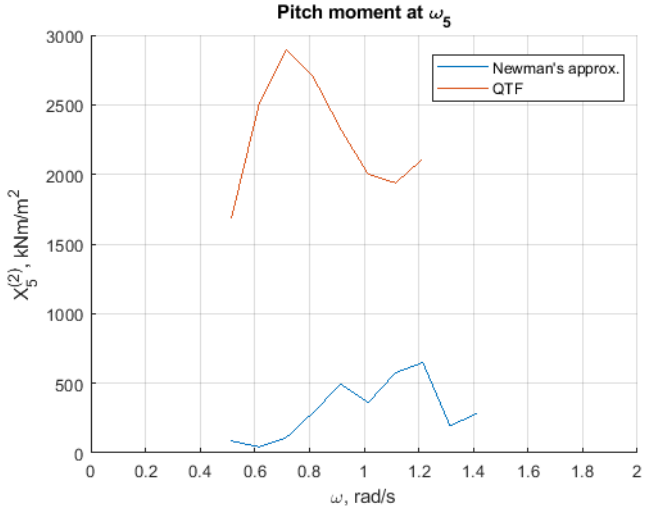

(c) Pitch

Figure 7.1: QTFs for surge, heave and pitch

7.2 Response of Floating Wind Turbine

The response of the floating wind turbine for each load case was studied and is presented in this section. A statistical analysis was carried out to find the standard deviation of the rigid body motions in surge, heave, and pitch, which were the dominating motions when the wave heading was of 0 degrees. At shallower water depths, the increment of the mooring line tension for increasing offsets reaches non-linear behavior earlier

than at deeper water. The horizontal motions of the platform are the main parameters affecting the mooring line tension. Therefore, the maximum and mean values of the motions in surge are presented and discussed. The first 1000 seconds of the simulation were removed when carrying out the statistical analysis to avoid the transient phase of the time-series. The impact of the waves on the rigid body motion was studied by comparing the same load case with and without wind.

7.2.1 Load Cases: O.1 and O.2

Load case O.1 and O.2 represent operational conditions where the mean annual wind speed of 8.5 m/s was used. These load cases correspond to the environmental condition that the floating wind turbine is most likely to experience. Table 7.1 shows the standard deviation of the rigid body motions for both load cases. The standard deviations are small, but the difference between the results obtained from the linear model and the model accounting for second-order effects is 36 % in surge which shows that it is important to consider this effect when analyzing the motions of the semi.

O.1	1st order	1st + 2nd order	Difference
Surge $[m]$	0.15	0.23	36.0 %
Heave $[m]$	0.04	0.05	16.3 %
Pitch $[deg]$	0.09	0.12	24.8 %
O.2	1st order	1st + 2nd order	Difference
Surge $[m]$	0.45	0.48	7.0 %
Heave $[m]$	0.04	0.051	18.6 %
Pitch $[deg]$	0.09	0.89	0.3 %

Table 7.1: Standard deviation of floater motions for load case O.1 and O.2

The mean and maximum values for surge for load case O.1 and O.2 are presented in Table 7.2. The mean value of the surge motion for load case O.1 is 0.36 m, which is small considering the dimensions of the platform. This corresponds to a small increase in mooring line tension, which will be discussed in Section 7.4. The maximum value of the surge offset for the load case with wind for the models including second-order effects, is 65 % larger than without wind. This corresponds to 2.6 m and shows that for this environmental condition, the wind load is the dominating parameter when it comes to the offset in surge. From the constant wind test it was seen that the mean value of the surge offset at rated wind speed was 2.5 m. This corresponds to load case O.2. However, du to turbulent wind and damping due to waves and current, the mean value of surge in O.2 is only 2 m.

O.1	1st order	1st + 2nd order	Difference
Mean $[m]$	0.29	0.38	24.8%
Max $[m]$	0.94	1.34	29.8%
O.2	1st order	1st + 2nd order	Difference
Mean $[m]$	1.89	2.00	5.4%
Max $[m]$	3.61	3.94	8.3 %

Table 7.2: Mean and maximum values of floater motions for load case O.1 and O.2

Figure 7.2 shows the PSDs of O.1 and O.2 in surge, heave, and pitch. In the two surge spectra, the first peak is found at $\omega = 0.08\, rad/s$, which coincides with the natural frequency in surge. For these load cases, the response from the low-frequencies is much larger than for wave frequencies in all cases. All spectra show that the model which not consider second-order effects underestimates the motions at low frequencies. This is in accordance with the findings presented in the literature survey in Section 2.2. The heave spectra have one peak at $0.3\, rad/s$, which is the natural frequency in heave. The largest peak in the pitch spectra for O.1 corresponds to the natural period in surge. This occurs due to the coupling effect between pitch and surge. The pitch spectra for load case O.2 shows a high response for $\omega = 0\, rad/s$. This is due to the mean value of the pitch motion that is generated by the wind.

The spectra for heave and pitch motions of load case O.2 gives larger values on the y-axis than case O.1. This shows that the wind has a large impact on these motions, while the heave motions are only affected by the waves.

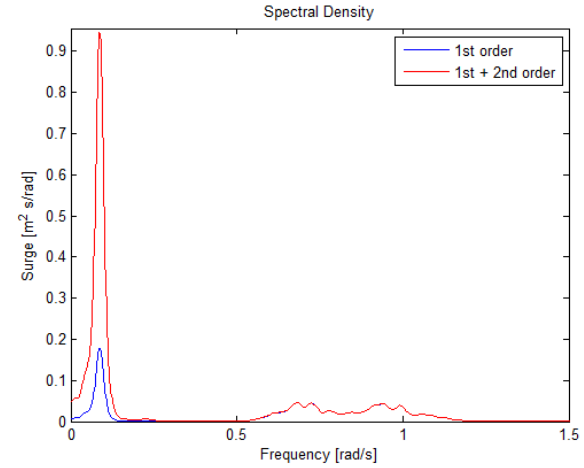

(a) Surge O.1

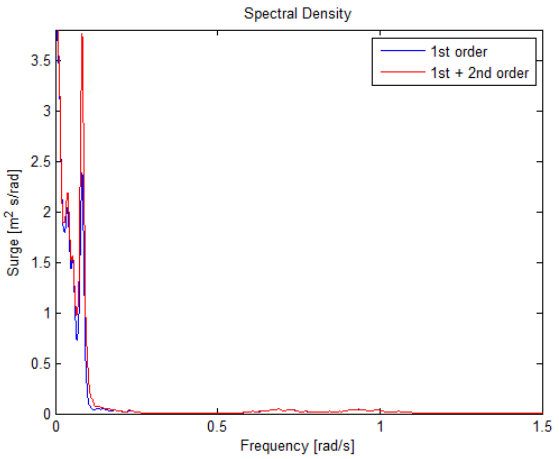

(b) Surge O.2

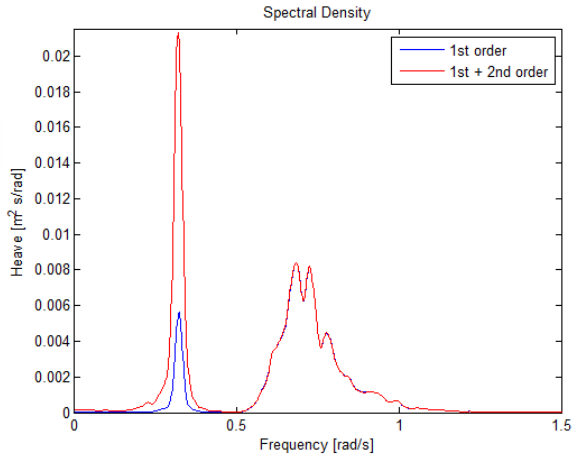

(c) Heave O.1

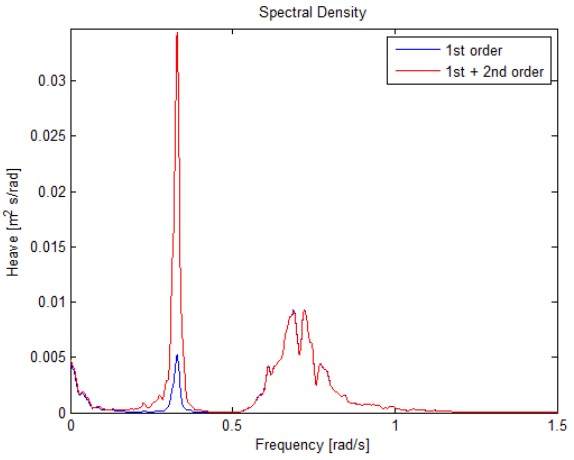

(d) Heave O.2

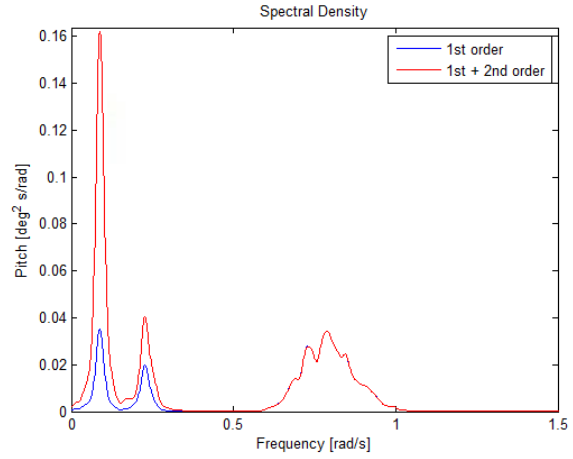

(e) Pitch O.1

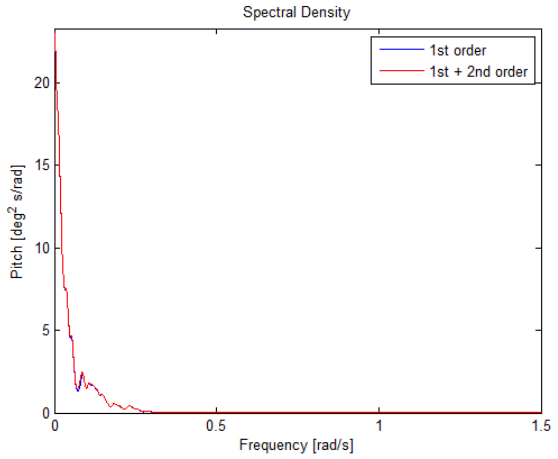

(f) Pitch O.2

Figure 7.2: Response spectra of load case O.1 and O.2 in surge, heave and pitch.

7.2.2 Load Cases: C.1 and C.2

Load case C.1 and C.2 are still within the operational conditions of the floating wind turbine, but the wind speed at hub-height is close to the cut-off speed and the significant wave height and peak period, induced by the wind velocity, are higher. The standard deviations of the motions are presented in Table 7.3. The difference between the standard deviation of the load case with and without wind is smaller than for load case O.1 and O.2. However, the responses are larger. The difference between the simulations including and not including second-order effects are larger in surge and pitch than in heave.

C.1	1st order	1st + 2nd order	Difference
Surge $[m]$	0.97	1.18	18.3 %
Heave $[m]$	0.29	0.32	10.9 %
Pitch $[deg]$	0.36	0.44	18.7 %
C.2	1st order	1st + 2nd order	Difference
Surge $[m]$	1.03	1.27	18.7 %
Heave $[m]$	0.29	0.32	9.6 %
Pitch $[deg]$	0.75	0.79	4 %

Table 7.3: Standard deviation of floater motions for load case C.1

The mean and maximum values of the surge motion are presented in Table 7.4. The mean values for the linear model are almost the same for C.1 and C.2, but when including second-order effects, the mean value of C.2 is 52.3 % larger than C.1. The second-order effects also show a significant increase in the maximum values compared to the linear model.

C.1	1st order	1st + 2nd order	Difference
Mean $[m]$	0.62	0.92	25.2%
Max $[m]$	5.13	6.65	22.8%
C.2	1st order	1st + 2nd order	Difference
Mean $[m]$	0.63	1.94	67.5%
Max $[m]$	5.89	7.89	25.3%

Table 7.4: Mean and maximum values of floater motions for load case C.1 and C.2

The response PSDs are given in Figure 7.3. The surge spectra show the same trend as for load case O.1 and O.2, but the magnitude of the response is much larger. In heave, the response at the wave frequency from $\omega = 0.5\,rad/s$ to $\omega = 0.8\,rad/s$ is larger than at the low-frequency motions. The linear potential theory model also underestimates

the low-frequency motions for these load cases as well as for O.1 and O.2. In the pitch spectra, a large peak was found at the frequency coinciding with the natural frequency in surge. This is due to the coupling effect of pitch and surge, which could be seen from the decay test in pitch in Section 6.1.

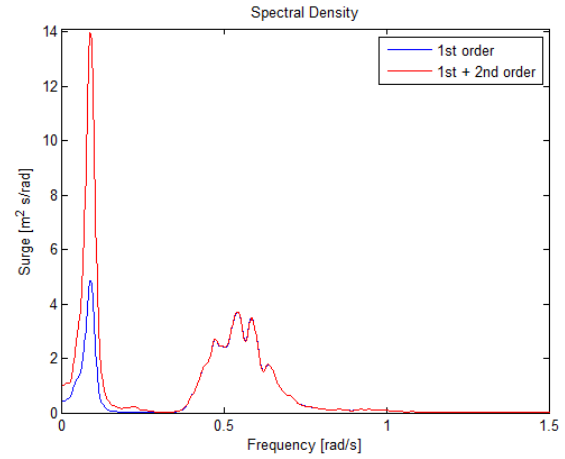

(a) Surge C.1

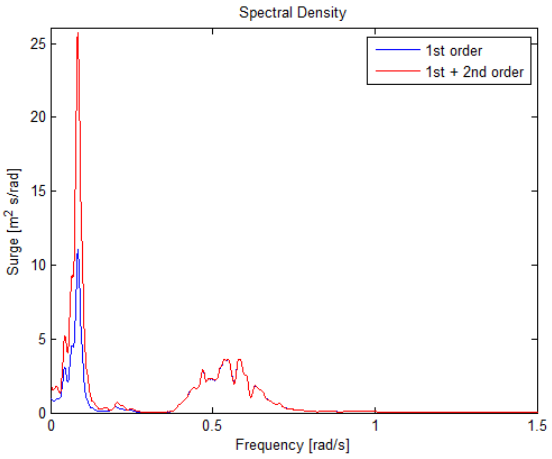

(b) Surge C.2

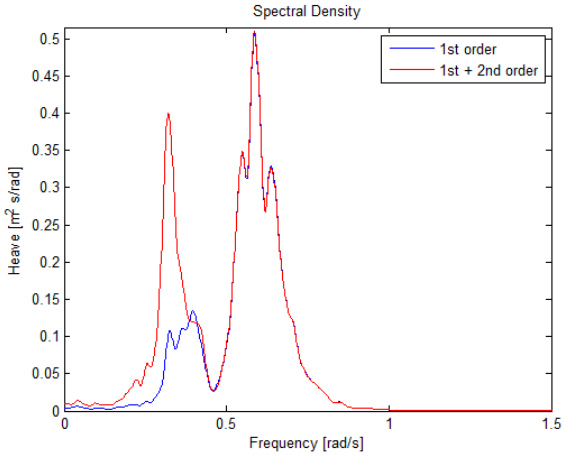

(c) Heave C.1

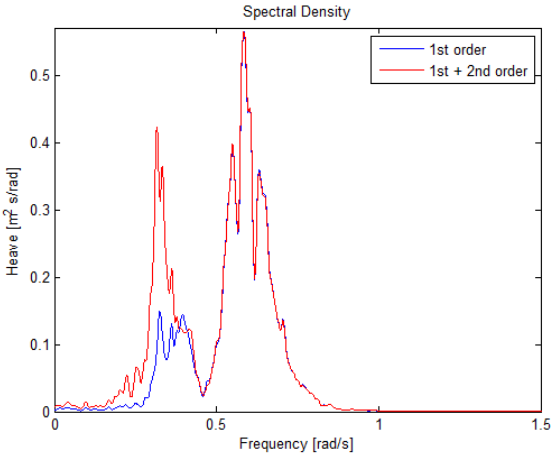

(d) Heave C.2

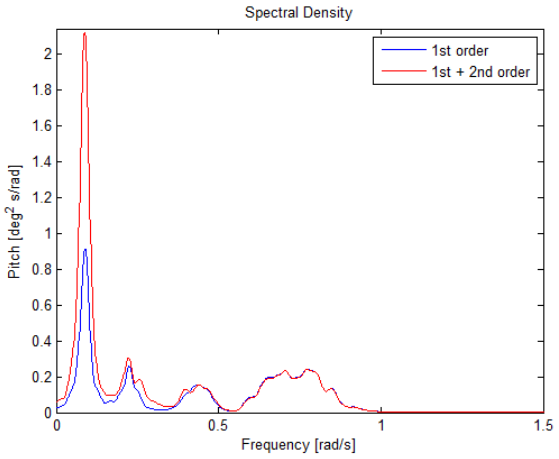

(e) Pitch C.1

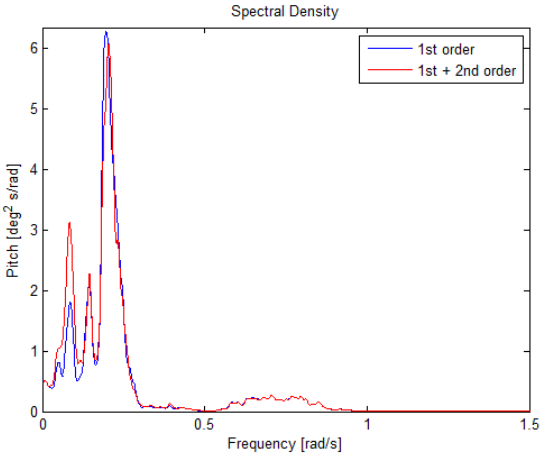

(f) Pitch C.2

Figure 7.3: Response spectra of load case C.1 and C.2 in surge, heave and pitch.

7.2.3 Load Cases: X.1 and X.2

Load case X.1 and X.2 represent extreme conditions with and without wind, respectively. In this weather condition, the wind turbine is parked which means that the blades are feathered and restrained from rotating. The standard deviations of the motions are seen in Table 7.5. The offset in surge is significantly larger than for the operational cases. The pitch motion does not change much from X.1 to X.2 since the blades are restrained from rotating. The large waves also result in larger heave motions, and the standard deviation of 1.5 m is high compared to the other cases. The difference between the two load models is small. The possible reason for this is that according to the literature survey conducted on second-order effects carried out by [18], difference-frequency loads have little effect during extreme load cases. The maximum

X.1	1st order	1st + 2nd order	Difference
Surge $[m]$	3.06	3.09	0.8 %
Heave $[m]$	1.48	1.55	1.4 %
Pitch $[deg]$	1.40	1.41	0.5 %
X.2	1st order	1st + 2nd order	Difference
Surge $[m]$	2.99	3.03	1.3%
Heave $[m]$	1.43	1.45	1.5%
Pitch $[deg]$	1.95	1.96	0.8%

Table 7.5: Standard deviation of floater motions for load case X.1 and X.2

and mean values are listed in Table 7.6. In Figure 5.4 the mooring line tension as a function of the horizontal offset is presented. This graph showed that the mooring line tension reaches the maximum breaking strength at an offset of approximately 8 m. The maximum offset from the time-domain simulation was 19.21 m, which according to Figure 5.4, is above the offset limit. However, this graph do not take into account the elasticity of the mooring line. An further investigation of the mooring line tension was carried out and is presented in Section 7.4. The PSD of the response in surge,

X.1	1st order	1st + 2nd order	Difference
Mean $[m]$	4.46	4.82	8.2 %
Max $[m]$	16.28	15.48	5.5%
X.2	1st order	1st + 2nd order	Difference
Mean $[m]$	7.84	8.12	4.4 %
Max $[m]$	19.21	18.85	1.9 %

Table 7.6: Mean and maximum values of floater motions for load case X.1 and X.2

heave and pitch are shown in Figure 7.4. The spectra for load case X.1 shows that there are little difference between the responses of the two load models.

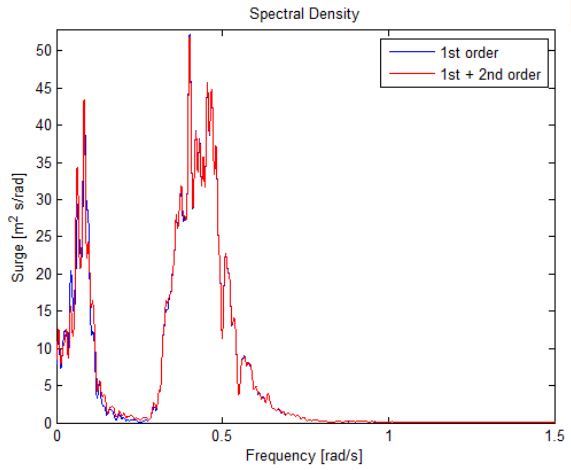

(a) Surge X.1

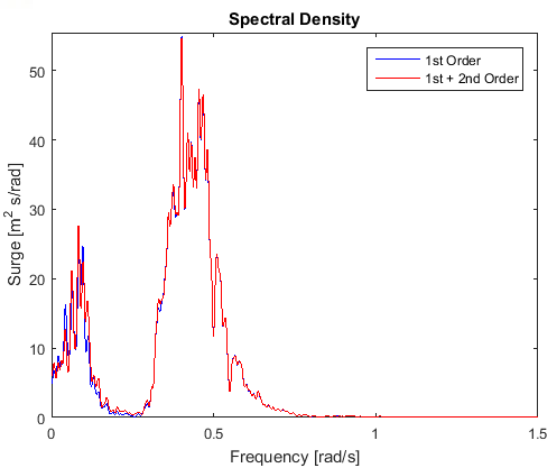

(b) Surge X.2

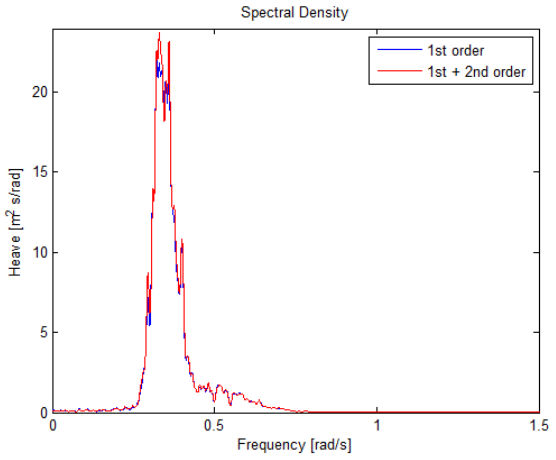

(c) Heave X.1

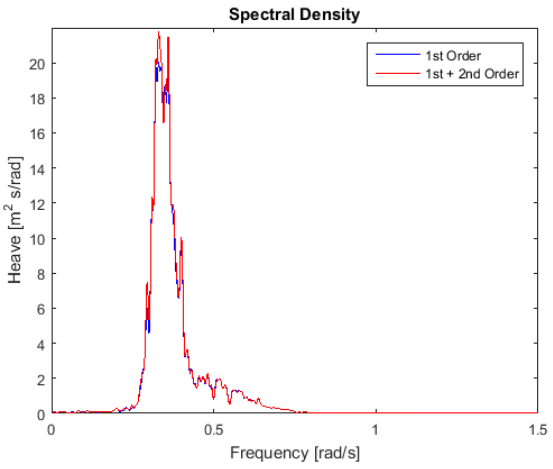

(d) Heave X.2

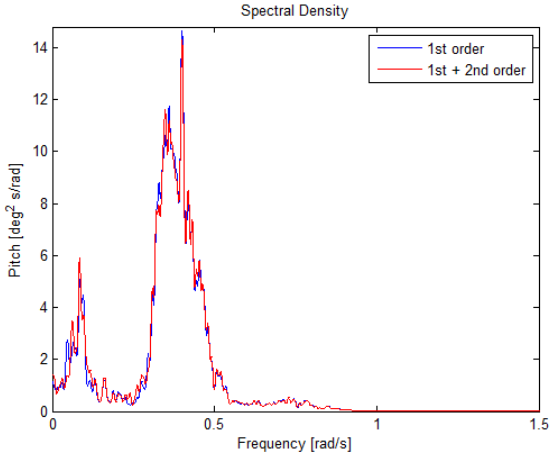

(e) Pitch X.1

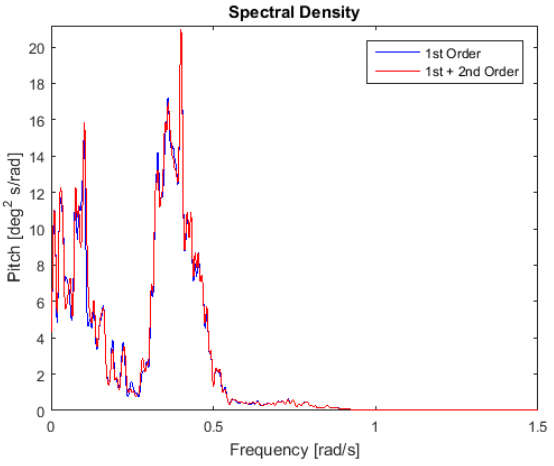

(f) Pitch X.2

Figure 7.4: Response spectra of load case X.1 and X.2 in surge, heave and pitch.

7.3 Loads on the Floating Wind Turbine

The hydrodynamic loads acting on the wind turbine are important to study to get a better understanding of the responses demonstrated in the previous section. Load case O.1, C.1, and X.1 are considered since the hydrodynamic loads are the same when and when not including wind.

7.3.1 Aerodynamic Loads

The aerodynamic loads acting on the wind turbine in the load cases including wind are presented in Table 7.7. The aerodynamic force acts in the x-direction while the aerodynamic moment is the moment in the y-direction, affecting the pitch motion. These loads are contributing to the response in surge and pitch, which can be seen on the difference in the response values between the wind and no wind cases. The forces are small compared to the first-order wave loads.

	Aerodynamic Force $[kN]$	Aerodynamic Moment $[kNm]$
O.2	70.46	2629
C.2	157.63	5492
X.2	341.57	6934

Table 7.7: Standard deviation of aerodynamic load in load cases including wind

7.3.2 Load Cases: O.1 and O.2

The standard deviation of the first and second-order wave forces for load case O.1 and O.2 are presented in Table 7.8. The second-order force is 2.3% of the first-order force in surge, and even smaller in heave and pitch.

O.1	Surge $[kN]$	Heave $[kN]$	Pitch $[kNm]$
1st Order	2684.7	1115.6	38457.1
2nd Order	62.6	38.1	944.2

Table 7.8: Standard deviation of the wave loads for load case O.1

In Figure 7.5, the load PSDs of the surge, heave, and pitch motions are presented. When the peak period is low, the contribution from the second-order wave loads is small as seen in the PSDs. It can be seen that the first-order wave frequency only appears at the wave frequencies from 0.5-1.8 rad/s. However, from the previous section, it was seen that the largest motions of the body were found at lower frequencies. This is due to the second-order difference-frequency loads that induce oscillating motions at the resonance frequency in surge, pitch and heave. It is therefore considered important to include the second-order effects even though the second-order loads are small compared to first-order loads.

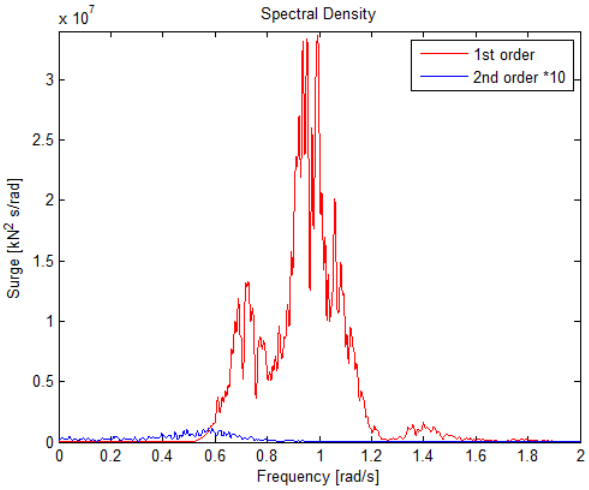

(a) Surge O.1

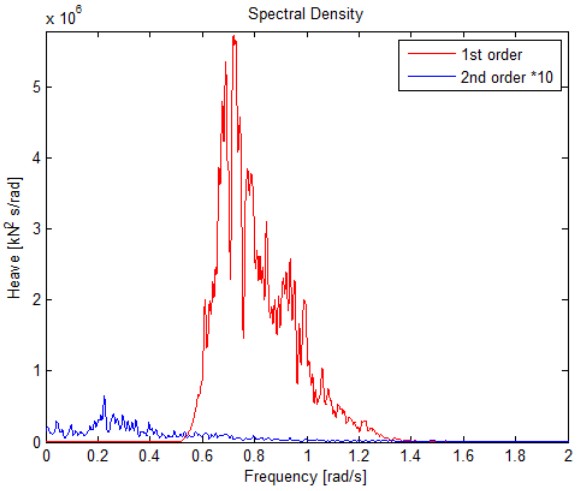

(b) Heave O.1

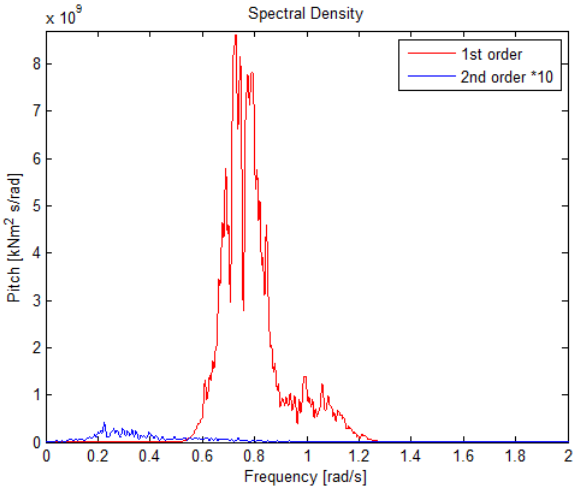

(c) Pitch O.1

Figure 7.5: Load PSD of first-order wave loads and second-order difference-frequency load of load case O.1 and O.2 in surge, heave and pitch.

7.3.3 Load Cases: C.1 and C.2

The standard deviations of first and second-order loads acting on the body for load case C.1 and C.2 are listed in Table 7.9. The second-order loads are still only 3.5 % of the first-order wave loads in surge. However, as for the hydrodynamic load of load case O.1 and O.2 presented in the section above, large responses are found for the low frequencies which are induced by the second-order loads. The standard deviation for the second-order loads is larger since the peak period is larger.

C.1	Surge $[kN]$	Heave$[kN]$	Pitch$[kNm]$
1st Order	9057.6	5535.9	161730.6
2nd Order	322.7	281.8	7142.6

Table 7.9: Standard deviation of the wave loads of load case C.1

The PSDs of the loads are presented in Figure 7.6. The second-order forces are small compared to the first-order wave forces, but are dominating the low-frequency regions and cause large motions, as seen in Figure 7.3.

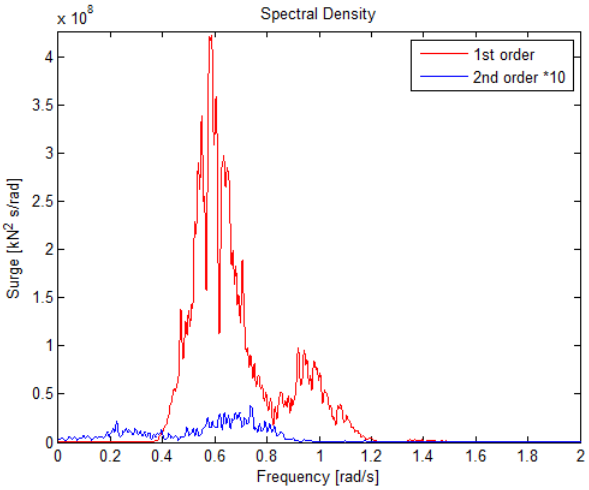

(a) Surge C.1

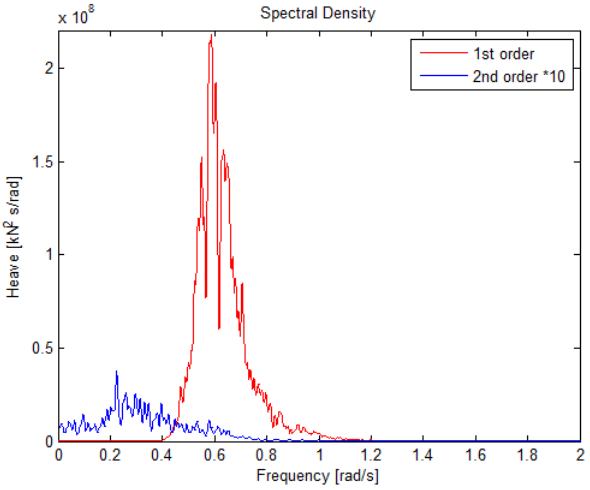

(b) Heave C.1

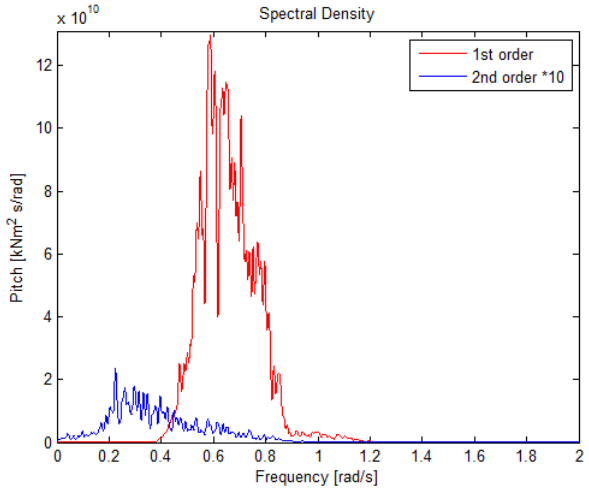

(c) Pitch C.1

Figure 7.6: Load PSD of first-order wave loads and second-order difference-frequency load of load case C.1 and C.2 in surge, heave and pitch.

7.3.4 Load Cases: X.1 and X.2

The standard deviation of the loads are presented in Table 7.10. The second-order loads are significantly large in heave and pitch, compared to the two other load cases. The large significant wave height and peak period result in a large standard deviation of loads.

X.1	Surge $[kN]$	Heave$[kN]$	Pitch $[kNm]$
1st Order	17220.0	9139.9	268208.5
2nd Order	737.5	714.2	18550.8

Table 7.10: Standard deviation of the wave loads for load case X.1

Figure 7.7 shows the load PSD for load case X.1. The contributions from the second-order wave loads are larger in all motions. The heave and pitch spectra are most dense around the natural periods. The peak period for these load cases is 14 s which corresponds to $0.44\,rad/s$. From the response spectra in Figure 7.4 it can be seen that the peaks of the response spectra are exactly at this frequency. However, according to the load PSDs, the peak is shifted slightly to the right. Due to the large peak period at this load case, the range of the second-order frequency loads is much larger than for the other two cases. However, the loads are still small compared to the first-order wave forces.

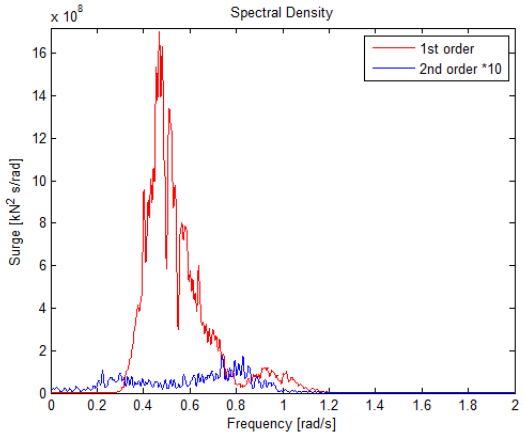

(a) Surge X.1

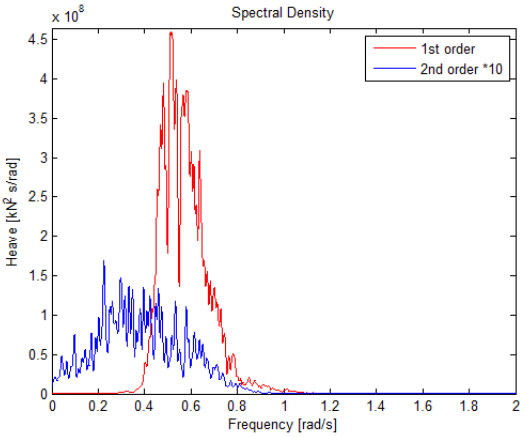

(b) Heave X.1

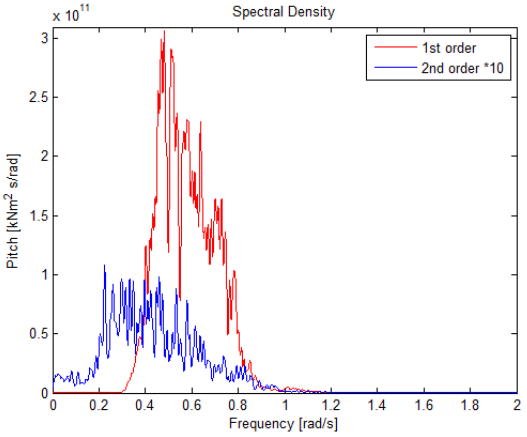

(c) Pitch X.1

Figure 7.7: Load PSD of first-order wave loads and second-order difference-frequency load of load case X.1 and X.2 in surge, heave and pitch

7.4 Mooring Line Tension

When studying the mooring line tension for the different cases, the load cases O.1 and O.2, were not taken into consideration since the offset in these cases was significantly small.

The mooring line tension was calculated for line 1 and 2, which are defined in Figure 5.1. This means that a larger offset gives smaller tension in line 1, but larger tension in line 2. The results obtained with the linear model were compared with the results obtained when including the second-order effects. The effect of the wind on the mooring line tension was also investigated.

7.4.1 Load Cases: C.1 and C.2

Table 7.11 gives the standard deviations of the mooring line tension for load case C.1 and C.2. When considering case C.1, the standard deviation of the mooring line tension in line 1 of the model including second-order effects is only 8% larger than the linear model and for line 2 it is 15.9% larger. However, when looking at the maximum values in Table 7.12, the value of model taking into account the second-order effects is respectively 436.5 % and 340.5 % larger for line 1 and 2, than the linear model. This trend is also true for load case C.2. The maximum mooring line tension of line 2 for case C.2 is 3419 kN. This is far from the breaking strength of the mooring line of 20 MN, but it is more than three times larger than the maximum value obtained from the linear model. This can also be seen from the PSDs of the mooring line tension of load case C.1 and C.2 shown in Figure 7.8. The largest value of the mooring line tension is found in the low-frequency range, which the linear model does not capture.

The maximum value of line 2 for the load case including wind is approximately 9% larger than the load case without wind.

C.1	Linear	Linear + full QTF	Difference
Line 1 $[kN]$	208.52	228.56	8 %
Line 2 $[kN]$	145.71	173.27	15.9 %
C.2	Linear	Linear + full QTF	Difference
Line 1 $[kN]$	153.02	169.91	9.9 %
Line 2 $[kN]$	188.34	226.33	16.8 %

Table 7.11: Standard deviation value of the mooring line tension from load case C.1 and C.2

C.1	Linear	Linear + full QTF	Difference
Line 1 $[kN]$	626.20	2733.58	436.5 %
Line 2 $[kN]$	914.36	3110.07	340.1%
C.2	Linear	Linear + full QTF	Difference
Line 1 $[kN]$	598.04	2133.66	356.8 %
Line 2 $[kN]$	966.15	3419.10	353.9 %

Table 7.12: Maximum value of the mooring line tension from load case C.1 and C.2

The PSDs of the mooring line tension in mooring line 1 and 2 can be seen in Figure 7.8. These spectra agree with the difference in the maximum values between the linear and non-linear models. The maximum values are found at the low frequencies, which the linear model does not capture, and the maximum mooring line tension is thus much smaller for this model. It can also be seen from load case C.2 that wind speed influences the mooring line tension in mooring line 2 due to the increase in horizontal offset.

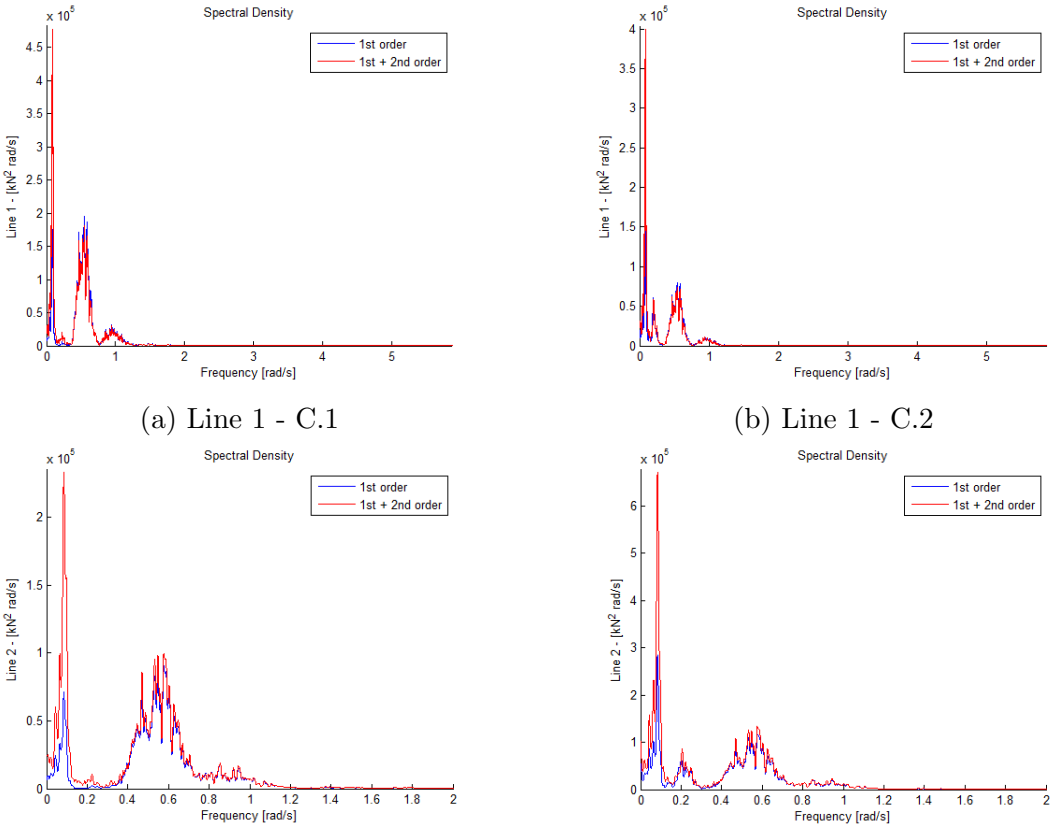

(a) Line 1 - C.1

(b) Line 1 - C.2

(c) Line 2 - C.1

(d) Line 2 - C.2

Figure 7.8: PSD Mooring line tension for mooring line 1 and 2 for load case C.1 and C.2

7.4.2 Load Cases: X.1 and X.2

The extreme conditions are the most critical conditions when it comes to mooring line tension. These load cases gave the largest responses and hydrodynamic loads. Table 7.13 shows the standard deviation of mooring line tension calculated with the linear and the non-linear load model. Small differences are found between the two models. The maximum values of the mooring line tension are presented in Table 7.14. For load case X.1, the maximum mooring line tension is almost 60 % of the maximum breaking strength(MBS) of the mooring line. When the wind is included in load case X.1, this value is very close to the MBS and improvements should be made to the mooring system. However, the tension do not exceed the breaking strength as it should have according to Figure 5.4. By comparing the values from X.1 and X.2 it can be seen that the wind has a great contribution to the mooring line tension. Different from load case

X.1	Linear	Linear + full QTF	Difference
Line 1 $[kN]$	544.42	539.31	0.9 %
Line 2 $[kN]$	1488.71	1512.05	1.5
X.2	Linear	Linear + full QTF	Difference
Line 1 $[kN]$	501.67	502.90	0.2 %
Line 2 $[kN]$	2412.56	2451.82	1.6%

Table 7.13: Standard deviation value of the mooring line tension from load case X.1 and X.2

X.1	Linear	Linear + full QTF	Difference
Line 1 $[kN]$	4362.85	5092.37	14.3 %
Line 2 $[kN]$	12544.88	11798.57	5.9%
X.2	Linear	Linear + full QTF	Difference
Line 1 $[kN]$	3787.92	3619.74	4.44 %
Line 2 $[kN]$	18033.81	17712.82	1.8%

Table 7.14: Maximum value of the mooring line tension from load case X.1 and X.2

C.1 and C.2, the maximum values of the mooring line tension are found at the wave frequency corresponding to the peak period. The PSDs of the mooring line tensions are shown in Figure 7.9. The largest peaks of the mooring line tensions are found at the wave frequency corresponding to the peak period of the sea state.

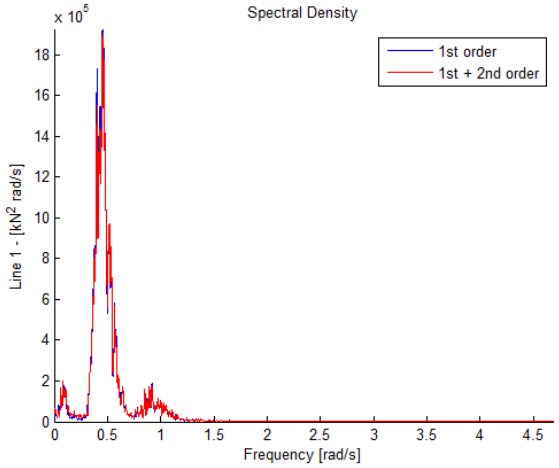

(a) Line 1 - X.1

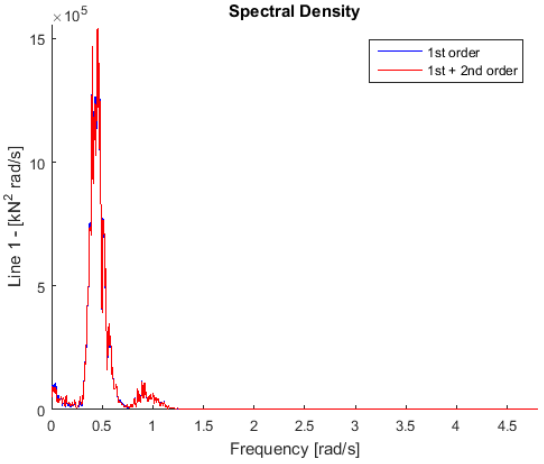

(b) Line 1 - X.2

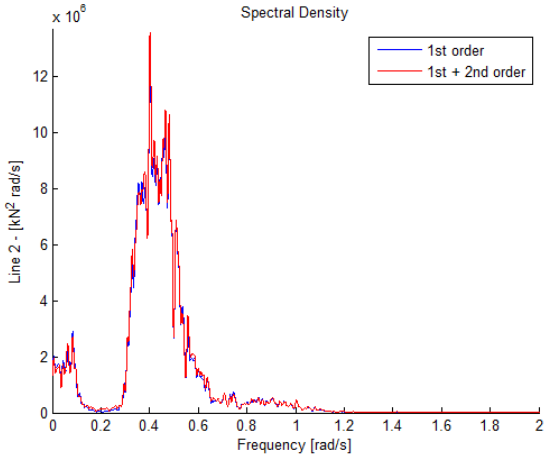

(c) Line 2 - X.1

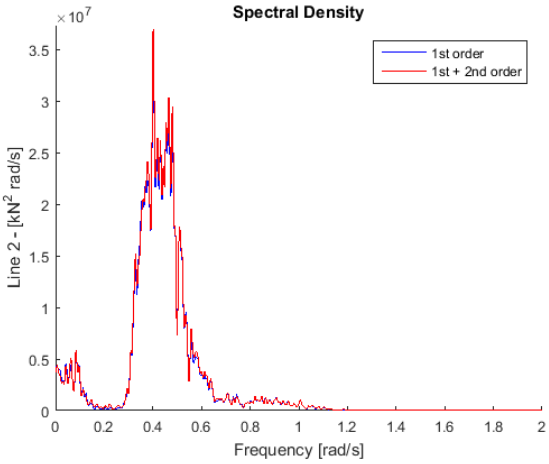

(d) Line 2 - X.2

Figure 7.9: PSD Mooring line tension for mooring line 1 and 2 for load case X.1 and X.2

7.5 Major Finding Regarding Behaviour

This section summarizes the most important findings when it comes to the behavior of the OO Star 10 MW Wind Floater at 50 m water depth.

- Linear potential theory underestimates the behavior of the low-frequency responses in cases where the wind turbine is operating. The difference in standard deviation and maximum value between the linear and non-linear model for these two cases is in average 27% and 26.3%, respectively. This is not seen for the extreme cases. According to [18], the difference-frequency effects become minimal for extreme cases.
- The heave motion was only affected by waves, and not by wind.
- It was found that for load cases including wind, the mean value of the surge motion was in average 176.7% larger than load cases without wind.
- First-order wave loads are much larger than second-order wave loads. However, the low-frequency loads excite resonant motions when the difference-frequency reaches the natural frequency of the body.
- The maximum offset in surge was in load case X.1 and was 19.21 m. Correspondingly, this load case also had the maximum mooring line tension of 18033.8 kN. This is only 2000 kN from the breaking strength of the mooring line and improvements of the mooring system is necessary.
- For load cases C.1 and C.2, the maximum mooring line tension is significantly underpredicted by linear potential theory. This is due to the low-frequency motions in surge which are not captured without accounting for second-order effects. Even though this difference is not present for the extreme load cases where the maximum mooring line tension is largest, the second-order effects were concluded to be extremely important to take into account since the maximum tension for load case C.1 and C.2, also was high. If the second-order effects are not taken into account when considering a moored structure, the consequences can be severe.
- It is also important to highlight the study carried out by [14], which showed that second-order difference-frequency loads are under-predicted in Wadam. This also means that the mooring line tension could be underestimated, which should be taken into consideration when analyzing a mooring system.

Chapter 8

Comparison of Hydrodynamic Load Models

In the previous chapter, it was concluded that the second-order effects are crucial to capture, to be able to calculate the responses and mooring line tension correctly. There are different ways of calculating the hydrodynamic loads and motions of the floating wind turbine. In this chapter results obtained by using a full QTF is compared with Newman's approximation, and the results from the LFDA-model are compared with a strip theory model.

8.1 Comparison Between Calculations With Full QTF and Newman's Approximation

An easier way of calculating the slow-drift motions is by applying Newman's approximation, which is described in Section 3.2.2. Simulations including a full QTF and Newman's approximation were carried out for all load cases and are compared. This section provides the results obtained from these simulations and the discussion of the applicability of Newman's approximation compared to the full QTF. In the following sections, a comparison of the two load models in surge, heave, and pitch, as well as the mooring line tension, is presented.

8.1.1 Surge

Table 8.1 shows the standard deviation of the surge motion for all load cases. The largest difference between the two methods is 6.7 % for load case O.1, but this differ-

ence only corresponds to 0.17 m. Since the offset in surge is directly related to the

LC	Full QTF	Newman's app.	Difference
O.1 $[m]$	0.235	0.252	6.7 %
O.2 $[m]$	0.482	0.49	1.6 %
C.1 $[m]$	1.18	1.15	2.54%
C.2 $[m]$	1.27	1.248	1.7 %
X.1 $[m]$	3.09	3.1	0.3%
X.2 $[m]$	3.03	3.02	0.3%

Table 8.1: Standard deviation of surge motion: Comparison of Newman's approximation and full QTF

mooring line tension, the maximum values of the offset for each load case are important to consider. These values are presented in Table 8.2. The largest difference between the max values is 6% for load case C.1, which corresponds to 0.4 m. This is very little compared to the dimensions of the floating wind turbine. Figure 8.1 shows the response PSDs of the surge motion for load case O.1, C.2 and X.1. The model applying Newman's approximation shows good agreement with the full QTF. The largest deviation is found at the low-frequencies for load case O.1 and C.2. For load case X.1, the difference is small at all frequencies. According to these findings, the Newman's approximation gives a good agreement with the full QTF. However, this cannot be concluded until the effect of Newman's approximation on the mooring line tension is investigated.

		Full QTF	Newman's approx	Difference
O.1	Mean $[m]$	0.386	0.411	6.0%
O.1	Max $[m]$	1.346	1.41	4.5%
O.2	Mean $[m]$	2.0057	2.03	1.19%
O.2	Max $[m]$	3.944	4.0	1.4 %
C.1	Mean $[m]$	0.925	1.016	8.9%
C.1	Max $[m]$	6.65	6.25	6.0%
C.2	Mean $[m]$	1.94	2.04	4.9%
C.2	Max $[m]$	7.89	7.44	5.7%
X.1	Mean $[m]$	4.82	4.93	2.2%
X.1	Max $[m]$	15.48	16.2	4.4%
X.2	Mean $[m]$	8.11	8.19	0.97 %
X.2	Max $[m]$	18.85	19.47	3.18%

Table 8.2: Mean and maximum values of floater motions for load case O.1 and O.2: Comparison of Newman's approximation and full QTF

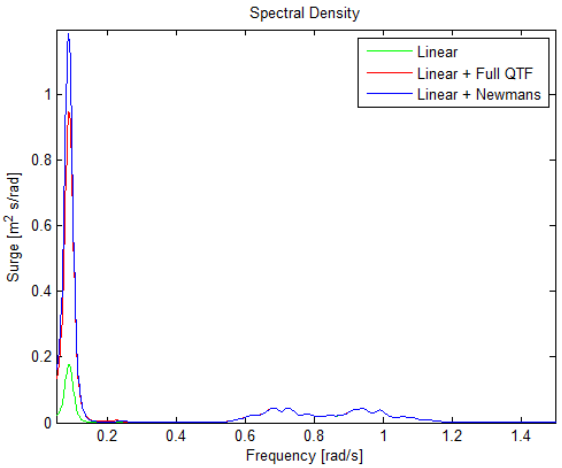

(a) O.1: Surge

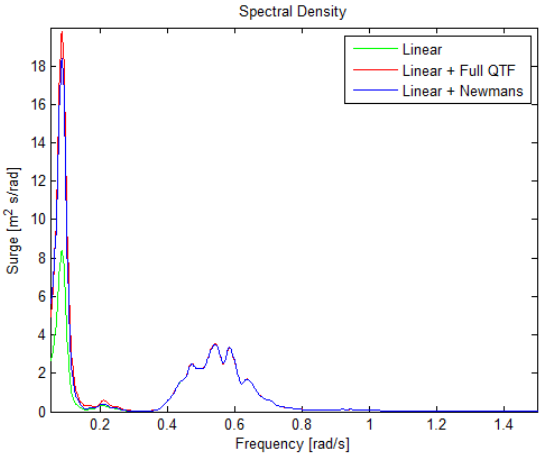

(b) C.2: Surge

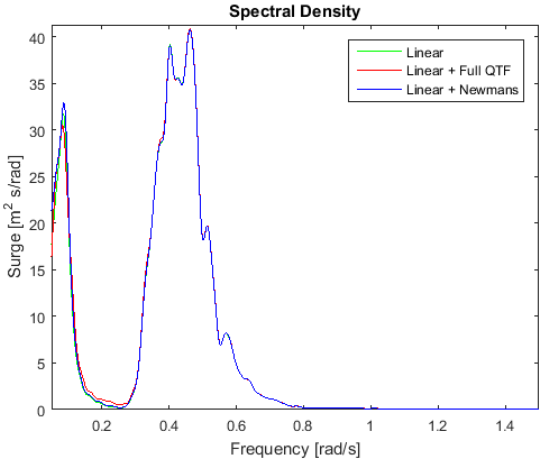

(c) X.1: Surge

Figure 8.1: Response PSD in surge

8.1.2 Heave and Pitch

The standard deviations of the heave motions are given in Table 8.3. The difference between applying a full QTF and Newman's approximation is more evident for this motion than surge. This was expected since the natural period in heave is smaller than in surge, and is, therefore, further away from the diagonal of difference-frequencies equal to zero. The difference is largest for load case O.1 and O.2. Figure 8.2 shows the

LC	Full QTF	Newman's app.	Difference
O.1 $[m]$	0.04	0.04	10.4 %
O.2 $[m]$	0.05	0.05	11.1 %
C.1 $[m]$	0.32	0.30	5.6%
C.2 $[m]$	0.32	0.31	4.7 %
X.1 $[m]$	1.52	1.48	1.3%
X.2 $[m]$	1.43	1.44	0.7 %

Table 8.3: Standard deviation of heave motion

response PSDs of heave motion. At wave frequencies, the graphs coincides and both the linear model and Newman's approximation estimate the response well. At low-frequencies, Newman's approximation underestimates the heave response significantly, as expected. A full QTF is therefore recommended to obtain the correct values of the heave response at low-frequencies. The natural period in pitch is also considered to be located far from the diagonal of zero-valued difference-frequencies. Thus, Newman's approximation is also expected to under estimate the responses at low-frequencies. This is not evident from the standard deviation of the pitch motion listed in Table 8.4. The largest difference is seen at load case O.1, but corresponds to 0.02 degrees which physically is extremely low. Figure 8.2 shows the PSD of the pitch response for three of the load cases. Load case O.1 shows the largest under prediction of the response at low-frequencies when Newman's approximation is applied. However, for load case C.2 and X.1, the agreement between the methods is good.

LC	Full QTF	Newman's app.	Difference
O.1 $[deg]$	0.12	0.14	12.9 %
O.2 $[deg]$	0.48	0.49	1.6 %
C.1 $[deg]$	0.44	0.46	3.7%
C.2 $[deg]$	0.79	0.8	1.25 %
X.1 $[deg]$	1.41	1.45	2.7%
X.2 $[deg]$	1.95	1.99	2.0%

Table 8.4: Standard deviation of pitch motion: Comparison of Newman's approximation and full QTF

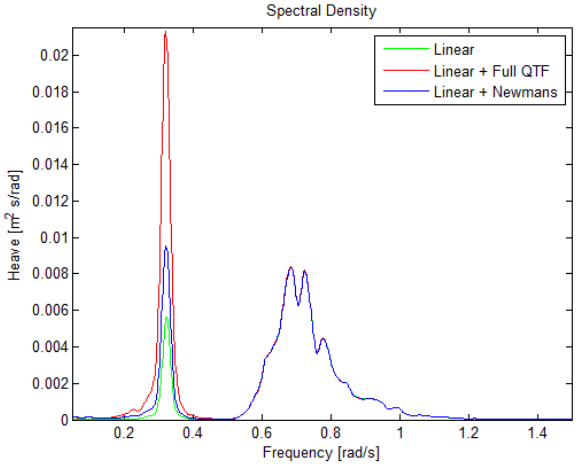

(a) O.1: Heave

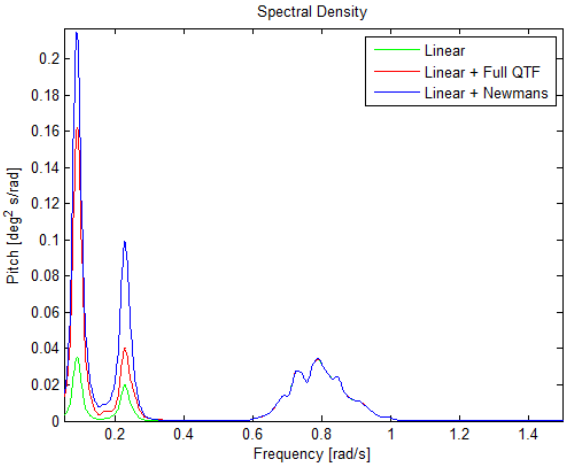

(b) O.1: Pitch

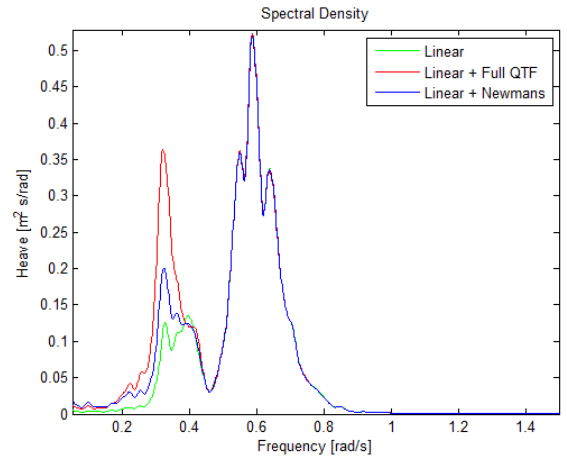

(c) C.2: Heave

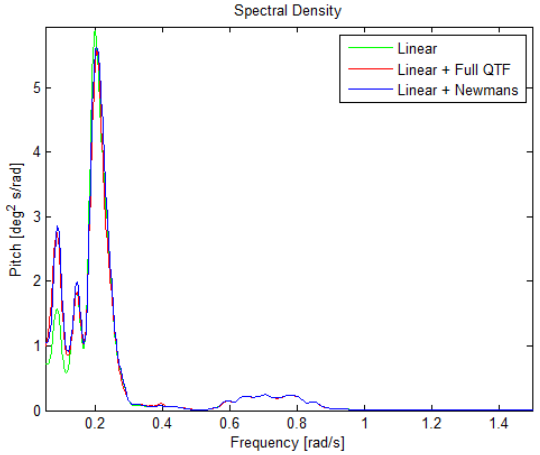

(d) C.2: Pitch

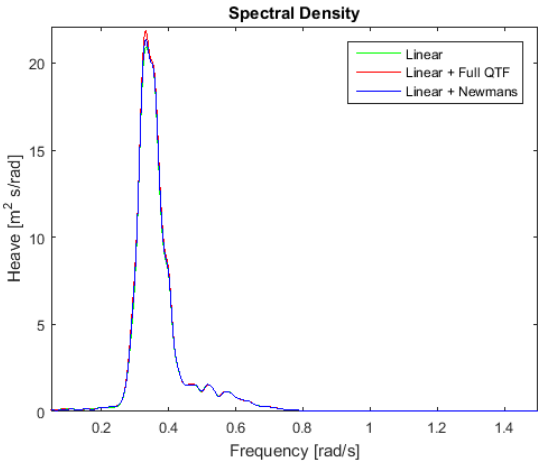

(e) X.1: Heave

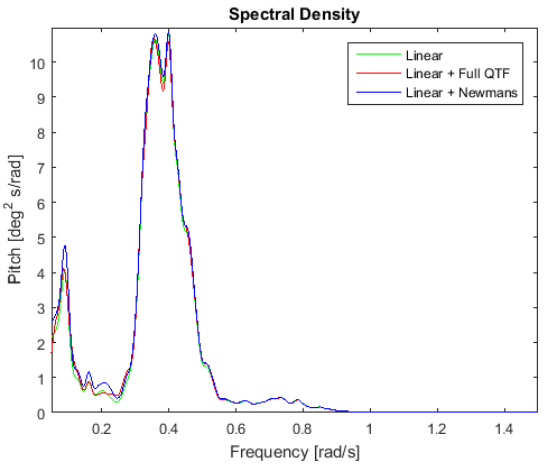

(f) X.1: Pitch

Figure 8.2: Response PSD in heave and pitch: Comparison of Newman's approximation and full QTF

8.1.3 Mooring Line Tension

The mooring line tension is essential to look at to find out if Newman's approximation is a suitable approximation method that can be used. It was observed that Newman's approximation gave some deviation of the maximum values of the surge motions compared to the model with the QTF, and the significance of these differences can be evaluated by investigating the mooring line tension. Only the mooring line tension in line 2 is considered since line 2, and 3 are the ones experiencing increased tension. Line 3 will experience the same as line 2. Load case O.1 and O.2 were not considered due to the low offset experienced under these conditions.

The standard deviations and the maximum values of the mooring line tension are seen in Table 8.5. For the maximum values, Newman's approximation overestimates the mooring line tensions. This is considered less critical than if the tension was underestimated. The differences are so small that the Newman's approximation can be suggested as a valid method to calculate second-order loads when considering the surge motion and the mooring line tension for the OO Star 10 MW Wind Floater at 50 m water depth.

LC		Full QTF	Newman's app.	Difference
C.1	Std. $[kN]$	173.27	172.32	0.5%
C.1	Max $[kN]$	3110.07	3224.78	3.6%
C.2	Std. $[kN]$	226.33	225.94	1.7%
C.2	Max $[kN]$	3419.10	3545.38	4.56%
X.1	Std. $[kN]$	1512.05	1569.00	3.6%
X.1	Max $[kN]$	11798.57	12544.00	5.9%
X.2	Std. $[kN]$	2541.85	2511.22	2.3%
X.2	Max $[kN]$	17712.87	18289.29	3.15 %

Table 8.5: Standard deviation and maximum value of mooring line tension in Line 2: Comparison of Newman's approximation and full QTF

8.2 Comparison Between Frequency Domain Analysis Model and Strip Theory Model

This section provides the comparison of response between the strip theory model and the model obtained from a linear frequency domain analysis(LFDA). Simulations with all load cases were carried out, but only load case C.1 and C.2 are presented in this section. This was decided because all load cases showed the same trends, and it was therefore considered unnecessary to comment on all cases. However, the response spectra for load case O.1, O.2, X.1, and X.2 are presented in the appendix. In the following section, the standard deviation of the response in surge, heave, and pitch are presented, as well as the PSDs. A comparison with the model including the full QTF, was also considered.

8.2.1 Load Cases: C.1 and C.2

Table 8.6 lists the standard deviations of surge, heave, and pitch for load case C.1 and C.2. The LFDA-model is compared with the model based on strip theory. Large differences are found for all motions in both cases. The lowest difference is of 15.5%, which is considered a significant difference. The response PSDs of the two load cases

C.1	LFDA	Strip Theory	Difference
Surge $[m]$	0.97	0.71	26.8 %
Heave $[m]$	0.29	0.24	17.2 %
Pitch $[deg]$	0.36	0.48	25.0 %
C.2	LFDA	Strip Theory	Difference
Surge $[m]$	1.03	0.87	15.5 %
Heave $[m]$	0.29	0.24	17.2 %
Pitch $[deg]$	0.75	1.14	34.2%

Table 8.6: Standard deviation of floater motions for load case C.1 and C.2

are presented in Figure 8.3. It can be seen that the model using strip theory, follows the same trends as the linear potential theory model. However, it overestimates the low-frequency motions and underestimates the wave-frequency motions. From the literature review conducted on Morison's equation on semi-submersibles from Section 2.3, it was expected that the model based on strip theory would over estimate the loads at low frequencies and under estimate the loads at high frequencies for heave and pitch. This trend can be seen in the current PSDs, but this is also found for the surge motion. The reason for the difference in the responses is the difference in added mass between the two models.

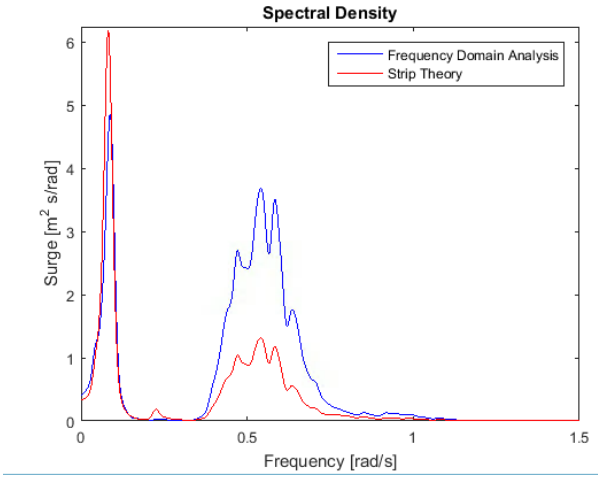

(a) Surge C.1

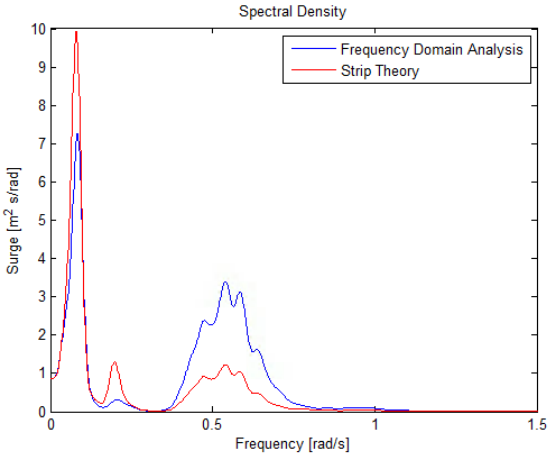

(b) Surge C.2

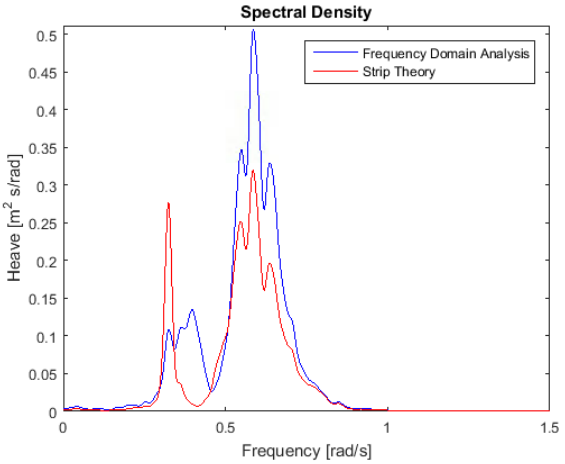

(c) Heave C.1

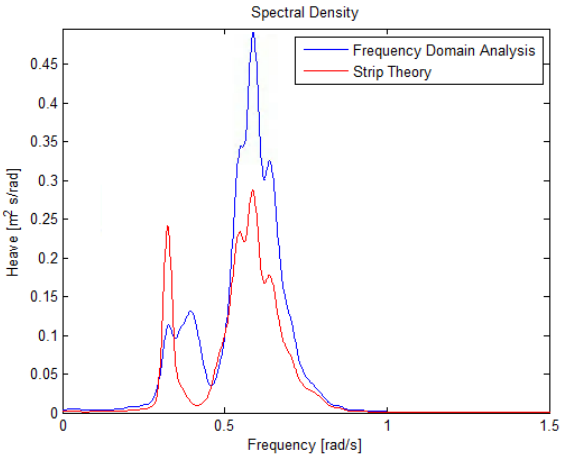

(d) Heave C.2

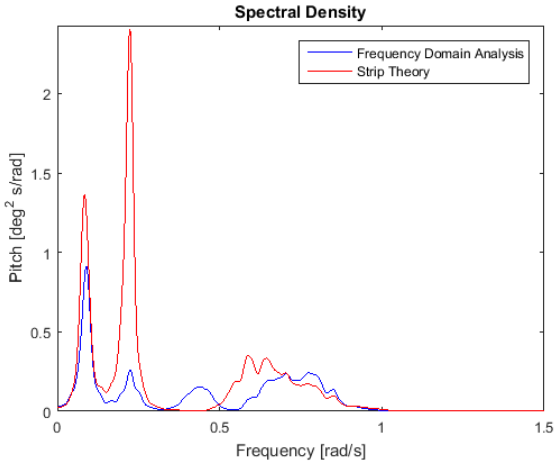

(e) Pitch C.1

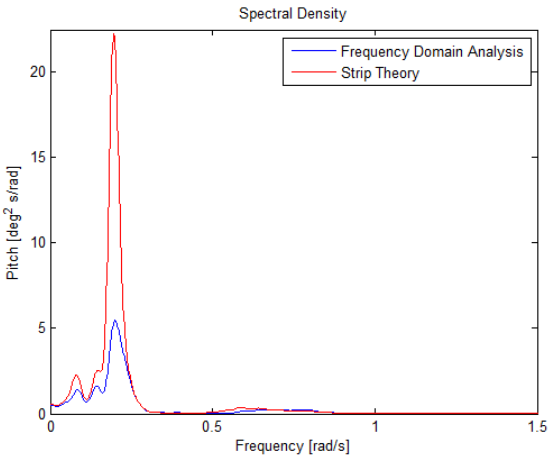

(f) Pitch C.2

Figure 8.3: Response spectra of load case C.1 and C.2 in surge, heave and pitch comparing strip theory model with LFDA-model

8.2.2 Comparison Between Strip Theory and Frequency Domain Analysis Model With Full QTF

The Strip theory model was also compared with the LFDA-model which includes the full QTF. For this comparison, only load case C.2 was considered. Figure 8.4 compares the response PSD in surge, heave, and pitch obtained by the strip theory model with the model using a full QTF. Even though the strip theory model over-estimated the low-frequency responses compared to the linear model, it does not coincide with the model using the full QTF. At wave frequencies, the linear and QTF-model show good agreement, while the strip theory model underestimates the responses. From Chapter 7, it was shown that the behavior of the floating wind turbine from low-frequency wave loads is crucial to capture to obtain the correct mooring line tension. It is therefore not recommended to apply strip theory according to the method described in this thesis when analyzing the behavior of a semi-submersible with the geometry of the OO Star Floater operating in 50 m water depth.

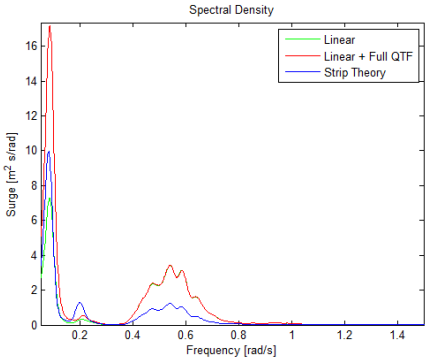

(a) Surge - C.2

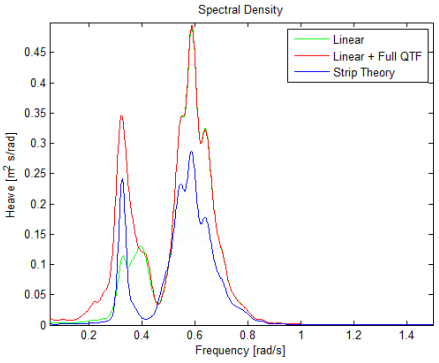

(b) Heave - C.2

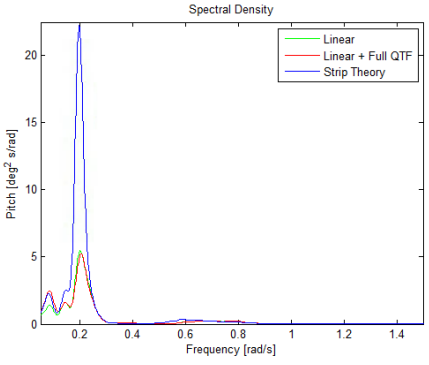

(c) Pitch - C.2

Figure 8.4: Response PSD for line tension for mooring line 1 and 2 for load case C.2, comparing strip theory model with LFDA-model including full QTF.

8.2.3 General Discussion of Results Obtain from Strip Theory Model

All load cases showed that the strip theory model, in general, underestimated the responses at low frequency and wave-frequency range compared to the model including a full QTF. There are several reasons why this happened. The difference in the added mass is possibly the main reason for this. The added mass coefficient was based on 2D-potential theory, and simplifications of the geometry were made. According to [2], this coefficient is both frequency-dependent and dependent on the KC-number.

For small waves, the wavelength-to-diameter ratio becomes small, and diffraction effects are important. These are not considered when applying strip theory since long-wave approximation is assumed.

The junctions between the columns and pontoons on the added mass were not taken into account.

Since the low-frequency motions are underestimated compared to results obtained with the model including the full QTF, the corresponding mooring line tensions will also be underestimated which is critical when looking at a mooring system in shallower water depths.

The applicability of strip theory is therefore not considered to be a valid method of calculating responses of the OO Star Wind Floater at 50 m water depth. However, the load model can be useful when looking at the main trends in the responses, if the fact that the responses are underestimated is considered.

Chapter 9

Conclusion and Recommendations for Further Work

9.1 Conclusion

A floating wind turbine operating at 50 m water depth has been studied. The OO Star 10 MW Wind Floater was considered and consists of a semi-submersible platform supporting the 10 MW DTU Reference Wind Turbine. A numerical model was developed by a panel method, and first and second-order frequency domain analyses were performed to obtain the hydrodynamic properties of the structure. These properties were imported into SIMA, where time-domain simulations were carried out. In addition, a model where added mass was calculated by strip theory was considered.

The main objective was to investigate the behavior of the floating wind turbine, as well as to evaluate the applicability of different hydrodynamic load models. This was done by comparing the results obtained from the four coupled models defined in Section 5.8.1. The following list presents the conclusions that were drawn based on the results.

- For the operational load cases, linear potential theory underestimated surge, heave, and pitch low-frequency motions compared to the model considering second-order effects. In these load cases, the largest offset in surge was found at low frequencies. The average maximum value in surge was 22% larger when including second-order effects. Therefore, second-order effects are important to take into account when considering a moored structure.
- For the extreme cases, linear potential theory did not underestimate the motions compared to the model including second-order effects. According to the literature review carried out on second-order effects, the effect of difference-frequencies

becomes small for extreme cases.

- The mooring line tension is directly related to the offset in surge. Since the maximum offset in surge was found at low frequencies, the maximum mooring line tension was also found in such movement. The difference in the maximum value of the mooring line tension between the linear model and the model accounting for second-order effects was 16.35% when looking at the operational cases. This implies that, to obtain the correct mooring line tension, it is important to include second-order effects in the calculations.
- Newman's approximation showed good agreement with the numerical model considering the full QTF in surge motion. Consequently, the large mooring line tension was also captured by Newman's approximation. It was therefore concluded that Newman's approximation can be applied when surge motion and mooring line tension are investigated. However, the motions in heave were underestimated at low frequencies, and a full QTF should be applied when studying this motion.
- The model based on strip theory overestimated the low-frequency motions and underestimated high-frequency motions compared to the LFDA-model. Compared to the model including the full QTF, strip theory underestimated all responses. However, PSDs showed that the strip theory model follows the same trend as the LFDA-model. Strip theory can therefore be applied to see the trends in the responses, but a frequency domain analysis is necessary to provide satisfactory results for the calculation of the responses.

9.2 Recommendations for Further Work

Topics that were not considered in this thesis but that should be looked into are listed below:

- According to the literature studies presented in Section 2.1, Wadam underestimates the difference-frequency loads compared to reality. A model test considering a floating wind turbine in shallow water depths should be carried out to see how much these loads are underestimated with Wadam.
- The mooring system design was not in focus during the work of the current project. The mooring system has a large effect on the responses of the turbine. Therefore, a mooring system which is more feasible at shallower water depths for the OO Star 10 MW Wind Floater should be developed.
- Continue the investigation of applying strip theory. A study on the effect of the KC-number on the added mass and drag coefficients should be carried out. The

counter interaction effect between the columns of the semi should also be looked into.

- The literature review reviled that the added mass of a heave plate is underpredicted by Wadam. This underprediction should be addressed and corrected for.
- In the strip theory model, the added mass of the heave plates was calculated by considering a general formula for the added mass of a disk. This is not accurate enough, and a CFD analysis of the heave plates should be conducted to get better predictions of the added mass and drag force of the heave plates.

Bibliography

[1] M. Haga, *Floating Wind Turbines in ShallowerDepth: Preliminary Studies*. NTNU, 2018.

[2] O. Faltinsen, *Sea Loads on Ships and Offshore Structures*. Cambridge University Press, 1990.

[3] D. Myrhaug, *Wave Statistics - Marine Dynamics Lecture Notes*. NTNU, 2004.

[4] M. O. Hansen, *Aerodynamics of wind turbines*. London: Earthscan c2008, 2nd ed. ed., 2008.

[5] M. Borg, M. Mirzaei, and H. Bredmose, *LIFES50+ D1.2: Wind turbine models for the design,*. DTU Wind Energy E-101, 2015.

[6] S. Ocean, *RIFLEX 4.12.2 User Guide*. 2018.

[7] W. Yu, K. Müller, and F. Lemmer, *LIFES50+ D4.2: Public Definition of the Two LIFES50+ 10MW Floater Concepts*. University of Stuttgart, 2018.

[8] T. Stenlund, *Mooring System Design for a Large Floating Wind Turbine in Shallow Water*. NTNU, 2018.

[9] A. Sayigh, *Comprehensive renewable energy*. Boston: Elevier, 2012.

[10] D. T. O. Olsen, "Lifes50+:prosjektbeskrivelse." `https://www.olavolsen.no/global/upload/4BPPQ/files/LIFES50%2B.pdf`, 2017. Accessed: 04-05-2019.

[11] A. Pegalajar-Jurado, F. Madsen, M. Borg, and H. Bredmose, "State-of-the-art models for the two lifes50+ 10mw floater concepts," tech. rep., 2018.

[12] M. Borg and M. Collu, "Offshore floating vertical axis wind turbines, dynamics modelling state of the art. part iii: Hydrodynamics and coupled modelling approaches," *Renewable and Sustainable Energy Reviews*, vol. 46, pp. 296 – 310, 2015.

[13] A. Pegalajar-Jurado, M. Madsen, F.J.and Borg, and H. Bredmose, "D4.4 – overview of the numerical models used in the consortium and their qualification," tech. rep., 2018.

[14] C. Lopez-Pavon, R. Watai, F. Ruggeri, A. Simos, and A. Souto-Iglesias, "Influence of wave induced second-order forces in semisubmersible fowt mooring design," *Journal of Offshore Mechanics and Arctic Engineering*, vol. 137, 01 2015.

[15] C. Lopez-Pavon and A. Souto-Iglesias, "Hydrodynamic coefficients and pressure loads on heave plates for semi-submersible floating offshore wind turbines: A comparative analysis using large scale models," *Renewable Energy*, vol. 81, pp. 864 – 881, 2015.

[16] T. Ishihara and S. Zhang, "Prediction of dynamic response of semi-submersible floating offshore wind turbine using augmented morison's equation with frequency dependent hydrodynamic coefficients," *Renewable Energy*, vol. 131, pp. 1186–1207, 2019.

[17] K. Xu, Z. Gao, and T. Moan, "Effect of hydrodynamic load modelling on the response of floating wind turbines and its mooring system in small water depths," *Journal of Physics: Conference Series*, vol. 1104, 2018.

[18] T. Duarte, A. Sarmento, and J. M. Jonkman, "Effects of second-order hydrodynamic forces on floating offshore wind turbines," 01 2014.

[19] G. de Hauteclocque, F. Rezende, O. Waals, and X. Chen, "Review of approximations to evaluate second-order low-frequency load," vol. 1, 07 2012.

[20] A. N. Simos, F. Ruggeri, R. Watai, A. Souto-Iglesias, and C. Lopez-Pavon, "Slow-drift of a floating wind turbine: An assessment of frequency-domain methods based on model tests," *Renewable Energy*, vol. 116, 09 2017.

[21] M. I. Kvittem, E. E. Bachynski, and T. Moan, "Effects of hydrodynamic modelling in fully coupled simulations of a semi-submersible wind turbine," *Energy Procedia*, vol. 24, no. C, pp. 351–362, 2012.

[22] K. Xu, Y. Shao, Z. Gao, and T. Moan, "A study on fully nonlinear wave load effects on floating wind turbine," *Journal of Fluids and Structures*, vol. 88, pp. 216 – 240, 2019.

[23] S. Ocean, *SIMO Theory Manual*. SINTEF Ocean.

[24] L. Li, Z. Gao, and T. Moan, "Joint distribution of environmental condition at five european offshore sites for design of combined wind and wave energy devices," vol. 137, no. 3, 2015.

[25] W. Inc, *WAMIT USER MANUAL Version 7*. WAMIT Inc., 2013.

[26] M. Greco, *Lecture notes, TMR 4215: Sea Loads*. NTNU, 2012.

[27] E. Bachynski, *Lecture notes - Basic aerodynamics for wind turbines*. NTNU, 2018.

[28] Equinor, "Hywind—the world's leading floating offshore wind solution." `https://www.equinor.com/en/what-we-do/hywind-where-the-wind-takes-us.html`, 2017. Accessed: 03-10-2018.

[29] Equinor, *Hywind Buchan Deep Metocean Design Basis*. Equinor, 2013.

[30] NREL, "Turbsim." https://nwtc.nrel.gov/TurbSim, 2017. Accessed: 10-05-2018.

[31] IEC, *NEK IEC 61400-1:2019 RLV*. NEK - Norsk elektronisk komite, 2019.

[32] D. GL, *Recommended Practice DNV-RP-C205, Environmental Conditions and Environmental Loads*. DNV GL, 2010.

[33] DNV GL, *GeniE V7.5-14 Documentation*. 2017.

[34] DNV GL, *HYDROD 4.10 SESAM USER MANUAL*. 2017.

[35] G. wind energy council, "Lifes50+." `https://lifes50plus.eu/`, 2017. Accessed: 10-9-2018.

[36] K. Xu, *Design and Analysis of Mooring System for Semi-submersible Floating Wind Turbines in Shallow Water*. NTNU, 2015.

[37] D. G. Software, *Sesam User Manual: Wadam*. DNV GL, 2015.

[38] D. GL, *DNV-RP-H103: Modeling and Analysis of Marine Operations*. DNV GL, 2011.

[39] L. Tao, B. Molin, Y.-M. Scolan, and K. Thiagarajan, "Spacing effects on hydrodynamics of heave plates on offshore structures," *Journal of Fluids and Structures*, vol. 23, no. 8, pp. 1119 – 1136, 2007.

[40] M. H. Hansen and L. C. Henriksen, *Basic DTU Wind Energy controller*. DTU Wind Enery Report E-0029, 2013.

[41] T. J. Larsen and T. D. Hanson, "A method to avoid negative damped low frequent tower vibrations for a floating, pitch controlled wind turbine," *Journal of Physics: Conference Series*, vol. 75, p. 012073, jul 2007.

[42] J. JM, S. Butterfield, W. Musial, and G. Scott, "Definition of a 5mw reference wind turbine for offshore system development," *National Renewable Energy Laboratory (NREL)*, 01 2009.

[43] E. Bachynski, *Project Description - Integrated Dynamic Analysis of Wind Turbines TMR4505*. NTNU, 2018.

Appendix A

PSDs of Frequency Domain Analysis Model Compared With Strip Theory Model

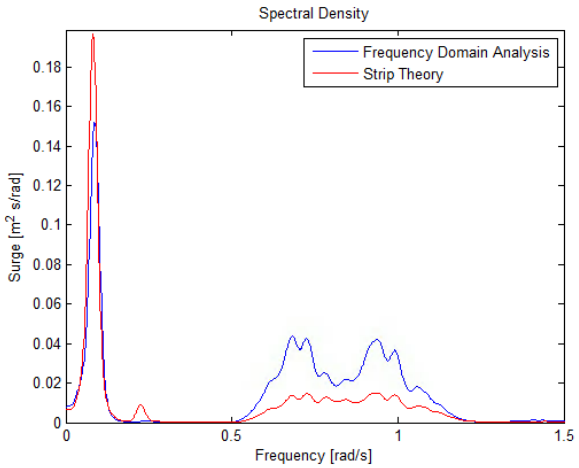

(a) Surge O.1

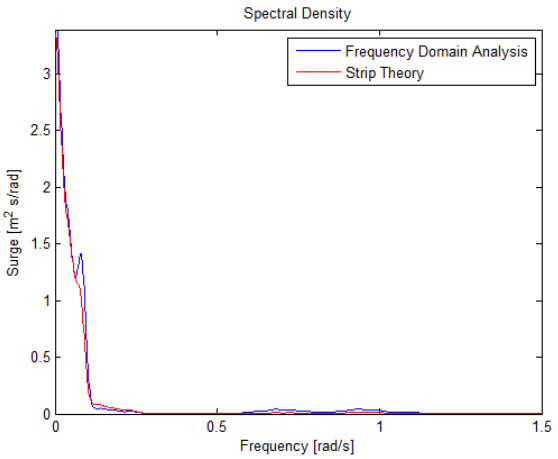

(b) Surge O.2

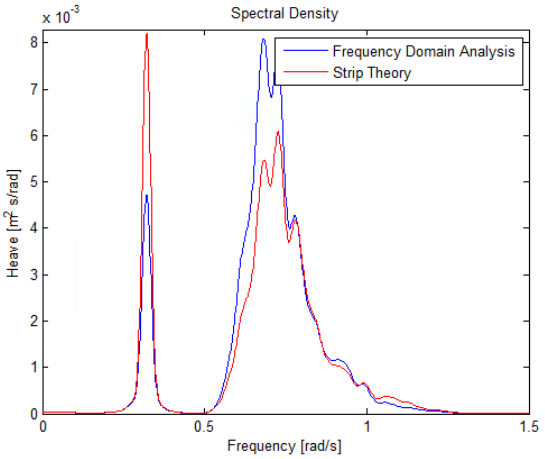

(c) Heave O.1

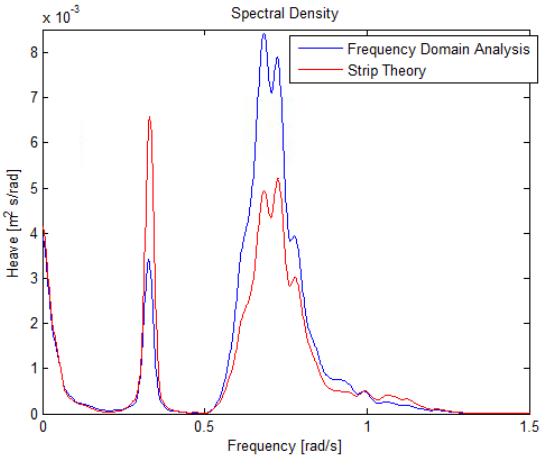

(d) Heave O.2

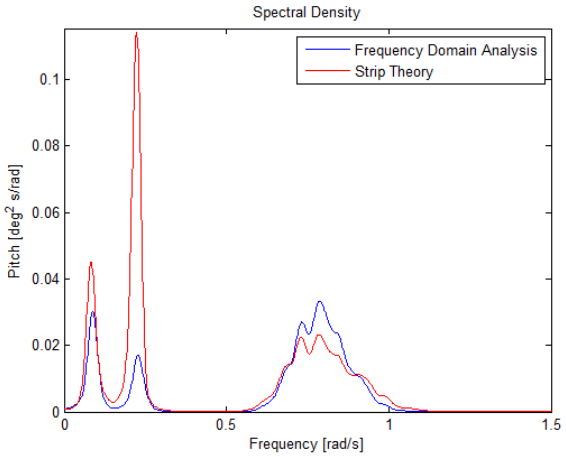

(e) Pitch O.1

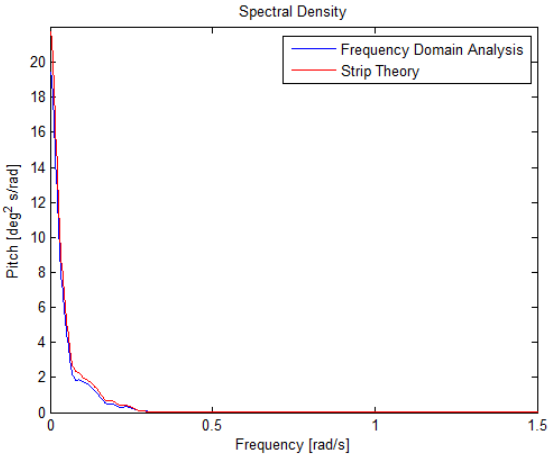

(f) Pitch O.2

Figure A.1: Response spectra of load case O.1 and O.2 in surge, heave and pitch.

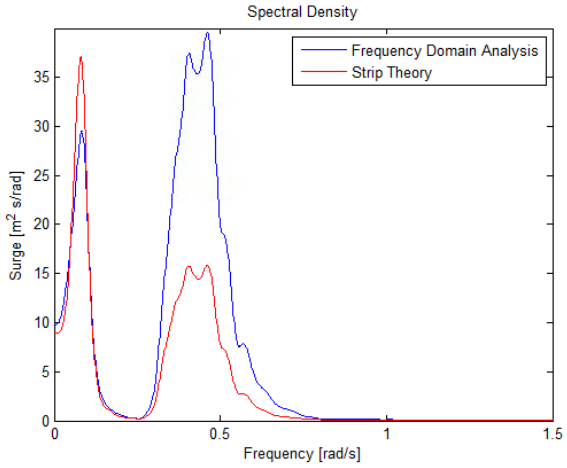

(a) Surge X.1

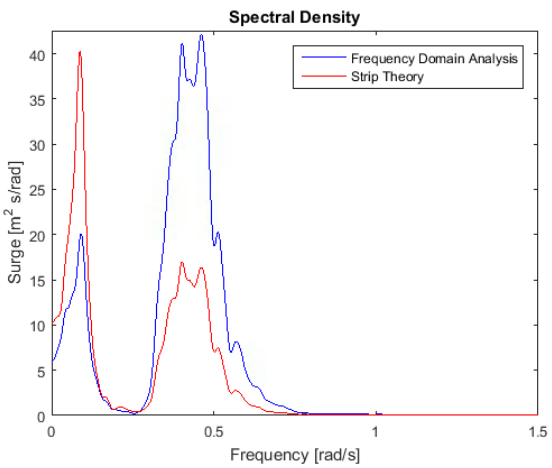

(b) Surge X.2

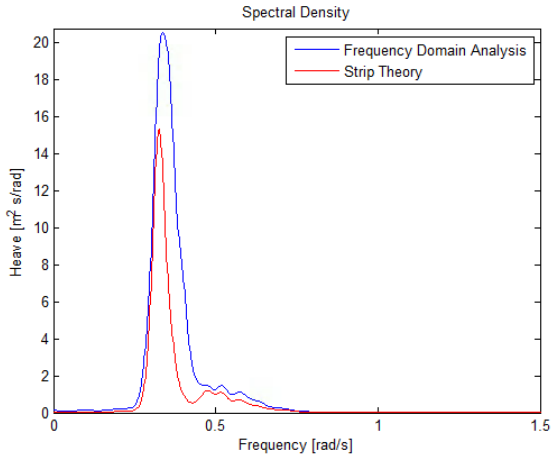

(c) Heave X.1

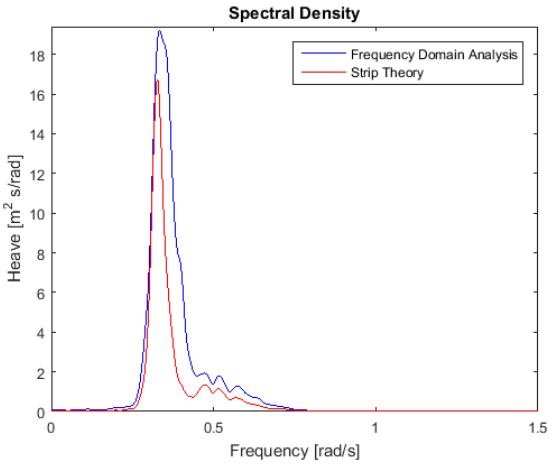

(d) Heave X.2

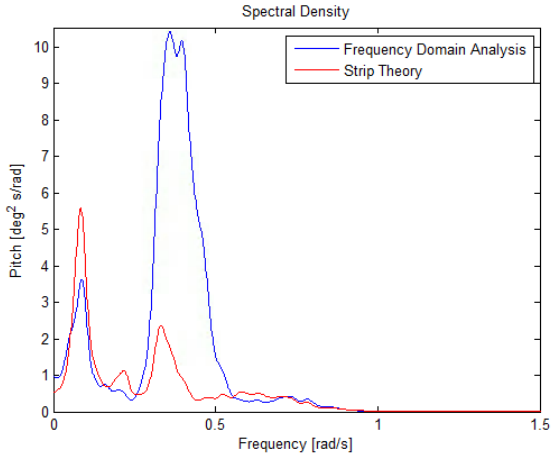

(e) Pitch X.1

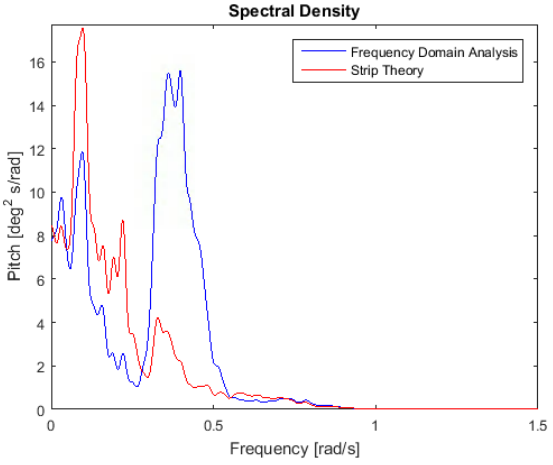

(f) Pitch X.2

Figure A.2: Response spectra of load case X.1 and X.2 in surge, heave and pitch.

Mildrid Sofie Breivik Haga

Hydrodynamic Challenges of Floating Wind Turbines in Shallower Water Depth

NTNU
Norwegian University of
Science and Technology